A TUNEABLE ELECTROMAGNETIC BAND-GAP MICROSTRIP FILTER

A Thesis

presented to

the Electrical Engineering Department Faculty of

California Polytechnic State University, San Luis Obispo

In Partial Fulfillment

of the Requirements for the Degree

Master of Science in Electrical Engineering

by

Greg Lancaster

January 2013

Committee

TITLE:	A Tuneable Electromagnetic Band-gap Microstrip Filter
AUTHOR:	Greg Lancaster
DATE SUBMITTED:	January 2013
COMMITTEE CHAIR:	Dr. Vladimir Prodanov, Assistant Professor of Electrical Engineering
COMMITTEE MEMBER:	Dr. Dennis Derickson, Department Chair of Electrical Engineering
COMMITTEE MEMBER:	Dr. Tina Smilkstein, Assistant Professor of Electrical Engineering

Abstract

A Tuneable Electromagnetic Band-gap Microstrip Filter

Greg Lancaster

In high frequency design, harmonic suppression is a persistent struggle. Non-linear devices such as switches and amplifiers produce unwanted harmonics which may interfere with other frequency bands. Filtering is a widely accepted solution, however there are various shortcomings involved. Suppressing multiple harmonics, if desired, with traditional lumped element and distributed component band-stop filters requires using multiple filters. These topologies are not easily made tunable either. A new filter topology is investigated called Electromagnetic Band-Gap (EBG) structures.

EBG structures have recently gained the interest of microwave designers due to their periodic nature which prohibits the propagation of certain frequency bands. EBG structures exhibit characteristics similar to that of a band-stop filter, but in periodically repeating intervals making it ideal for harmonic suppression. The band-gap frequency of an EBG structure may be varied by altering the periodicity of the structure. However, EBG materials are generally static in structure making tuning a challenge.

In this thesis, a novel solution for tuning the band-gap properties of an EBG structure is investigated. Designs aimed to improve upon existing solutions are reached. These designs involve acoustic and mechanical tuning methods. Performance is simulated using Agilent's Advanced Design System (ADS) and a device is constructed and evaluated. Comparing all measured test cases to simulation, band-gap center frequency error is on average 4.44% and absolute band-gap rejection error is 1.358 dB.

Acknowledgements

I would like to thank Dr. Vladimir Prodanov, my advisor, for devising the initial concept and being a source of guidance and support throughout the project's development. This thesis couldn't have been completed without his insight and help in overcoming challenges encountered along the way.

I would like to thank my family, Clint, Diane, and Scott for their continual support of my educational decisions. Your encouragement has helped me throughout my entire college career and for that I am very thankful.

Lastly, I would like to thank the entire Cal Poly electrical engineering faculty and staff for helping develop my education; an invaluable asset in which this thesis would not have been possible without.

Table of Contents

List of Tables

List of Figures

Chapter 1
INTRODUCTION

1.1 Electromagnetic Band-Gap Structures

Electromagnetic band-gap (EBG), also known as photonic band-gap (PBG), structures are useful in microwave applications because of their periodic nature which prohibits the propagation of certain electromagnetic wavelengths. An EBG material is essentially composed of periodically repeating high and low dielectric regions which, based on the periodicity of the structure, creates frequency band-gaps. EM waves at the band-gap frequency or integer multiples of the band-gap frequency cannot propagate through the material.

EBG materials exist in one, two, and three dimensional forms. A one-dimensional EBG structure exists when the dielectric constant repeats periodically in only a single direction, creating a band-gap in the direction of the periodicity. An example of a 1-D EBG is a dielectric mirror which incorporates a stack of periodically repeating high and low refractive index layers to reflect certain wavelengths of light based on the periodicity of the layers [1]. A 2-D EBG structure is periodic in two directions. 2-D EBG structures are used in microstrip patch antennas to suppress harmonic surface waves in the substrate of the antenna. 3-D EBG structures exist in nature and are referred to as photonic band-gap materials. The gemstone opal is an example of a PBG structure. Opal's internal structure is composed of small spheres of silica stacked on top of each other, forming a lattice of silica [2]. The interaction between EM waves and the silica lattice causes certain wavelengths of light to be diffracted. The wavelength of the diffracted light is

based on the size and spacing of the silica spheres. Figure 1.1 illustrates the three types of EBG structures.

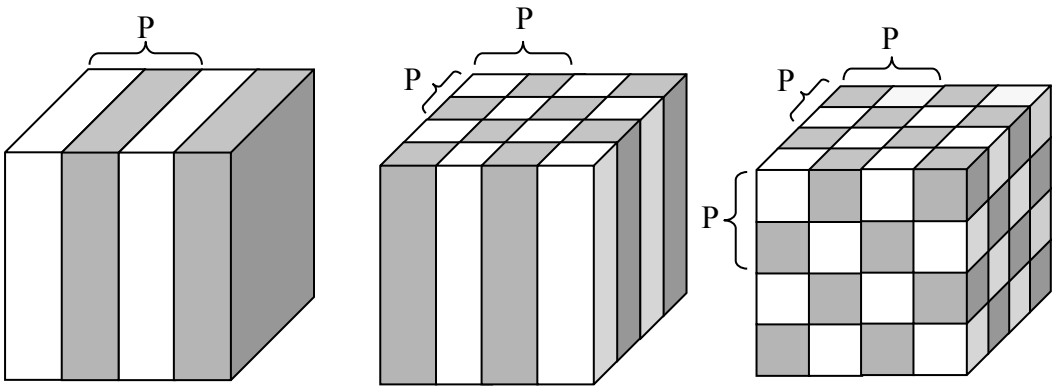

Figure 1.1: (a) 1-D EBG structure (b) 2-D EBG structure (c) 3-D EBG structure. Grey and white signify high and low dielectric regions and P signifies the length of one period.

1.2 Applications and Uses

EBG structures are desirable for harmonic filtering applications because of their repeating band-gap properties. Harmonics arise from non-linear devices and are a common problem in high frequency design. Harmonic content is unwanted because it may interfere with other frequency bands being used, effectively reducing their sensitivity. Filtering is the best solution to reduce harmonic levels, but traditional lumped element and distributed element filters only filter a single frequency band. Filtering multiple frequency bands requires implementing multiple filters. EBG structures filter not only the fundamental band-gap frequency, but also integer multiples of the fundamental frequency. This eliminates the need of multiple filters.

An example of an applied EBG filter is a microstrip with a 2-D pattern of etched circles in the ground plane. The spacing between etched circles determines the band-gap frequency and the circle radius determines the gap width. The filter is constructed by etching circles into the bottom (ground) plane of a double-sided copper clad substrate

supporting a 50Ω microstrip line. Figure 1.2 illustrates a filter with etched circles of radius ‘r’ and spacing ‘a’.

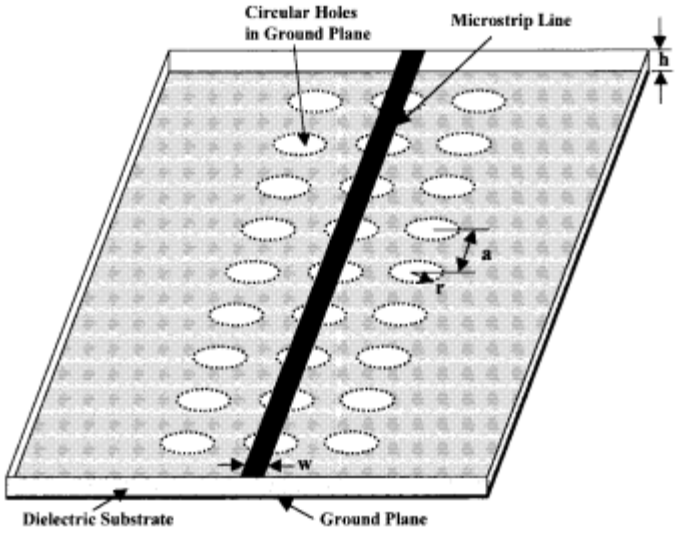

Figure 1.2: A 2-D EBG microstrip filter with a ground plane etched pattern [3].

1.3 Problem and Proposed Solution

For design robustness in a filter it may be desirable to have tuning options. Key parameters which define a band-gap filter’s response include its band-gap frequency (center frequency), rejection, and band-gap width (bandwidth). These are the parameters which should be able to be tuned in a tunable EBG structure. Lumped element filters may be tuned by varying capacitor and inductor component values. Distributed element filters may be tuned by varying stub and transmission line lengths. EBG structures prove to be much more difficult in varying their properties. To tune the band-gap frequency of an EBG filter, its periodicity must be changed. This requires physically altering the structure. Some solutions already exist but each has its faults.

1.4 Existing Solutions

Recent research has provided a few solutions for tunable EBG structures. However, existing solutions lack robustness in tunable frequency range and resolution. A wide tunable frequency range allows the band-gap frequency of the filter to be adjusted over a wide frequency range. This may increase filter usefulness and open it to more applications. A fine adjustable resolution allows a desired band-gap frequency to be realized with greater precision.

1.4.1 Dynamic Tuning of Grounded Patch Microstrip EBG

One solution [4] involves periodically shifting the ground plane in a dual layer substrate of a microstrip line to achieve an EBG structure. The structure, shown in Figure 1.3, is composed of a single microstrip line supported by a dual layer substrate with a ground plane underneath. The substrate has a thick bottom layer made of high dielectric alumina and a thin top layer made of low dielectric polyimide. The thickness ratio of alumina to polyimide is 25:2. There are 24 metal patches sandwiched between the two dielectric layers spaced evenly along the microstrip line. When a patch is short circuited, through a ground via, the alumina layer becomes isolated from the microstrip. Isolating the alumina layer decreases the effective dielectric constant subjected to microstrip at the location of the patch. Grounding patches in periodic patterns produces a periodically repeating high and low dielectric constant on the microstrip, which forms an EBG structure.

This method achieves tunability by controlling the length of the dielectric period. The minimum period length is reached when every patch is grounded. For this scenario, the period length equals the width of the patch plus the width of the gap between patches.

Other repeating period combinations which produce different band-gap frequencies include 10, 1100, 111000, 11110000 etc… (1 = grounded patch and 0 = floating patch).

This solution lacks resolution in frequency tunability. With only 24 patches, a limited number of band-gap frequencies can be realized. Adjusting band-gap frequency in discrete increments is not ideal for tunable filter applications. In Figure 1.4 the band-gaps of a few periodic combinations are compared.

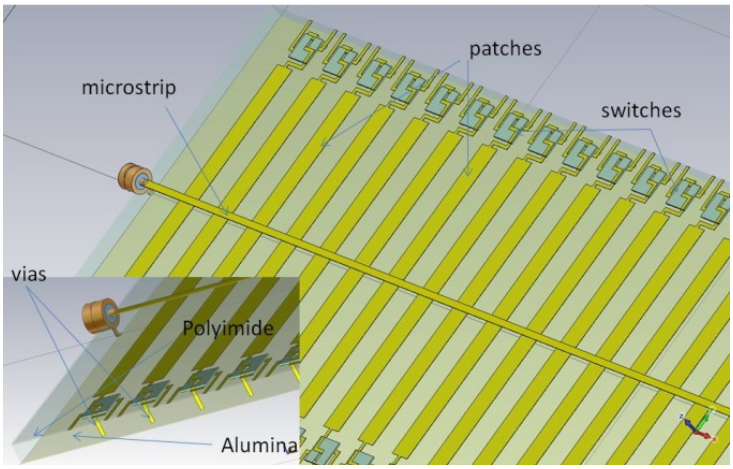

Figure 1.3: Model of the grounded patch microstrip EBG structure [4].

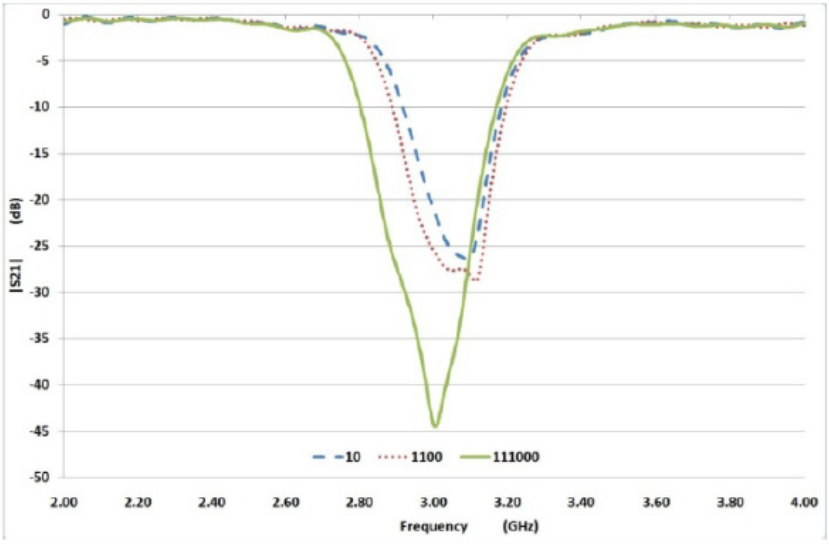

Figure 1.4: S21 responses for "10", "1100", and "111000" periodic patterns [4].

1.4.2 Tunable acoustic gratings in solid-core photonic bandgap fiber

Another solution [5], published in 2007, presents a technique for tuning a photonic crystal fiber (PCF) using an acoustic stimulus. A PCF is an optical fiber, which is periodic in one or two directions. Any light that propagates through the PCF is subject to PBG behavior due to the periodic microstructure of the fiber. A common periodic formation involves the solid-core fiber surrounded by hollow air-filled holes in two dimensions. This periodic formation is similar to that of the 2D pattern of ground plane etched circles. A more specific type of PCF is a photonic band-gap fiber (PBGF). A PBGF is realized by filling the air holes of a PCF with a material with a refractive index greater than that of the light-carrying core. Unlike a PCF, a PBGF relies on Bragg reflection as the method of wave-guidance instead of total internal reflection. In total internal reflection, the refractive index of the light-carrying core is higher than that of its cladding. However, in a PBGF, the light propagates in a low dielectric (or refractive index) medium through Bragg reflections off of the periodically repeating high and low dielectric cladding. Figure 1.5 illustrates cross-sections of various PCFs. Table 1.1 defines key distinctions between PCFs and PBGFs.

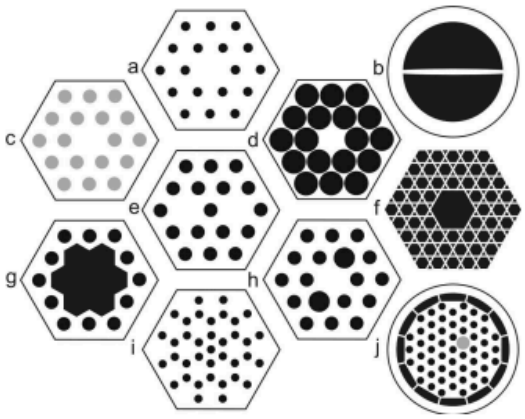

Figure 1.5: Cross-sections of various PCF configurations. White regions represent the fiber, and black regions represent hollow space [6].

Table 1.1: Core, cladding, and waveguiding principles for various PCFs [7].

	Cross section and waveguiding principle
Hole-assisted fiber (HAF)	Air hole; High-refractive-index core — Core: high-refractive-index glass; Clad: hole-added glass; Waveguiding principle: total reflection
Photonic crystal fiber (PCF)	Air hole; Silica glass core — Core: silica glass; Clad: glass with holes added; Waveguiding principle: total reflection
Photonic band-gap fiber (PBGF)	Air hole; Hollow core — Core: hollow; Clad: hole-added glass; Waveguiding principle: Bragg reflection
Existing optical fiber (SMF)	High-refractive-index core — Core: high-refractive-index glass; Clad: glass; Waveguiding principle: total reflection

This study aimed to achieve tunable gratings through acousto-optic interaction of the fiber core. The air holes of a PCF are filled with a high dielectric fluid and the fiber is stimulated by a piezoelectric acoustic transducer. An acoustic dampener is placed along the fiber at a chosen distance from the transducer to terminate the acoustic wave. An acoustic wave traverses the fiber slightly bending the fiber up and down, forming periodic perturbations in the fluid filled holes. The periodicity of the perturbations is controlled by the frequency of the acoustic wave. The fiber was stimulated with acoustic frequencies ranging from 1.4MHz to 2MHz (ultra sonic) to yield band-gap wavelengths

from 840nm to 880nm. The system achieves a >10dB notch over the tunable range. Six transmission spectrums are illustrated in Figure 1.6 (a) for various acoustic frequencies. Also shown (Figure 1.6 b) is the linear relationship between applied acoustic frequency and the resulting band-gap center frequency.

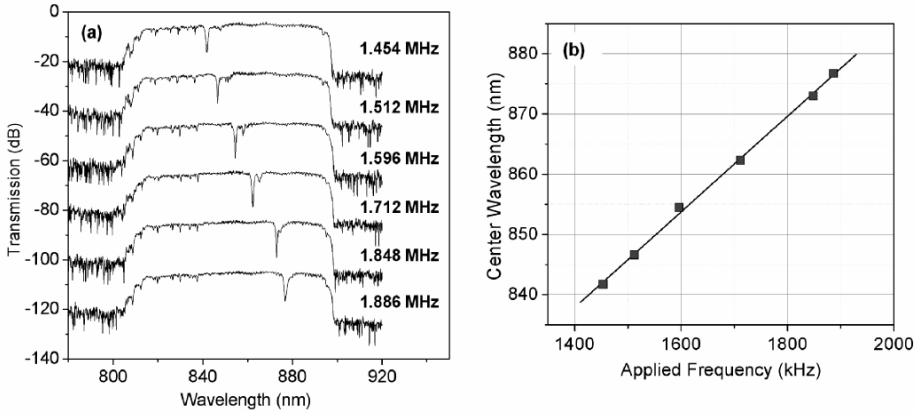

Figure 1.6: (a) Spectral results for six acoustic frequencies. (b) Band-gap center frequency vs. applied acoustic frequency [5].

Although fine tuning resolution is possible unlike in the grounded patch microstrip, the tunable range is very limited. In optical filtering applications wide tunable range may not be desired. A wider tunable range is more beneficial for applications in the microwave frequency range. A new EBG tuning method must be developed.

1.5 Project Goal, Specifications, and Considerations

This thesis aims to put forth and evaluate a novel solution for a tunable EBG filter. The filter shall be based on a 1-D EBG structure. Tuning mechanisms of varying complexity are to be developed to aid with tuning the EBG structure. The project scope includes designing, simulating, constructing, and testing the proposed tunable EBG filter solutions.

1.5.1 Specifications

To improve upon previous solutions, a wide tunable range and fine tunable precision must both be accommodated. A wide tunable frequency range of 1 – 6 GHz is chosen. This range covers many wireless communications frequency bands and their resulting harmonics. A 5GHz tunable range is much larger than the previously investigated solutions. Unlike the grounded patch microstrip, a non-discrete tuning mechanism must be implemented to achieve fine tunable precision. Passband ripple should be minimized while stopband rejections should be maximized. To provide adequate attenuation, band-gap rejection should be >10dB. Passband ripple should be <1dB so passband frequencies are not inadvertently attenuated.

1.5.2 System Interface

A microstrip topology is chosen as the medium to support the EGB for its simplicity in design, simulation, and fabrication. Also for the sake of simplicity a one-dimension EBG structure design is chosen. The filter should use standard RF connectors such as SMA connectors for ease of testing and must have 50Ω input impedance. There must be a guide to describe how much the filter must be tuned to achieve a desired band-gap frequency; for instance the band-gap center frequency vs. applied acoustic frequency graph in Figure 1.6 (b).

1.5.3 Consideration and Challenges

Simulation: A simulation tool must be used to aid in the design and simulation of the filter. Agilent's Advanced Design System (ADS) offers many potentially useful microstrip simulation features such as multilayer substrates models, a line width and impedance calculator program (LinCalc), and optimization tools.

Fabrication: Dielectric substrates must be selected to support the microstrip and a milling machine will be used to fabricate the designed microstrip layout. This shall be accommodated by a milling machine located on campus at Cal Poly University, San Luis Obispo.

Testing: To test the performance of the filter a high frequency network analyzer must be used. A method for extracting data from the network analyzer for analysis must also be available.

Challenges: The major challenge lies in contriving a method to physically alter the periodicity of the EBG structure. The tuning mechanisms must be robust enough to support wide and precise frequency tuning, adding to the difficulty of the project.

Chapter 2
BACKGROUND ON FILTERS AND EBG STRUCTURES

2.1 Passive Filter Response Types

Passive filters, opposed to active filters, do not require the use of an external power supply or active devices. There are four basic types of passive filters. They are characterized by their frequency response:

Low-pass filter: attenuates high frequency signals and is characterized by its cutoff frequency, the frequency at which insertion loss drops 3dB below pass band gain level.

High-pass filter: attenuates low frequency signals and is characterized by its cutoff frequency, the frequency at which insertion loss drops 3dB below pass band gain level.

Band-pass filter: passes signals of the frequency between its two cutoff frequencies. They are characterized by their bandwidth, the frequency difference between the upper and lower 3dB cutoff points.

Band-stop filter: attenuates signals of the frequency between its two cutoff frequencies. They are characterized by their bandwidth, the frequency difference between the upper and lower 3dB cutoff points.

Other parameters which define band-stop filter performance are ripple and rejection. Ripple is the amount of magnitude variation in the pass-band. Rejection is the attenuation of the stop-band with respect to the pass-band. For all intents and purposes

EBG filters act like band-stop filters, but with periodically repeating band-stop segments. A typical band-stop frequency response is shown in Figure 2.1 with labeled parameters.

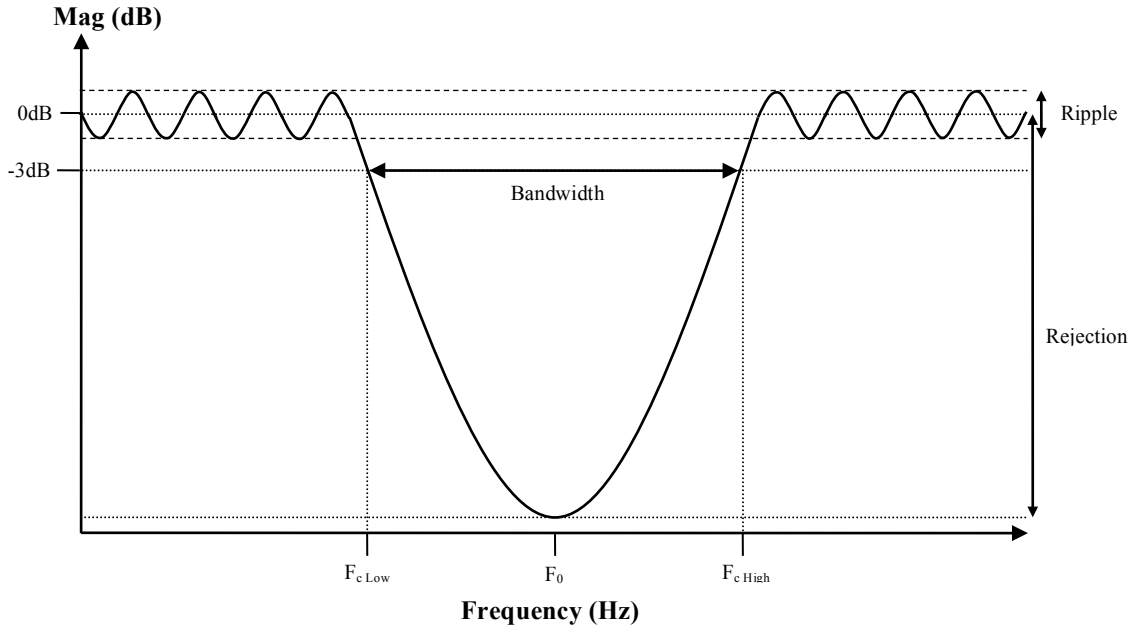

Figure 2.1: Typical band-stop filter frequency response (S_{21}).

2.2 Passive Filter Topologies

Two topologies are commonly used to realize a passive filter. The following is a description of these two topologies:

2.2.1 Lumped Element Filters

Lumped element filters use passive circuit elements such as capacitors and inductors. Capacitors impede low frequency signals, and pass high frequency signals. While inductors impede high frequency signals and pass low frequency signals. A band-stop filter may be realized by using shunt or series connected parallel and series resonant pairs of capacitors and inductors. The resonant frequency of each pair is the frequency at which the impedance is purely real (resistive). A series resonant pair (Figure 2.2 (a)) will act as a short circuit at the resonant frequency. A parallel resonant pair (Figure 2.2 (b))

will act as an open circuit at the resonant frequency. By using series connected parallel resonant pairs and shunt connected series resonant pairs, a band-stop filter can be achieved.

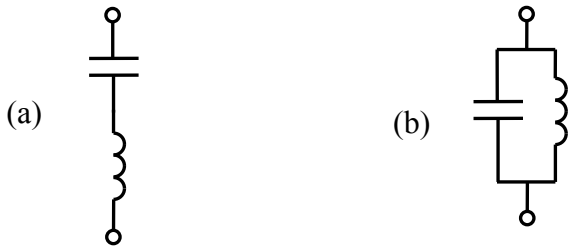

Figure 2.2: (a) Series connected resonant pair. (b) Parallel connected resonant pair.

Advantages: Lumped element filters may be tuned by varying capacitor and inductor component values. Variable capacitors are commonly used in tunable LC circuits and variable inductors, while not as common as variable capacitors, are also available.

Another lumped element advantage is their compactness. The smallest package size available for capacitors and inductors is 0.01" x 0.005" (01005). Small size is desired in high frequency design in order to reduce the electrical length of circuits and potential for unwanted coupling of neighboring circuits; as well as minimizing overall circuit board space usage.

Disadvantages: Capacitor and inductors become less ideal as frequency increases due to inherent parasitics. An actual capacitor may be modeled by an ideal capacitor, resistor, and inductor connected in series. The resistor introduces loss to the capacitor and the inductor causes series resonance at a certain frequency. An actual inductor may be

modeld by an ideal inductor in series with a resistor, all in parallel with a capacitor. The resistor adds loss while the capacitor causes parallel resonance.

Another disadvantage is the limited selection of capacitor and iniductor values. When a lumped element design is reached, it must be implemented with available capacitor and inductor values. Using capacitor or inductor values different from the design will alter the filter's response.

2.2.2 Distributed Component Filters

Distributed components, such as open or short-circuited transmission line stubs can be used to replicate reactive elements such as capacitors and inductors. This introduces another filter topology: distributed component filters. Distributed component filters are most commonly implemented in a microstrip structure. Richard's transformation may be used to convert a lumped-element into a distributed component transmission line stubs. This allows a lumped element design to be converted directly to a distributed component design. The input impedance of a short circuit stub can be found as

$$Z_{in} = jZ_0 tan\beta\ell,$$

and for a open circuit stub as

$$Z_{in} = -jZ_0 cot\beta\ell.$$

where:

Z_{in} = input impedance of stub;

Z_0 = characteristic impedance of stub;

$\beta = \frac{2\pi}{\lambda}$ = wavenumber;

ℓ = stub electrical length.

Therefore, for a stub of length $\ell = \lambda/8$,

$$Z_{in} = jZ_0 \tan\left(\pi/4\right) = jZ_0,$$

for a short circuit stub, and

$$Z_{in} = -jZ_0 \cot\left(\pi/4\right) = -jZ_0,$$

for an open circuit stub.

At frequency ω_c, a short circuit stub of $\ell = \lambda/8$ can be used to replicate the impedance of an inductor if the characteristic impedance is equal to the reactance of the inductor: $Z_0 = \omega_c L$. Likewise, an open circuit stub of $\ell = \lambda/8$ can be used to replicate the impedance of a capacitor if the characteristic impedance is equal to the reactance of the capacitor: $Z_0 = 1/\omega_c C$. This is the basis of Richard's transformation and is shown in Figure 2.3.

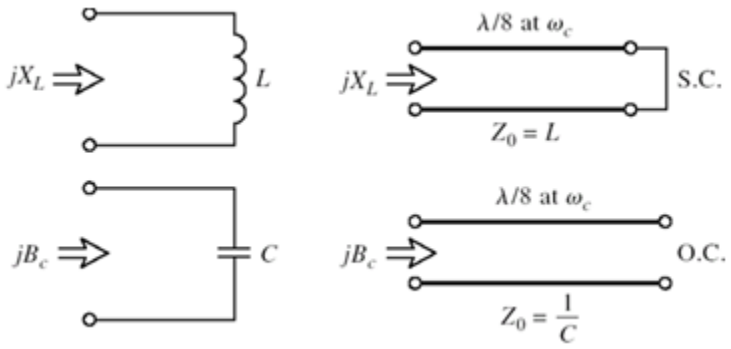

Figure 2.3: Richard's transformation for an inductor replicated by a short circuit stub, and a capacitor replicated by an open circuit stub [8].

Advantages: Unlike lumped element design, any capacitor or inductor value can be realized by setting the appropriate stub length and characteristic impedance. This makes distributed component filter more ideal for applications where precision is critical.

Disadvantages: Since the electrical length of a stub is frequency dependent, the input impedance a stub varies with frequency. The input impedance of a stub matches

that of the capacitor/inductor which it is designed to replicate at only one exact frequency.

Since a microstrip filter is made of copper lines etched on a substrate, it may not be tuned easily. Adjusting the width (characteristic impedance) or length of a microstrip stub or transmission line requires cutting or adding copper. This process takes a lot of time and is difficult to produce desired tuning results.

2.3 Band-gap Effect

The band-gap effect, which is the formation of a frequency band-gap due to periodically repeating dielectric, is most easily explained in a one dimensional EBG structure. A one dimensional EBG structure consists of two dielectrics of different permittivity (dielectric constant) repeating with a constant periodicity in one direction [9]. In Figure 2.3 an incident wave W_i enters a one dimensional EBG material made of dielectrics ε_1 and ε_1 with lengths ℓ_1 and ℓ_2 respectively. The period length $\ell_P = \ell_1 + \ell_2$. A material's dielectric constant affects its electrical length as perceived by an EM wave propagating through it. The incident wave is reflected at the interface of two periodic cells. This reflected wave W_r interferes with the incident waves creating a standing wave, effectively forbidding linear propagation of this wavelength through the EBG structure. This occurs at each periodic cell interface throughout the length of the one-dimensional EBG structure. The path difference d between incident and reflected waves in a one-dimensional EBG is,

$$d = 2(\sqrt{\varepsilon_1}\times\ell_1 + \sqrt{\varepsilon_2}\times\ell_2).$$

The frequency whose wavelength λ is equal to this distance, is the center of the band-gap frequency λ_c. This also applies to all integer multiples of this frequency.

The band-gap condition in equation form is as follows,

$$d = 2(\sqrt{\varepsilon_1}\times\ell_1 + \sqrt{\varepsilon_2}\times\ell_2) = m\lambda.$$

where:

m = 1,2,3…

Therefore the center band-gap frequency may be stated as,

$$\lambda_c = \frac{2(\sqrt{\varepsilon_1}\times\ell_1+\sqrt{\varepsilon_2}\times\ell_2)}{m}.$$

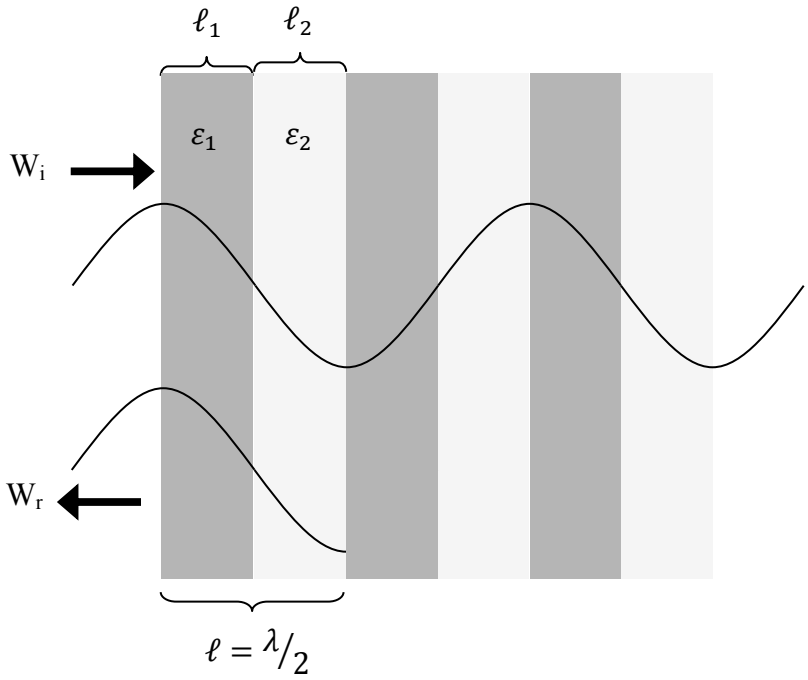

Figure 2.4: Incident (Wi) and reflected (Wr) waves in a one dimensional EBG structure. The interfering waves form a standing wave.

2.3.1 Reflection at a Dielectric Boundary

The following is a micro scale explanation of EM wave reflection upon the interface of two dielectric media. When an incident wave encounters a boundary of two

dielectric media, the wave is partially transmitted and partially reflected. The reflection and transmission coefficients may be calculated by applying EM boundary conditions at the dielectric boundary. According to Maxwell's equations, electric and magnetic fields have the following relationship:

$$B_0 = \frac{\hat{k} \times E_0}{v},$$

where:

E_0 = electric field magnitude;

B_0 = magnetic field magnitude;

$\hat{k}$ = unit vector pointing in direction of propagation;

v = phase velocity = $\omega/k = c/\sqrt{\varepsilon}$;

ω = angular frequency;

k = wavenumber = $2\pi/\lambda_g = \frac{\omega}{c}\sqrt{\varepsilon}$;

ε = effective dielectric constant.

Therefore, an incident wave propagating in the z direction has electric and magnetic wave fields,

$$\boldsymbol{E}(z,t) = E_i e^{j(k_1 \cdot z - \omega t)} \hat{\boldsymbol{x}},$$

$$\boldsymbol{B}(z,t) = \frac{E_i}{v_1} e^{j(k_1 \cdot z - \omega t)} \hat{\boldsymbol{y}},$$

reflected wave fields,

$$\boldsymbol{E}(z,t) = E_r e^{j(-k_1 \cdot z - \omega t)} \hat{\boldsymbol{x}},$$

$$\boldsymbol{B}(z,t) = \frac{E_r}{v_1} e^{j(-k_1 \cdot z - \omega t)} \hat{\boldsymbol{y}},$$

and transmitted wave fields,

$$\boldsymbol{E}(z,t) = E_t e^{j(k_1 \cdot z - \omega t)} \hat{\boldsymbol{x}},$$

$$\boldsymbol{B}(z,t) = \frac{E_t}{v_2} e^{j(k_2 \cdot z - \omega t)} \hat{\boldsymbol{y}},$$

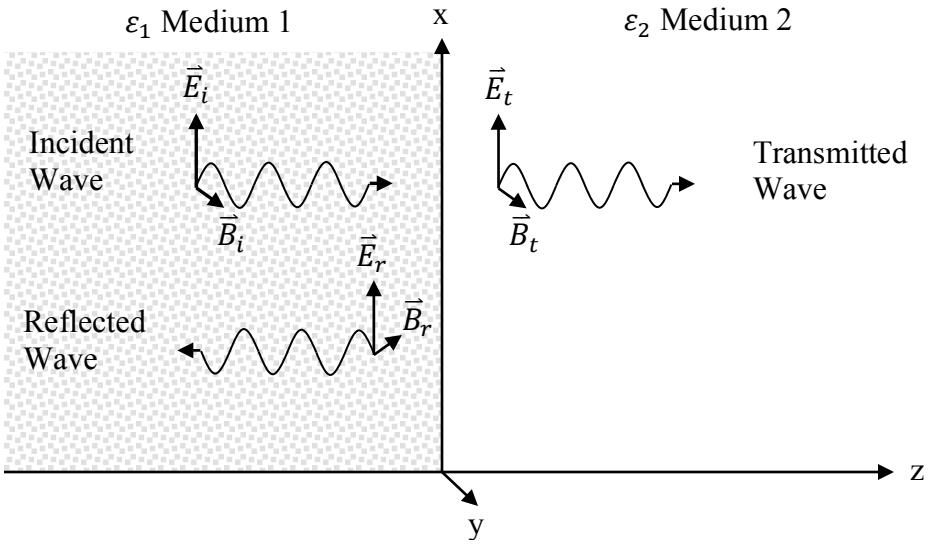

Figure 2.5: Incident and resulting reflected and transmitted waves at the boundary of two dielectric media.

The reflection coefficient Γ and transmission coefficient τ may be expressed as,

$$\Gamma = {}^{E_r}/_{E_i},$$

$$\tau = {}^{E_t}/_{E_i}.$$

Since the reflected and transmitted waves are produced from the incident wave,

$$E_i = E_r + E_t,$$

and by applying boundary conditions,

$$\frac{E_i - E_r}{v_1} = \frac{E_t}{v_2}.$$

By substituting the velocity factor with its previously stated definition we now have,

$$(E_i - E_r)\sqrt{\varepsilon_1} = E_t\sqrt{\varepsilon_2}$$

and by normalizing to the incident wave,

$$(1 - \Gamma)\sqrt{\varepsilon_1} = \tau\sqrt{\varepsilon_2}.$$

Finally, the reflection coefficient may be expressed in terms of the effective dielectric of the two materials,

$$\Gamma = \frac{\sqrt{\varepsilon_1}-\sqrt{\varepsilon_2}}{\sqrt{\varepsilon_1}+\sqrt{\varepsilon_2}},$$

and the transmission coefficient may be expressed as,

$$\tau = \frac{2\sqrt{\varepsilon_1}}{\sqrt{\varepsilon_1}+\sqrt{\varepsilon_2}}.$$

These results imply that a large dielectric contrast between the two materials yields a greater reflection coefficient, hence greater band-gap rejection. Also, since this reflection occurs at the interface of each periodic cell, it may be surmised that more periodic cells results in greater band-gap rejection.

Chapter 3
DESIGN

To reduce complexity and function solely as a proof of concept, a one-dimensional EBG structure using a microstrip topology was chosen. The microstrip line is the most common form of transmission medium in microwave electronics. Microstrip lines are well understood in operation and are easy to design and simulate. An EBG structure may be realized in a microstrip circuit when the effective dielectric constant along the microstrip line periodically repeats from high to low. One strategy [4] to accomplish this as previously shown, failed to provide precise band-gap frequency tuning. A unique and novel solution is needed.

3.1 Effective Dielectric Constant of a Microstrip Line

To devise a solution, first the factors which define a microstrip's effective dielectric constant ε_{eff} must be understood. A dielectric is an electrically insulating material that becomes polarized when introduced to an electric field. Like a spring that stores mechanical energy when stretched, a dielectric material stores electrical energy when an electric field is applied. A dielectric material is characterized by its dielectric constant, or relative permittivity ε_r, which describes its ability to store electric energy relative to the energy store in a vacuum under the same electrical field conditions.

In the context of a microstrip transmission line, effective dielectric constant is the relevant dielectric term. A microstrip line's electric field exists in more than one material; therefore its effective dielectric constant is based on the dielectric constants of the

materials in which the electric field exists. Other factors which determine a microstrip's effective dielectric constant is trace width, trace height, and substrate thickness. The following sections describe effective dielectric constant calculations for various microstrip line configurations.

3.1.1 Standard Microstrip Line

A standard microstrip line consists of a copper trace supported by a dielectric substrate. Electric fields above the trace exist in air and electric fields below the trace exist in the substrate. Therefore the effective dielectric will be greater than ε_{air} but less than $\varepsilon_{substrate}$. This is the most common configuration because of its ease of fabrication and design. Figure 3.1 shows the cross-section of a standard microstrip line.

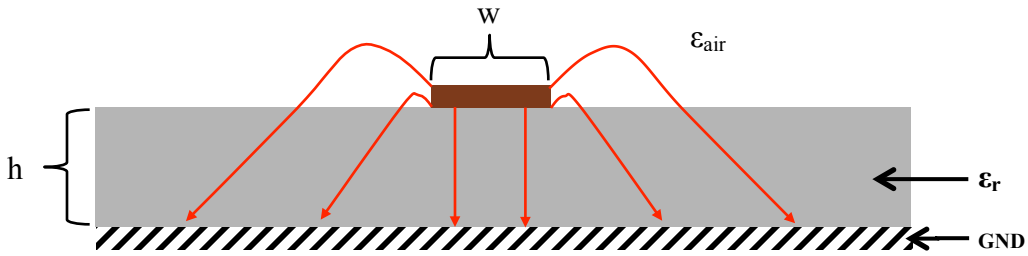

Figure 3.1: Cross-section of a standard microstrip line (electric field lines in red).

The effective constant for a standard microstrip may be calculated for the following two cases:

Case 1: $w \leq h$

$$\varepsilon_{eff} = \frac{\varepsilon_r+1}{2} + \frac{\varepsilon_r-1}{2}\left[\left(1+\frac{12h}{w}\right)^{-1/2} + 0.04\left(1-\frac{w}{h}\right)^2\right].$$

Case 2: $w > h$

$$\varepsilon_{eff} = \frac{\varepsilon_r+1}{2} + \frac{\varepsilon_r-1}{2}\left(1+\frac{12h}{w}\right)^{-1/2}.$$

This configuration does not prove to be useful in developing a tunable microstrip. According to the equations above, ε_{eff} is dependent on only ε_r, w, and h. The relative dielectric constant of the substrate cannot be manipulated because it is a solid material. The height of the substrate and the width of the trace cannot be easily adjusted either.

3.1.2 Two-Layer Substrate Microstrip Line

The next microstrip configuration investigated is a two-layer substrate microstrip. In this configuration the substrate is composed of two-layers of dielectric materials which differ in relative dielectric constant. Figure 3.2 below shows the cross-section of a two-layer substrate microstrip line.

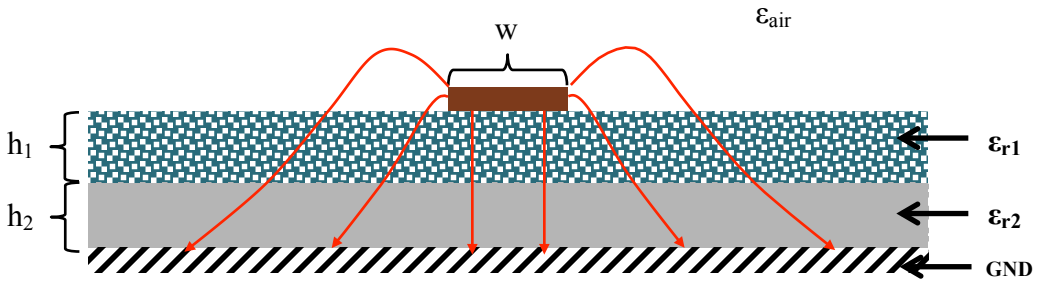

Figure 3.2: Cross-section of a two-layer substrate microstrip line (electric field lines in red).

Like the standard microstrip, the dielectric material above the trace is air. Analyzing a two-layer substrate microstrip is complex due to the fact that electric fields below the trace exist in two different substrates. A new method of calculating ε_{eff} must be used. The g-plane method models all dielectric materials (including air) as being under the microstrip trace. Each dielectric material's impact on the effective dielectric constant is determined by its filling factor q. Each dielectric's filling factor is the ratio of its cross-sectional area S in the g-plane to the total area S_C. The larger a material's filling factor,

the larger impact its dielectric constant has on the effective dielectric constant. Figure 3.3 illustrates the g-plane transformation.

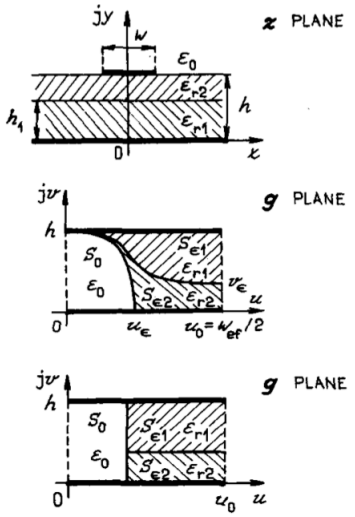

Figure 3.3: Z-plane to g-plane transformation for a two-layer substrate microstrip line [10].

The filling factors must first be calculated based on the two following cases. All variables reflect those in Figure 3.3.

Case 1: $w \leq h$

$$q_1 = \frac{ln\left(\frac{1+\frac{h_1}{h}}{1-\frac{h_1}{h}+\frac{w}{4h}}\right)}{2 \cdot ln\left(\frac{8h}{w}\right)} \cdot \left[1 + \frac{\pi}{4} - \frac{1}{2} arccos\left(\frac{h_1}{h} \cdot \frac{w}{8h} \sqrt{\frac{1+\frac{h_1}{h}}{1-\frac{h_1}{h}+\frac{w}{4h}}}\right)\right],$$

$$q_2 = \frac{1}{2} + \frac{0.9}{\pi \cdot \ln\left(\frac{8h}{w}\right)} - q_1.$$

Case 2: $w > h$

$$q_1 = \frac{1}{2} \cdot \frac{h_1}{h}\left[1 + \frac{\pi}{4} - \frac{h}{w_{eff}} ln\left(\frac{\pi}{h} \cdot w_{eff} \frac{\sin\left(\frac{\pi}{2} \cdot \frac{h_1}{h}\right)}{\frac{\pi}{2} \cdot \frac{h_1}{h}} + \cos\left(\frac{\pi}{2} \cdot \frac{h_1}{h}\right)\right)\right],$$

$$q_2 = 1 - q_1 - \frac{1}{2} \cdot \frac{ln\left(\frac{\pi}{h} w_{eff} - 1\right)}{\frac{w_{eff}}{h}},$$

where:

$$w_{eff} = w + \frac{2h}{\pi} ln\left[17.08\left(\frac{w}{2h} + 0.92\right)\right].$$

Now ε_{eff} may be calculated as,

$$\varepsilon_{eff} = 1 - q_1 - q_2 + \varepsilon_{r1}\varepsilon_{r2} \cdot \frac{(q_1 + q_2)^2}{\varepsilon_{r1}q_2 + \varepsilon_{r2}q_1}.$$

This is the configuration used in the grounded patch microstrip solution for a tunable EBG structure [4] when the patches are in a floating state. The two-layer substrate presents more tuning options over a single-layer substrate; however, adjusting the periodicity of a dielectric beneath the trace with precision is difficult. A third microstrip line configuration is investigated.

3.1.3 Microstrip line with Overlay

Overlay is a dielectric material situated on top of the microstrip line trace. Electric fields above the trace exist in the overlay and air while electric fields below the trace exist in the substrate. Like the two-layer substrate microstrip line configuration, g-plane filling factor analysis may be used to solve for ε_{eff}. Figure 3.4 shows the cross-section of a microstrip line with overlay and Figure 3.5 shows the g-plane transformation.

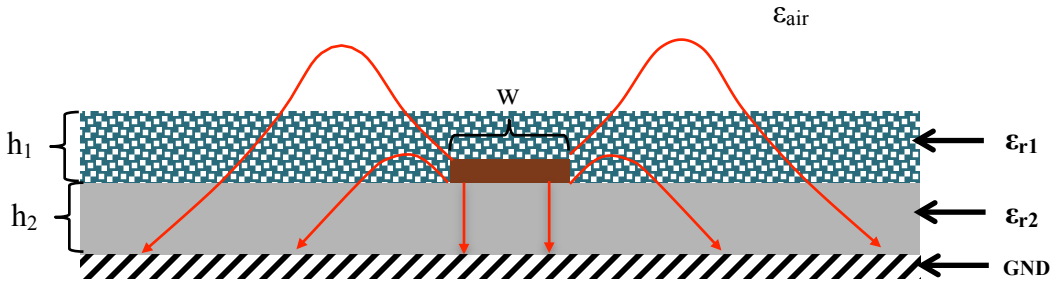

Figure 3.4: Cross-section of a microstrip line with overlay (electric field lines in red).

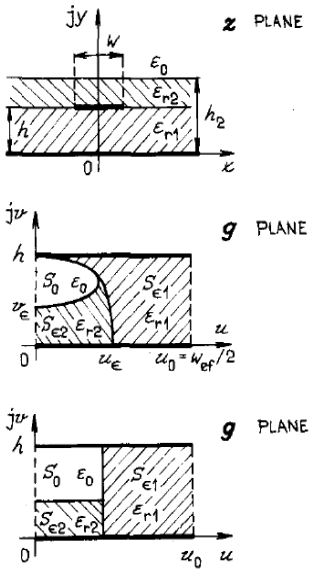

Figure 3.5: Z-plane to g-plane transformation for a microstrip line with overlay [10].

Case 1: $w \leq h$

$$q_1 = \frac{1}{2} + \frac{0.9}{\pi \cdot \ln\left(\frac{h}{w}\right)},$$

$$q_2 = \frac{1}{2} - \frac{0.9 + \frac{\pi}{4} ln\left(\frac{h_2/h+1}{h_2/h+w/4h-1}\right) \cdot arccos\left\{\left[1 - \frac{h}{h_2}\left(1 - \frac{w}{8h}\right)\right]\sqrt{\frac{h_2/h+1}{h_2/h+w/4h-1}}\right\}}{\pi \cdot ln\frac{8h}{w}}.$$

Case 2: $w > h$

$$q_1 = 1 - \frac{1}{2} \cdot \frac{ln\left(\frac{\pi}{h} w_{eff} - 1\right)}{\frac{w_{eff}}{h}},$$

$$q_2 = 1 - q_1 - \frac{1}{2} \cdot \frac{h - v_e}{w_{eff}} \cdot ln\left[\pi \cdot \frac{w_{eff}}{h} \cdot \frac{\cos\left(\frac{v_e}{2} \cdot \frac{\pi}{h}\right)}{\pi\left(\frac{h_2}{h} - \frac{1}{2}\right) + \frac{v_2}{2} \cdot \frac{\pi}{h}} + \sin\left(\frac{v_e}{2} \cdot \frac{\pi}{h}\right)\right],$$

where:

$$w_{eff} = w + \frac{2h}{\pi} ln\left[17.08\left(\frac{w}{2h} + 0.92\right)\right],$$

$$v_e = 2\frac{h}{\pi} arctan\left[\frac{\pi}{\frac{\pi}{2} \cdot \frac{w_{eff}}{h} - 2}\left(\frac{h_2}{h} - 1\right)\right].$$

Now ε_{eff} may be calculated as,

$$\varepsilon_{eff} = \varepsilon_{r1} q_1 + \varepsilon_{r2} \cdot \frac{(1-q_1)^2}{\varepsilon_{r2}(1-q_1-q_2)+q_2}.$$

This configuration presents new tunable possibilities which aren't possible with the two-layer substrate configuration. With the effective dielectric constant a product of the base substrate dielectric and overlay dielectric, only one material's periodicity needs to be adjusted to realize a tunable EBG structure. The easiest method is to keep a static base substrate to support the trace and adjust the periodicity of the overlay dielectric. The design will be based on this configuration. Next, methods for adjusting the periodicity of the overlay must be developed to fulfill the tuning mechanism requirements of the project.

3.2 Microstrip with Adjustable Overlay

By arranging the microstrip's overlay with periodic spacing along the trace, an EBG structure may be formed. Sections with overlay will have an effective dielectric constant greater than sections without overlay. A single periodic cell shall contain a section of microstrip with overlay and a section of microstrip without overlay.

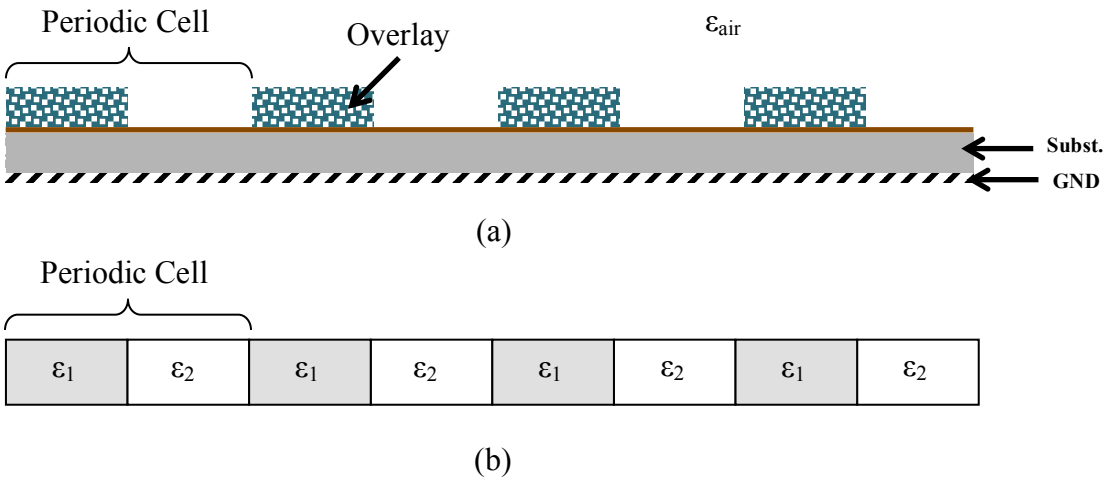

Figure 3.6: (a) Side view of microstrip line with periodic overlay. (b) Equivalent EBG structure model.

As proven by the equations in the previous section, a higher dielectric overlay results in a larger effective dielectric constant. Also it was shown that a larger dielectric contrast between ε_1 and ε_2 results in larger band-gap rejection. Combining these two results suggests that a low dielectric substrate and high dielectric overlay produces large band-gap rejection. These results provide a foundation for the design of the device.

3.2.1 Choosing Dielectric Substrates and Overlay

As previously stated, best band-gap rejection results are obtained when high dielectric periodic overlay is used on a low dielectric substrate.

Dielectric Substrates: To prove the theory that a low dielectric substrate yields larger band-gap rejection, both a low dielectric and high dielectric substrate shall be tested. Rogers Duroid® 5880LZ was chosen to represent the low dielectric substrate while Rogers Duroid® 3006 was chosen for the higher dielectric substrate. Rogers Duroid® 5880LZ is filled with a PTFE composite reinforced with glass microfibers and features low dielectric loss and uniform operation over high frequency range [11]. Rogers Duroid® 3006 combines PTFE/ceramic layers with PTFE/woven glass and also features high frequency operation [12]. Table 3. highlights some key properties of these two substrates.

Table 3.1: Rogers Duroid® 5880LZ and Duroid® 3006 properties.

	Typical Value Duroid® 5880LZ	Typical Value Duroid® 3006	Condition
Dielectric Constant ε_r	1.96±0.04	6.15±0.15	10 GHz 23°C
Dissipation Factor, tan δ	0.0019	0.002	10 GHz 23°C
Density gm/cm^3	1.4	2.6	

Both substrates were ordered in 12”x9” sizes with 50 mil thickness. The substrates feature double sided 1oz. copper cladding.

Dielectric Overlay: To obtain greatest band-gap rejection possible, a high dielectric overlay must be chosen. A limiting factor in choosing the overlay material is the size it is available in. An ideal overlay candidate has a high dielectric constant, is light in weight (may be easily moved), and is available in various shapes and sizes. Unfortunately high dielectric (or refractive index) materials tend to have higher densities. Figure 3.7 shows this relationship for 4000 various materials.

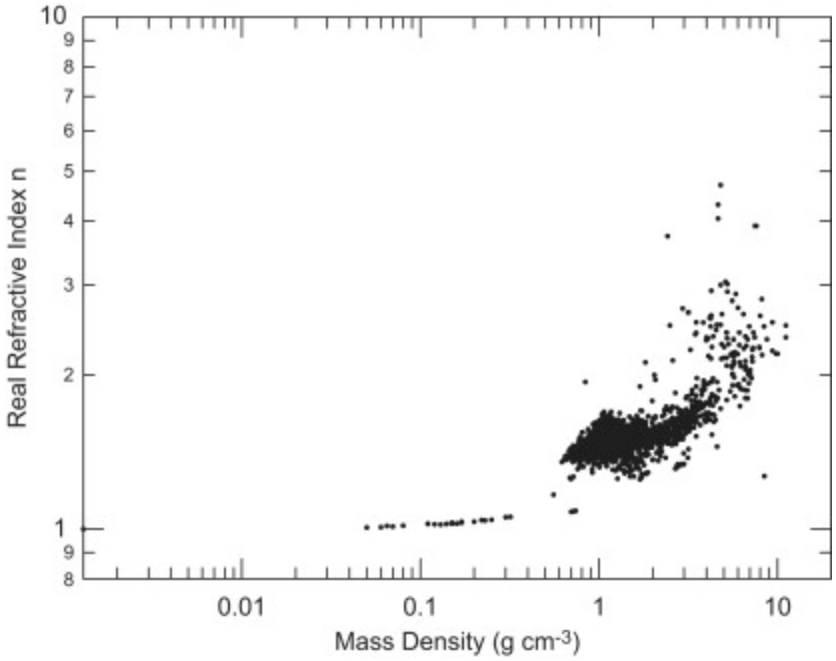

Figure 3.7: Relationship between refractive index and mass density for 4000 various materials including gases, liquids, and solids [13].

Alumina, or aluminum oxide, was chosen as a good overlay material for its high dielectric constant, non-conductivity, moderate mass density, and wide availability in shape and size. Alumina is a common ceramic which is known for its hardness; it is nearly as hard as diamond. Table 3. shows some of alumina's properties.

Table 3.2: Properties of alumina [14].

	Typical Value	**Condition**
Dielectric Constant ε_r	9.5	1 GHz 20°C
Resistivity Ω·cm	$>10^{14}$	20°C
Density gm/cm^3	3.88	

Alumina is manufactured in square and circular shaped rods which can be used to move along the microstrip trace to adjust the overlay periodicity. Circular rods may roll along the microstrip trace while square rods must be pushed/pulled. Various sizes of both

circular and square 99.8% pure alumina rods were ordered from Ortech Advanced Ceramics. Below, in Table 3., is an ordered parts list:

Table 3.3: List of ordered parts from Ortech Advanced Ceramics.

Part	Size	Price
Alumina 99.8% Circular Rod	3/8" x 12" Long	$42.54
Alumina 99.8% Circular Rod	1/4" x 12" Long	$36.06
Alumina 99.8% Circular Rod	1/8" x 12" Long	$26.31
Alumina 99.8% Square Rod	¼" x 12" Long	$49.29
Alumina 99.8% Square Rod	1/8" x 12" Long	$31.62

Each 12" long rod may be cut into smaller sections to create the individual overlay elements.

3.2.2 Calculation of Effective Dielectric Constant for Design Materials

Using the previously stated equations, the effective dielectric constant of sections of microstrip with and without overlay may be calculated. These calculations were performed for both base substrates chosen, and for alumina overlay. The results are tabulated below in Table 3..

Table 3.4: ε_{eff} calculation results for various overlay configurations.

Base Substrate	Alumina Overlay Size	q_1	q_2	Non-Overlay ε_{eff}	Overlay ε_{eff}	Dielectric Contrast
Duroid® 5880LZ	1/8" square	0.7522	0.2217	1.7029	2.7346	1.6058
	1/4" square	0.7522	0.2416	1.7029	3.4615	2.0327
Duroid® 3006	1/8" square	0.6764	0.3117	4.4282	6.5573	1.4808
	1/4" square	0.6764	0.3214	4.4282	7.1556	1.6159

These calculations reveal that a microstrip section with larger (taller) overlay has a larger impact on ε_{eff} since the fill factor q_2 is larger for ¼" square overlay. This result is also reflected by the fact that the ¼" square overlay sections have a larger ε_{eff}. Maximum dielectric contrast between overlay and non overlay microstrip sections occurs for Duroid® 5880LZ with ¼" square overlay. Therefore this configuration should yield largest band-gap rejection.

3.3 Tuning Operation

EBG theory states that the center band-gap wavelength is proportional to the dielectric periodicity; therefore center band-gap frequency is inversely related to dielectric periodicity. Moving the overlay elements closer to each other decreases the period spacing, while moving them apart increases the period spacing. This is the function in which the band-gap frequency will be tuned.

Using a rod as a single overlay elements means that the fill factor of each periodic cell will not always be 50%. Fill factor is the ratio of the length of the period with overlay to the total length of the period. A fill factor of 50% means half of the periodic cell is composed of ε_1 and the other half is composed of ε_2. Fill factor will be 50% only when the period is twice the size of the overlay rod. The effects of varying fill factor will be discovered through simulation and testing. The most critical tuning parameter, however, is the dielectric periodicity. This shall be controlled by adjusting the spacing of the overlay rods.

Shown below is an illustration of two configurations with different period spacing. The configuration in Figure 3.0.8 (a) has greater spacing than Figure 3.0.8 (b) and will exhibit a lower band-gap frequency.

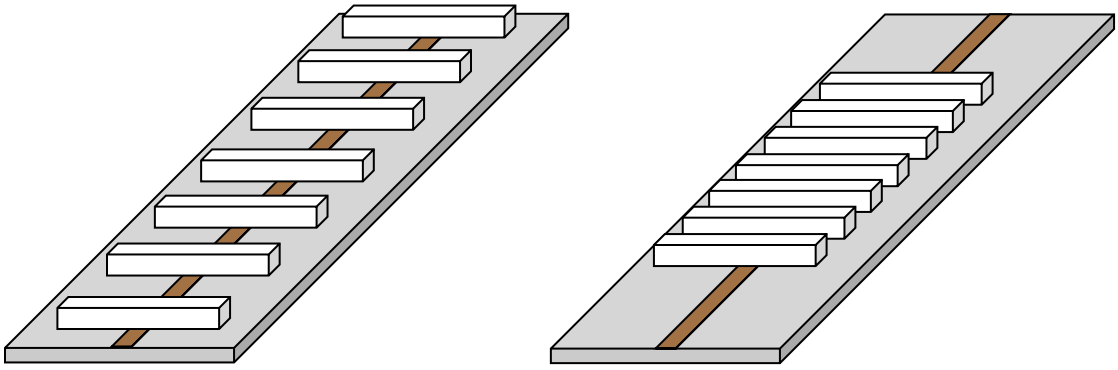

(a) (b)

Figure 3.8: (a) Overlay configuration for a low frequency band-gap. (b) Overlay configuration for a high frequency band-gap.

3.4 Overlay Adjusting Mechanism

A system which can adjust the periodicity of the overlay must be contrived. This tuning mechanism must be periodic in structure and its periodicity must be adjustable. It is vital that the spacing between each overlay elements is the same to ensure consistent periodicity. Two mechanisms which differ in complexity are proposed.

3.4.1 Acoustic Standing Wave Tuning Mechanism

An acoustic wave is a periodic structure which may be controlled using an acoustic transducer or speaker; therefore, it fits the identity of the desired overlay adjusting mechanism. An acoustic wave propagates through air by compressing and decompressing air molecules creating areas of high pressure and low pressure. These periodically repeating high and low pressure regions may be used to control the placement of the overlay rods. Longitudinally traveling waves cannot be used as the high

and low pressure areas cannot be controlled, so the wave must be stationary. A stationary wave, called a standing wave, is created when two waves traveling in opposing directions combine to produce a wave that has no propagating energy. In a standing wave, nodes are areas where the pressure does not change, and anti-nodes are areas where pressure fluctuates from maximum to minimum. An acoustic standing wave may be created by introducing an acoustic source to an open or closed end tube. Here, acoustic waves travel through the tube and are reflected off of the open/closed end. The reflected waves combine with incident waves to form a standing wave. A standing wave of wavelength λ is produced in an open/closed end tube of length L when the following conditions in Table 3. are met.

Table 3.5: Acoustic standing wave tube conditions.

Tube Type	Standing Wave Conditions	Modes
Closed-Closed	$\lambda_m = \frac{2L}{m}$	$m = 1,2,3 \ldots$
Open-Open	$\lambda_m = \frac{2L}{m}$	$m = 1,2,3 \ldots$
Closed-Open	$\lambda_m = \frac{4L}{m}$	$m = 1,3,5 \ldots$

The pressure distribution for the first three standing wave modes of each tube type is shown in Figure 3.9.

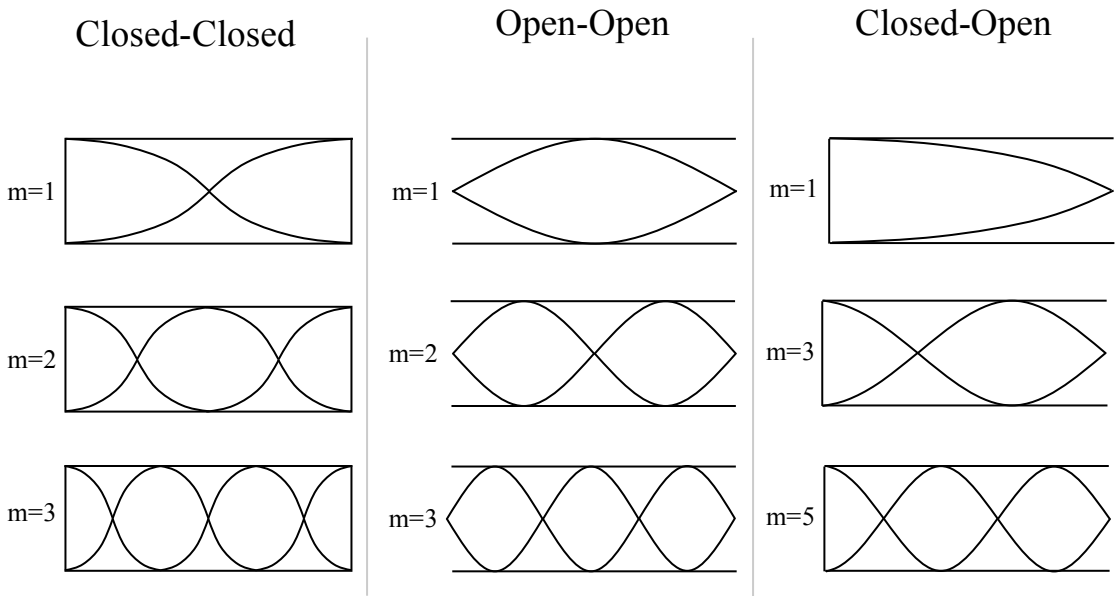

Figure 3.9: Acoustic standing wave pressure distribution for three tube types and three modes.

As shown in Figure 3.9, pressure variation is greatest at closed ends (anti-nodes), and pressure remains constant at atmospheric pressure at open ends (nodes). Since pressure at the nodes is unchanging, any objects inside the tube will attract towards the nodes. Conversely, any objects at anti-nodes locations will be pushed away as pressure fluctuates from high to low. This behavior has been proven in many experiments as a means to visualize sound waves. It was first demonstrated in 1866 by a German Physicist named August Kundt [15]. This demonstration is known as Kundt's tube. In a Kundt's tube a lightweight material in powder or small particle form is placed in a transparent standing wave tube. The material will build up at the nodes and stray from the anti-nodes. A common material used in this experiment is small Styrofoam balls as shown in Figure 3.10.

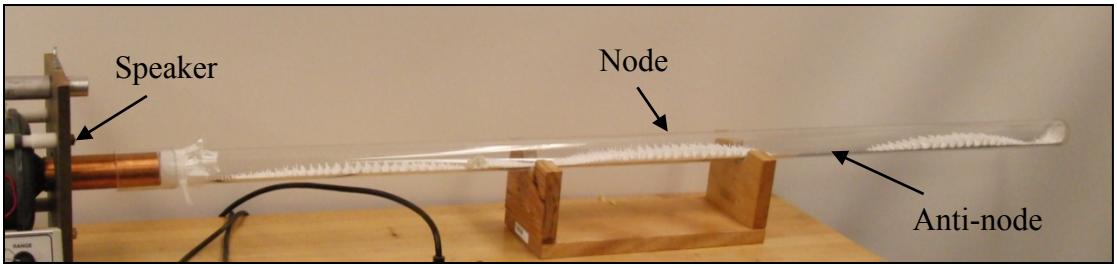

Figure 3.10: Kundt's tube with a third mode standing wave [16].

The Kundt's tube in Figure 3.10 is a closed-closed tube configuration with a third mode standing wave. The Styrofoam balls accumulate at the nodes and no Styrofoam balls are present at the anti-nodes.

A Kundt's tube-like mechanism could theoretically be used to adjust the location of the overlay rods on the microstrip line. Instead of moving Styrofoam balls, the standing wave would move the overlay rods. When placed in a standing wave tube, rods should move to the nodes, which are spaced with perfect periodicity, to create an EBG structure in the microstrip line. Adjusting the acoustic frequency of the speaker/transducer will change the periodicity of the nodes and overlay. Therefore, the frequency of the speaker/transducer directly affects the band-gap frequency.

Since the ceramic rods are much denser than Styrofoam, circular rods will be used as the overlay elements to roll along the microstrip line. The effects of using circular overlay elements opposed to square will be discussed in the simulation. Below is an illustration of how the acoustic standing wave interacts with the overlay.

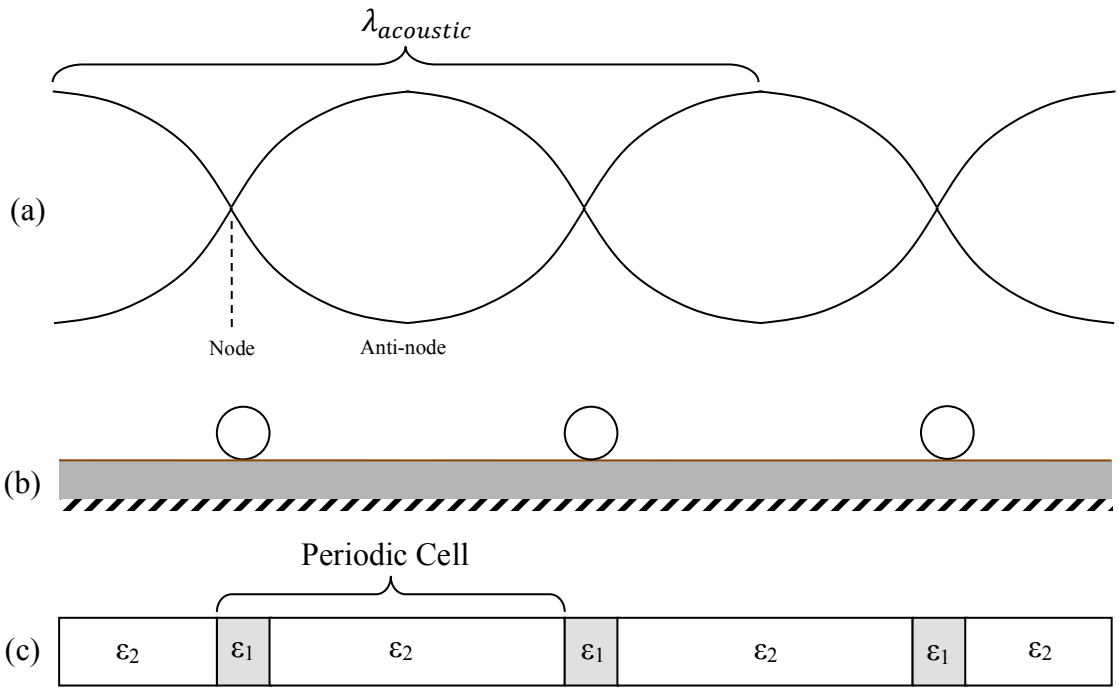

Figure 3.11: Relationship between (a) acoustic standing wave pressure distribution, (b) overlay rods on microstrip line, and (c) equivalent EBG structure model.

Since standing waves occur in discrete modes for a tube of a given length, the tube length must be adjustable to realize any acoustic frequency. This may be accomplished by adding an extension tube to be fitted on the inside of the acoustic tube which may slide in and out to effectively adjust the length of the acoustic tube. The following parts were selected to create the acoustic standing wave tube system:

Clear Acoustic Tube: A clear acrylic tube with a 2 ¼" outer diameter and 2" inner diameter was obtained from Tap Plastics. Three 2' long sections were ordered. When cut, the microstrip line substrate must be less than 2" wide to fit inside of the tube.

Extension Tube: An 18" long cardboard mailing tube with a 2" outer diameter was obtained to fit inside the acrylic tube. A portion of this tube shall be used to add length to the acoustic tube when necessary. Both tubes are shown in Figure 3.12.

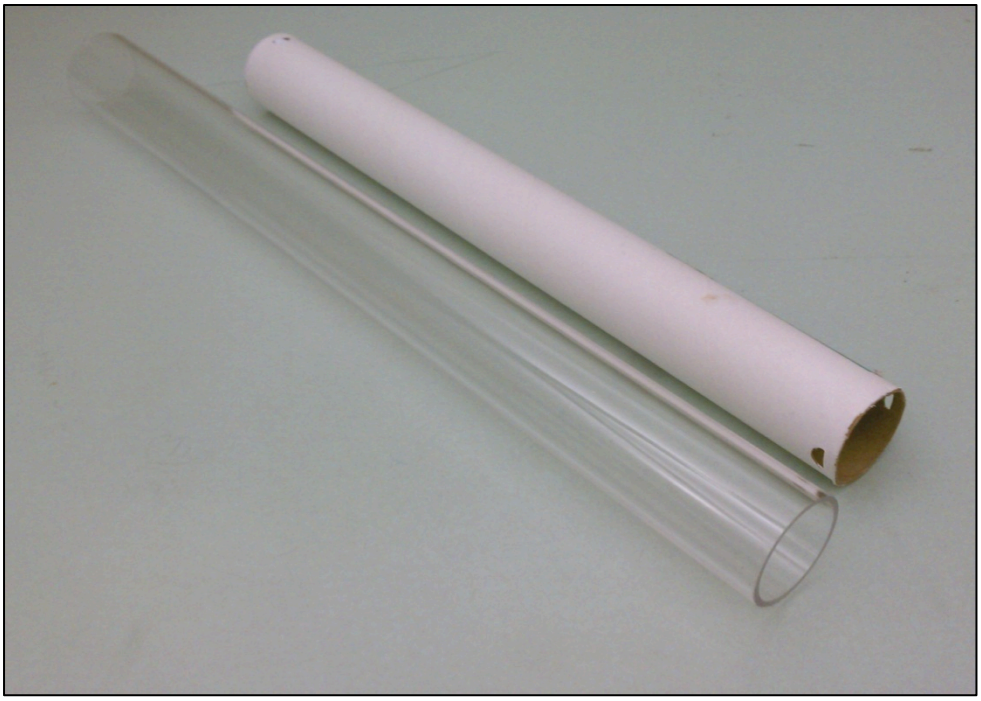

Figure 3.12: Clear acrylic tube and cardboard mailing tube.

Computer Speaker: A computer speaker was chosen as the acoustic source to avoid the need to obtain a standalone speaker and amplifier. The speaker chosen is an Altec Lansing ACS90 which has an output power capability of 4.5W and a frequency response of 90Hz-20kHz [17].

A difficult design question is: how much pressure is required to move the overlay rods? It is difficult to quantify this value because many factors such as air density and various frictions must be considered. Outside of moving small particles or powders for visual purposes, there are no known cases of an acoustic standing wave tube being used to move or arrange objects for a specific application. This thesis aims to determine the pressure required to move the overlay rods in acoustic standing wave tube.

Pressure, when used in the context of sound is called sound pressure level (SPL). SPL, or L_p, is rated on a decibel scale and can be related to pressure by the following,

$$L_p = 10\log_{10}\left(\frac{{p_{rms}}^2}{{p_{ref}}^2}\right) = 20\log_{10}\left(\frac{p_{rms}}{p_{ref}}\right),$$

where:

p_{rms} = rms pressure (pascals),

$p_{ref} = 20\mu Pa$ = rms reference pressure (pascals).

The following table, Table 3., demonstrates the sound pressure levels and corresponding sound pressures for various sound sources.

Table 3.6: Table of sound levels and corresponding sound pressure for various sound sources [18].

Table of sound levels L (loudness) and corresponding sound pressure and sound intensity			
Sound Sources Examples with distance	Sound Pressure Level L_p dBSPL	Sound Pressure p N/m^2 = Pa	Sound Intensity I W/m^2
Jet aircraft, 50 m away	140	200	100
Threshold of pain	130	63.2	10
Threshold of discomfort	120	20	1
Chainsaw, 1 m distance	110	6.3	0.1
Disco, 1 m from speaker	100	2	0.01
Diesel truck, 10 m away	90	0.63	0.001
Kerbside of busy road, 5 m	80	0.2	0.0001
Vacuum cleaner, distance 1 m	70	0.063	0.00001
Conversational speech, 1 m	60	0.02	0.000001
Average home	50	0.0063	0.0000001
Quiet library	40	0.002	0.00000001
Quiet bedroom at night	30	0.00063	0.000000001
Background in TV studio	20	0.0002	0.0000000001
Rustling leaves in the distance	10	0.000063	0.00000000001
Threshold of hearing	0	0.00002	0.000000000001

The SPL produced by a speaker is determined by its sensitivity. A speaker's sensitivity, rated in dB, is the SPL (dB) produced at 1 meter from the speaker for 1 watt of input power. While the sensitivity of the ACS90 speakers is not documented, typical speaker sensitivity is 84dB [19]. Assuming this is the speaker's sensitivity rating, at maximum power (4.5W) the speaker will produce an SPL of about 97dB. The effects of confining the speaker's sound waves into a tube will be discovered in experimentation.

3.4.2 Mechanical Tuning Mechanism

The second tuning mechanism involves a simpler approach. The design objective is to construct a mechanical device which can physically move the overlay while maintaining consistent periodicity between elements. A few designs were considered before an acceptable solution was reached. They are listed below:

Coil spring: A coil spring is a periodic mechanical device that can change in periodicity when stretched. A spring's periodicity comes from its helical turns which are spaced with equal distance from each other. Springs have a natural state in which they have a certain periodicity when left undisturbed. However, when stretched, helical turns move further from each other but still maintain periodic spacing. If overlay elements can be attached to helical turns in a spring, it could be used as a tuning mechanism.

The difficulty in using a spring as a tuning mechanism is developing a way to attach overlay elements to the spring itself. Springs are usually circular in cross-section and helical in form, making it difficult to attach overlay rods. There is also difficulty in mounting the spring system to the microstrip circuit board while still allowing it to be stretched. Other mechanical devices must be investigated

Rubber band: Rubber bands, like springs, are elastic structures which can change in periodicity when stretched. A rubber band may be cut to form an elastic string. Any two points along this piece of elastic will be separated by a distance proportional to the amount the elastic is stretched. If overlay elements are attached along the elastic with equal spacing, they should remain separated with consistent periodicity when the elastic is stretched.

While an elastic string is less complex than a spring, it has the same faults as the spring. It would be difficult to attach overlay elements to the elastic because every part of the elastic stretches; anywhere that the overlay elements would be attached would also stretch. This makes using adhesives for attaching overlay elements not plausible. Another challenge is initially placing the overlay elements. Any slight deviation from perfect periodicity in initial placement of the overlay would be proliferated when the elastic is stretched. Next, a non-elastic mechanical structure is investigated.

Mechanical Arm: A non-elastic, periodic, and adjustable, mechanical device is needed. Since such a device is not elastic, it must be able to extend and retract. A device which fits this profile is an extendable mechanical arm. An extendable mechanical arm is made of criss-crossing supports which are joined in a manner that allows the system to extend and contract. This type of apparatus is known as a pantograph. Figure 3.13 shows a basic mechanical arm pantograph at three extension lengths.

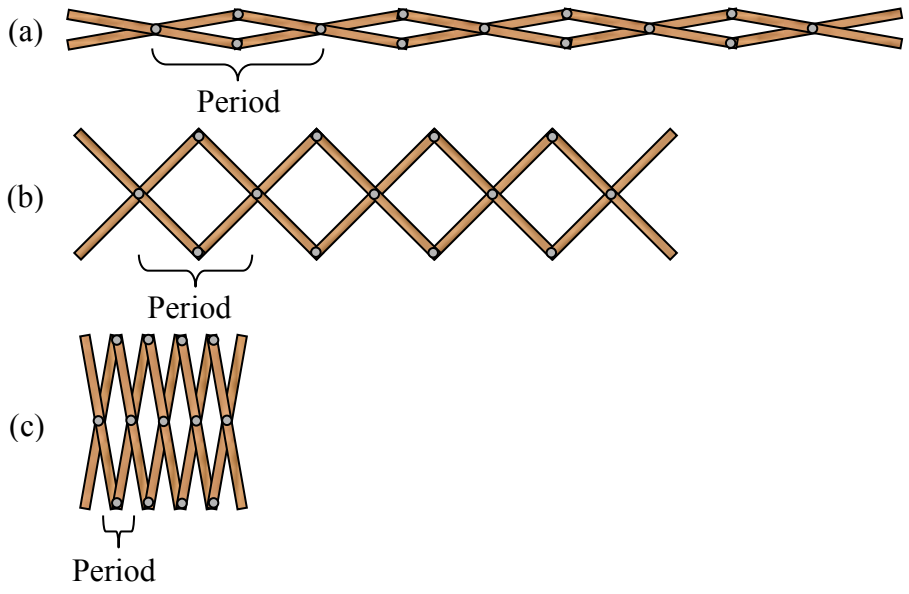

Figure 3.13: (a) Fully extended arm, (b) moderately extended arm, (c) contracted arm.

The periodicity in the device comes from the middle joints which are evenly spaced along the mechanical arm. This device can be used as an overlay tuning mechanism if the overlay elements are attached to the middle joints. Extending the arm would effectively adjust the periodicity of the overlay.

Unlike the elastic mechanisms, attaching the overlay elements to this device is simple. Overlay elements can be adhered to the joint heads. The difficulty in using this device comes from constructing it. All criss-crossing supports must be identical for the device to operate with perfect periodicity. There are no other inherent problems with this device as an overlay adjusting mechanism; therefore its design will be selected as a mechanical solution.

Chapter 4
SIMULATION

Simulations were completed using Agilent's Advanced Design System (ADS). ADS is an electronic design simulator which specializes in high frequency design. ADS meets the needs for simulating overlay microstrip lines, however it cannot be used to model circular overlay elements. A technique for approximately modeling circular overlay in ADS was developed and used in simulation.

4.1 Modeling an EBG Microstrip Structure with Overlay in ADS

The EBG microstrip structure consists of periodically repeating sections of a microstrip line with and without overlay. This may be modeled in ADS by connecting a series of microstrip lines which are set to overlay and non-overlay substrates in an alternating manner. A microstrip substrate may be modeled in ADS by using the 'MSUB' function where the user can specify parameters such as: substrate height, relative dielectric constant, loss tangent, and trace height. A substrate with overlay is modeled by using 'MLSUB' a multi-layer (three layer) substrate. Although there are only two dielectric substrates in 'MLSUB', the three layers refer to the three interfaces which bound the two substrates. The bottom layer is the ground plane, the middle layer (between the two substrates) is the microstrip trace (referred to as 'signal'), and the top layer is air ('blank'). The base dielectric substrate is the bottom substrate, and the overlay is the top substrate.

As per design specifications, the microstrip line ('MLIN') must be designed to have a characteristic impedance of 50Ω. This is achieved by setting the correct line

width. ADS has a tool called 'LineCalc' which calculates the trace width required to yield a characteristic impedance of 50Ω for a given substrate. The trace widths for the two substrates are shown below in Table 4..

Table 4.1: 'LineCalc' results for 50Ω trace width for Duroid®5880LZ and Duroid® 3006.

Substrate	Relative Dielectric Constant (ε_r)	50Ω Trace Width
Duroid® 5880LZ	1.96	165 mils
Duroid® 3006	6.15	74 mils

The lengths of the microstrip lines with overlay should reflect the width of the overlay elements. The lengths of the microstrip lines with no overlay should be set to yield to desired periodicity. An ADS schematic for an EBG microstrip structure with 6 periods of ¼" square alumina rods and a periodicity of 1000mils on a Duroid® 5880LZ substrate is shown in Figure 4.1. The S_{21} response of this circuit is shown in Figure 4.2.

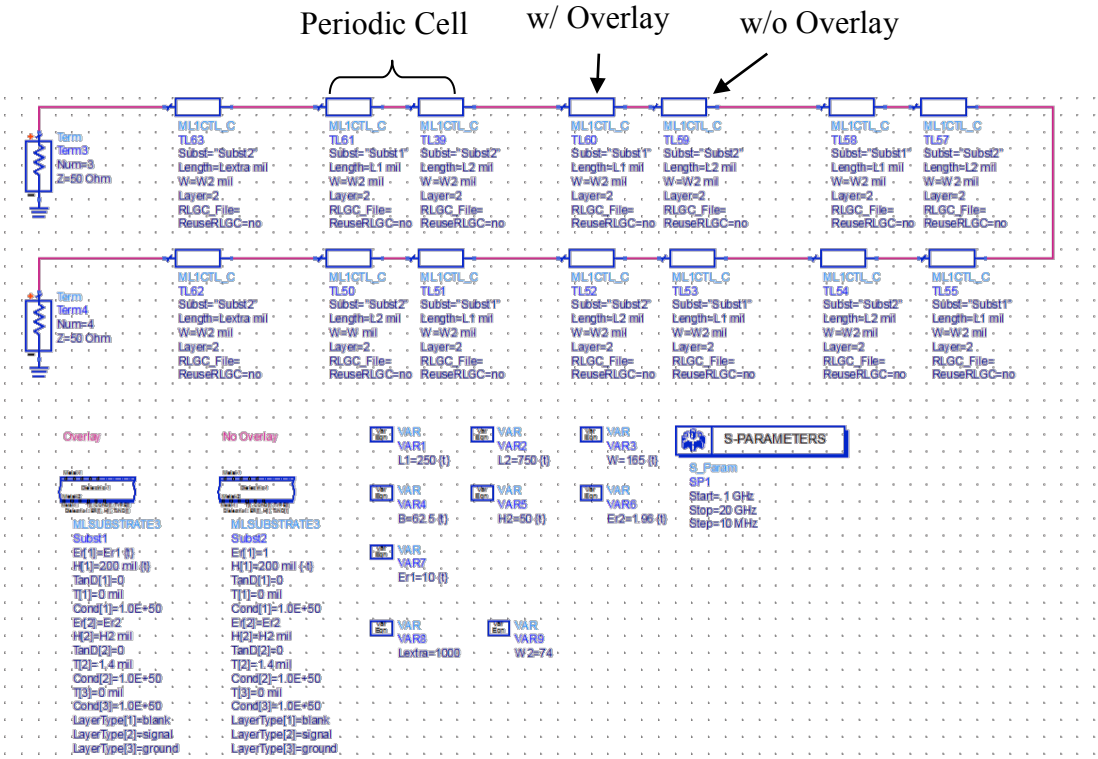

Figure 4.1: ADS Schematic for an EBG microstrip circuit (Periodicity=1000mils, # Periods = 6, Overlay = ¼" square alumina rods, substrate = Duroid® 5880LZ).

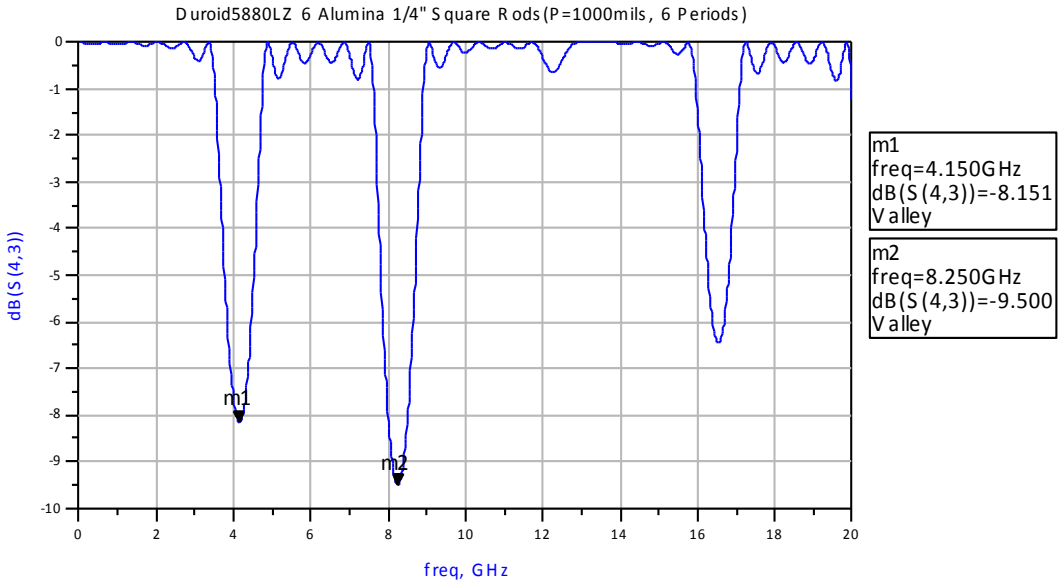

Figure 4.2: ADS Simulated S(2,1) response for circuit in Figure 4.1.

4.1.1 Approximation Technique for Modeling Circular Overlay

Since circular overlay is an unconventional and novel concept, there is no integration in ADS to support it. However, a technique for approximating a circular

overlay element in ADS was developed. A circular shape can be divided into discrete sections; the more sections, the better the approximation. For example, in Figure 4.3 a circle is divided into 7, 5, and 3 sections.

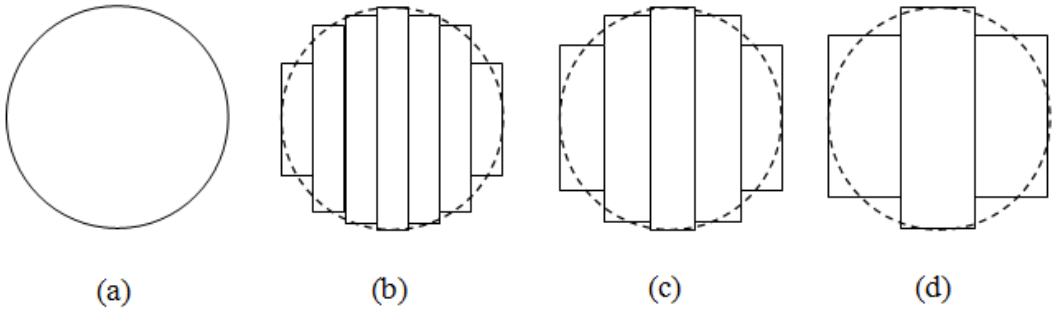

Figure 4.3: (a) An undivided circle, (b) divided into 7 sections, (c) divided into 5 sections, (d) divided into 3 sections.

This approximation technique may be implemented in ADS by modeling each discrete section individually and connecting them in series to form an approximate circle. This requires using a four layer microstrip (3 substrate layers) because for some discrete sections there is an air gap (ε_{air}) between the trace and the overlay substrate. The schematic in Figure 4.4 shows an approximate circle overlay representation in ADS using 5 sections.

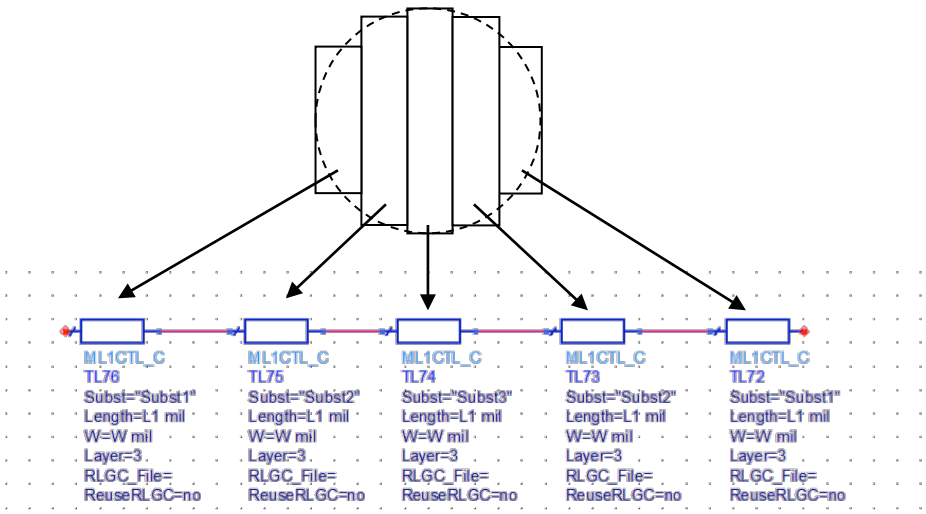

Figure 4.4: ADS approximation of a microstrip line with circular overlay divided into 5 discrete sections.

4.2 Effect of Periodicity and Number of Periods

The effects of periodicity and number of periodic cells in an EBG structure were established previously in the discussion of EBG theory. The theory states that periodicity directly influences band-gap wavelength in a proportional manner, hence an inverse relationship to band-gap frequency. Also, it has been affirmed that the number of periodic cells in an EBG directly affects the band-gap rejection. These theories are tested through simulation.

4.2.1 Effect of Periodicity

To determine the effect of periodicity on the EBG microstrip structure, various simulations will be executed with all factors constant except for periodicity. Identical tests shall be performed for both Duroid® 5880LZ and Duroid® 3006 base substrates. The constant test conditions are: 10 periods, alumina overlay ($\varepsilon_r = 9.8$), fill factor of 50% (half of periodic cell has overlay). Results are shown below:

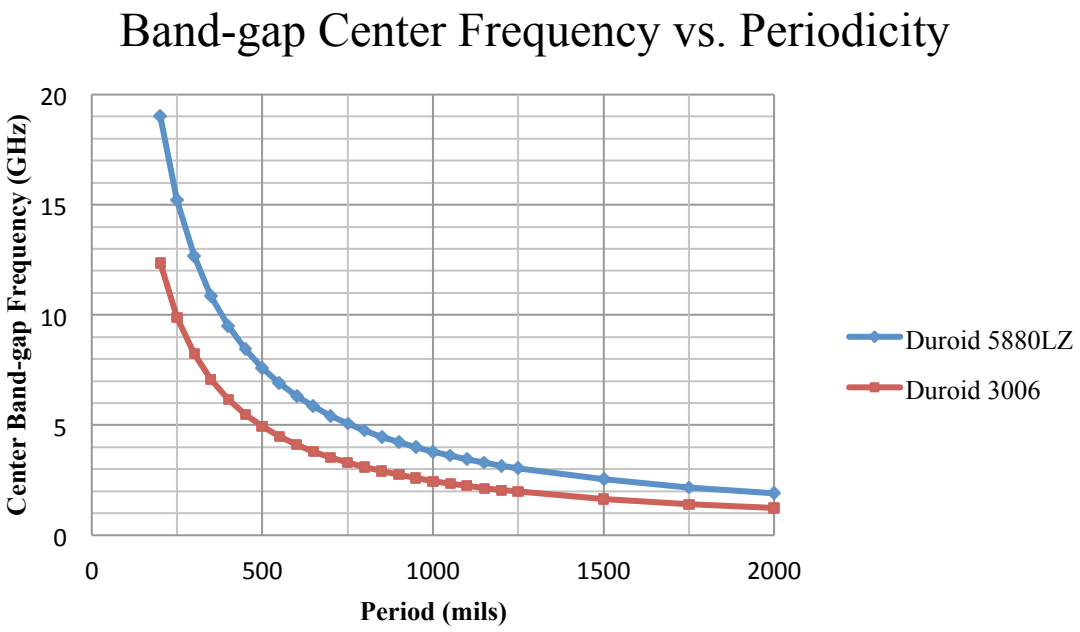

Figure 4.5: Effect on periodicity on band-gap center frequency.

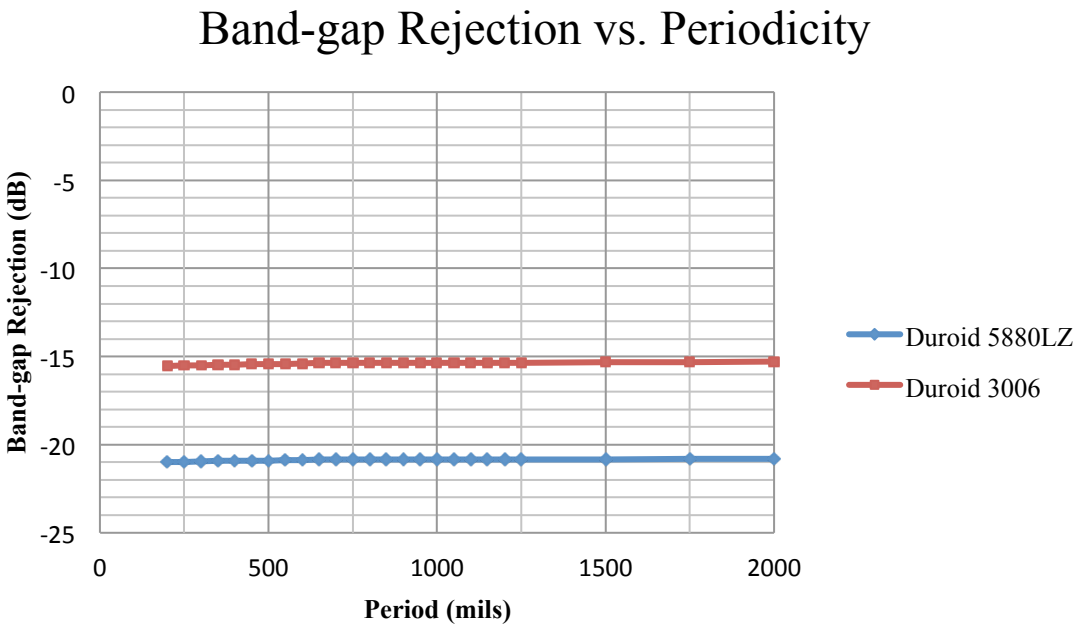

Figure 4.6: Effect of periodicity on band-gap rejection.

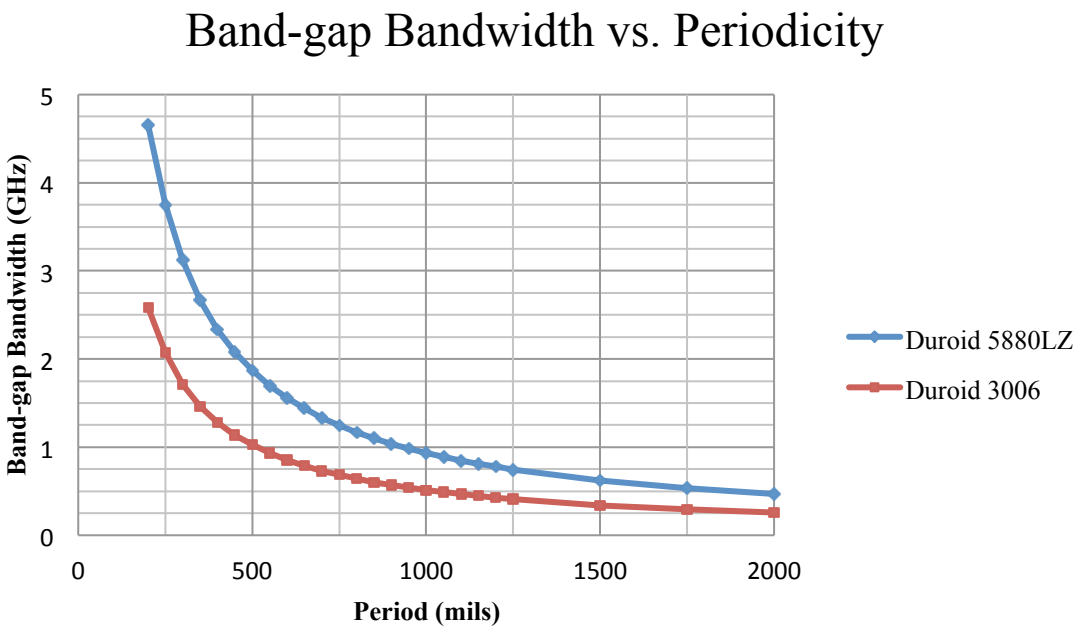

Figure 4.7: Effect of periodicity on band-gap bandwidth.

Results in Figure 4.5 confirm that simulation agrees with the theory that band-gap frequency decreases as the periodicity of an EBG structure increases. The relationship appears to be exponential. Figure 4.6 results show that periodicity has no affect on changing the band-gap rejection.

These results also agree with the previously derived theory that larger dielectric contrast between repeating dielectric elements results in greater band-gap rejection. Duroid® 5880LZ has a lower relative dielectric constant ($\varepsilon_r = 1.96$) compared to Duroid® 3006 ($\varepsilon_r = 6.15$), therefore it has a greater contrast in effective dielectric constant between elements with and without overlay. As shown in Figure 4.6, the simulation using Duroid® 5880LZ has >5dB band-gap rejection than Duroid® 3006.

A third result, in Figure 4.7, shows that the band-gap bandwidth's relationship with periodicity is identical to that of band-gap frequency. While this relationship wasn't

derived, it can be explained. All frequencies are reflected at the interface between periodic cells. However, the band-gap frequency is special because it is the frequency where a standing wave occurs, causing cancelation of wave propagation through the EBG structure. The reflection coefficient for frequencies which deviate slightly from the band-gap frequency (bandwidth frequencies/wavelengths) will be slightly less than that of the band-gap frequency. Therefore a standing wave won't be produced, but there will still be slight wave propagation. This is why the band-gap has bandwidth and is not a perfect notch at the band-gap frequency. Band-gap bandwidth follows a similar relationship as band-gap center frequency does with periodicity. This is because for a small period spacing configuration, wavelengths which deviate slightly from the band-gap frequency but still cause rejection (bandwidth wavelengths) are smaller (higher frequency).

4.2.2 Effect of Number of Periods

Given that there is a reflection at each periodic cell boundary, more periods should result in larger band-gap rejection. This theory is tested by performing simulations for both Duroid® 5880LZ and Duroid® 3006 where the number of periods is varied and all other conditions are constant. The constant test conditions are: periodicity of 500mils, alumina overlay ($\varepsilon_r = 9.8$), fill factor of 50% (half of periodic cell has overlay). Results are shown on the following pages.

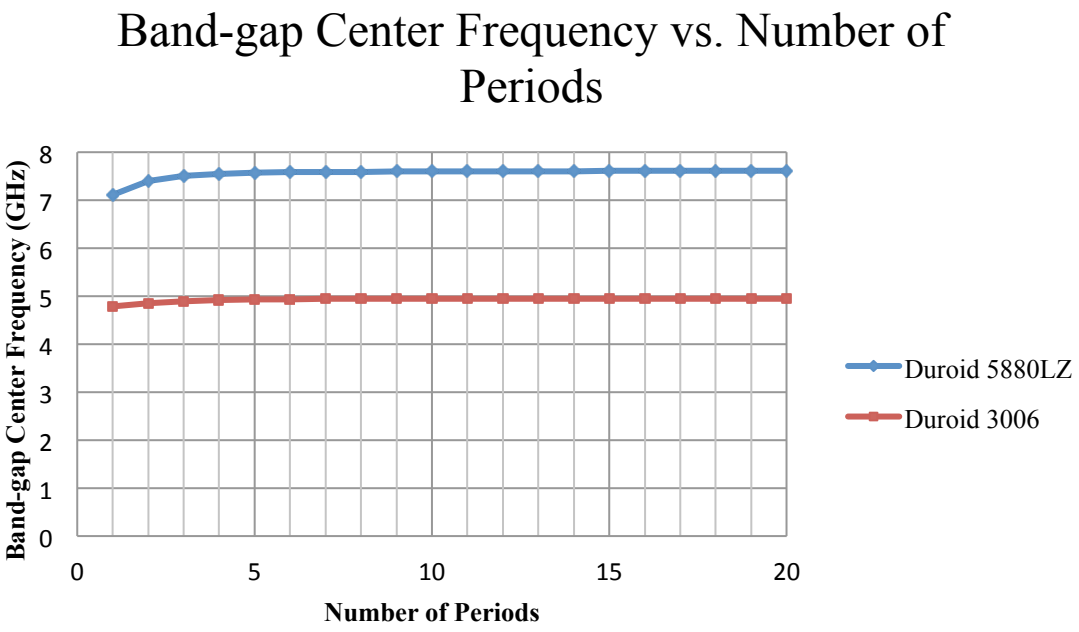

Figure 4.8: Effect of number of periods on band-gap center frequency.

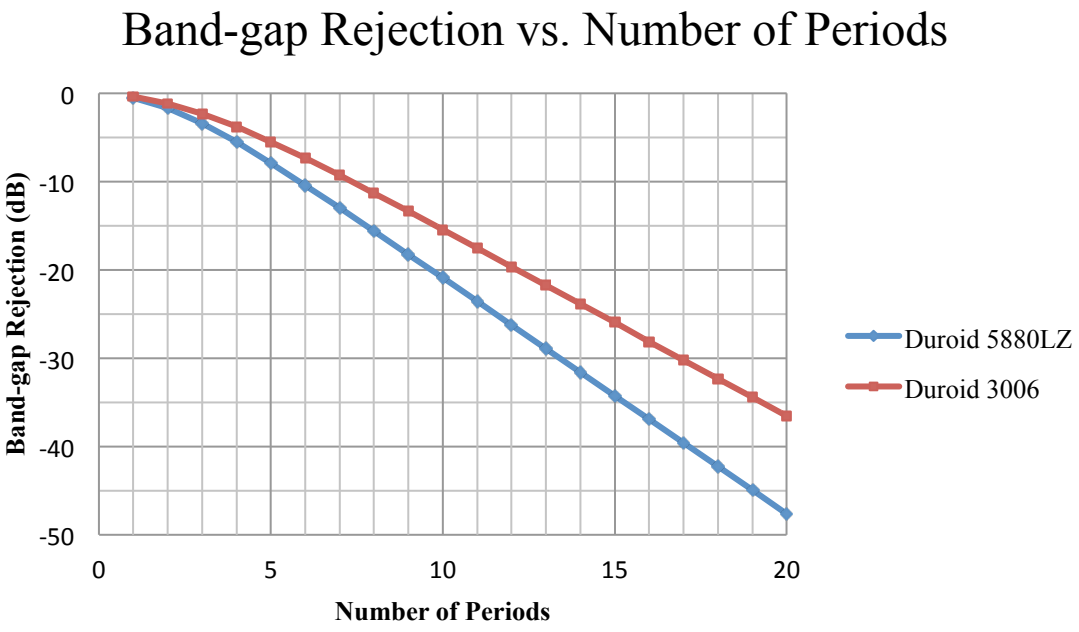

Figure 4.9: Effect of number of periods on band-gap rejection.

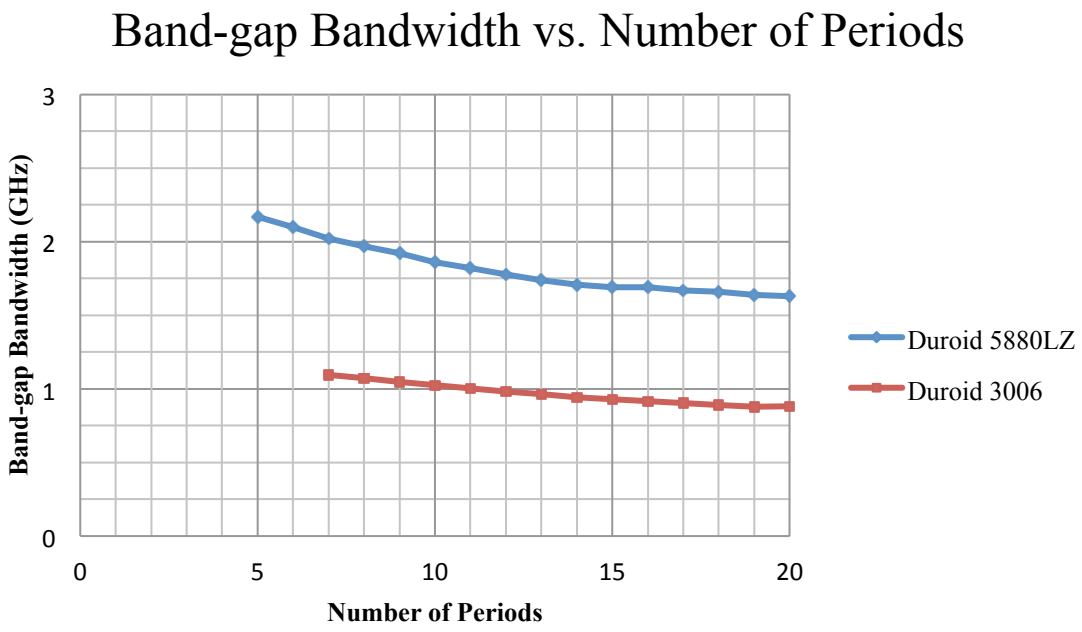

Figure 4.10: Effect of number of periods on band-gap bandwidth.

As expected, the number of periods does not influence the band-gap center frequency. It does, however, reduce the bandwidth of the band-gap when increased, as shown by Figure 4.10. One explanation for this behavior is because as propagating waves encounter more periodic cells, band-gap center frequency signals endure more rejection compared to non-band-gap frequency waves. This causes the band-gap to become narrower.

Simulation results shown in Figure 4.9 agree with the theory that increasing the number of periods in an EBG structure increases the band-gap rejection. After 5 periods, the relationship becomes linear. For the linear portion of the traces the attenuation per periodic cell can be determined. For Duroid® 5880LZ each period causes 2.67dB of attenuation for, and 2.11dB for Duroid® 3006. These values are a result of the dielectric contrast between overlay and non-overlay cells.

4.3 Effect of Substrate and Overlay Dielectric Constant

EBG theory states that a structure with greater dielectric contrast between periodic repeating elements will result in greater band-gap rejection. In the EBG microstrip structure developed this is achieved in two ways. The effective dielectric constant of a microstrip is a product of the relative dielectric constants of the base substrate and overlay. Adjusting either dielectric material will produce a change in effective dielectric constant.

It can be affirmed that a microstrip with a larger effective dielectric constant ε_{eff} will produce a smaller wavelength λ for a given frequency f through the following relation:

$$f = \frac{c}{\lambda\sqrt{\varepsilon_{eff}}},$$

$$\lambda = \frac{c}{f\sqrt{\varepsilon_{eff}}}.$$

This relation shows the band-gap wavelength of an EBG structure will decrease as ε_{eff} increases. It is therefore expected that Duroid® 3006 (ε_r=6.15) should produce a lower frequency band-gap than Duroid® 5880LZ (ε_r=1.96) for a given periodicity. This result should also be apparent for overlay dielectric constant.

To confirm these relationships, simulations were completed for both base substrates where the relative dielectric constant of the overlay was swept. Other parameters were kept constant: periodicity of 500mils, 10 periods, fill factor of 50%. The results are as follows:

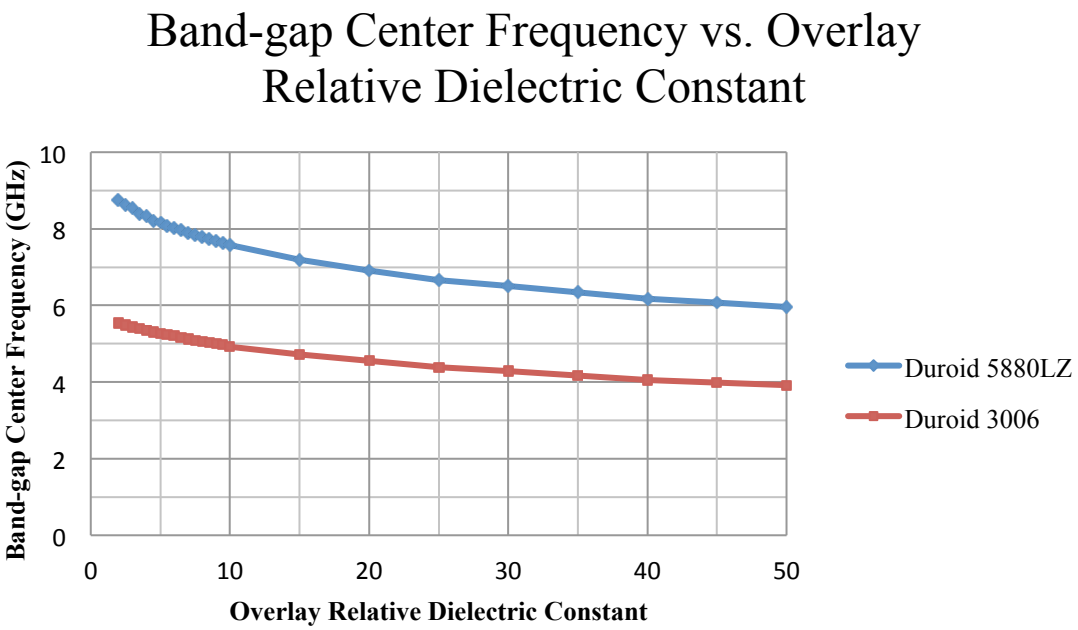

Figure 4.11: Effect of overlay relative dielectric constant on band-gap center frequency.

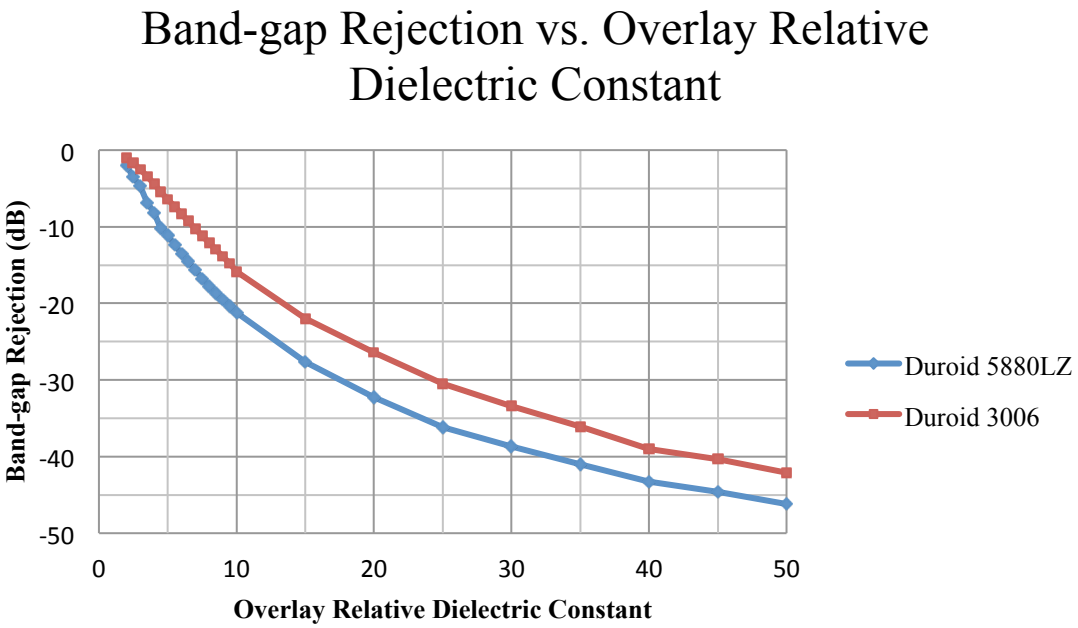

Figure 4.12: Effect of overlay relative dielectric constant on band-gap rejection.

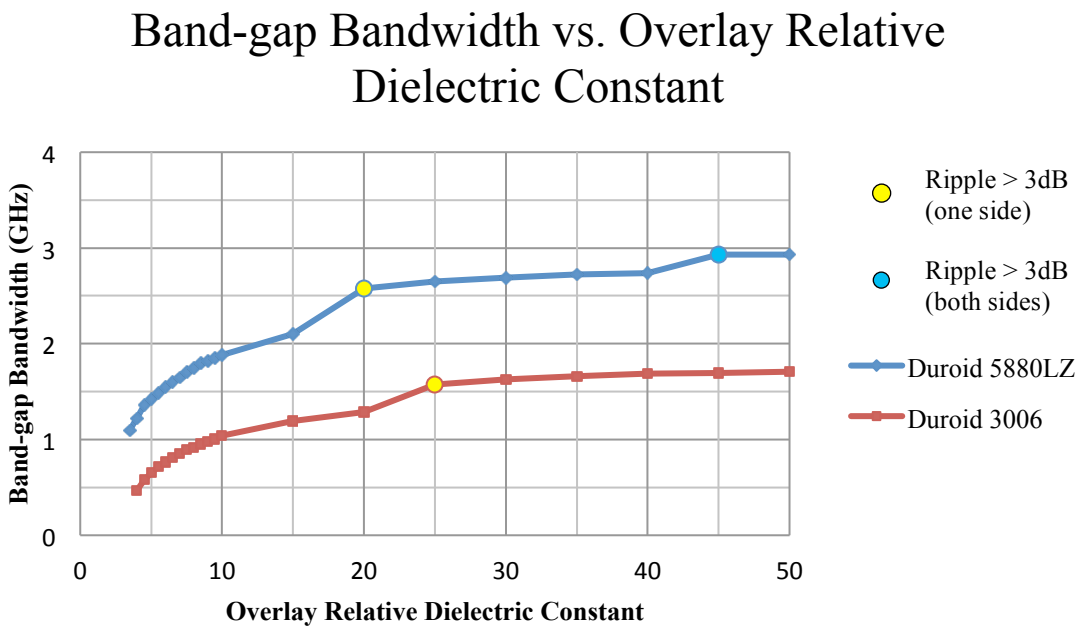

Figure 4.13: Effect of overlay relative dielectric constant on band-gap bandwidth.

As previously suggested, band-gap frequency decreases (Figure 4.11) and rejection increases (Figure 4.12) as the relative dielectric constant of the overlay increases. Duroid® 3006 (ε_r=6.15) does indeed always produce a lower frequency band-gap than Duroid® 5880LZ (ε_r=1.96) as per Figure 4.11. Also, Duroid® 5880LZ always produces a band-gap with more rejection (Figure 4.12) because, of the two base substrates, it has the larger dielectric contrast compared to the overlay dielectric.

Another result, shown in Figure 4.13, reveals that band-gap bandwidth increases as overlay relative dielectric increases. The graphs show sudden jumps in bandwidth. These points, as denoted in the legend, are due to >3dB ripple. Values which exceed 3dB attenuation must be considered part of the stop-band. Thus, when ripple first exceeds 3dB attenuation, there is a sudden increase in bandwidth.

4.4 Effect of Circular Overlay and Fill Factor

All previous simulations have kept fill factor constant at 50%. This means half of each periodic cell is microstrip line with overlay (fill factor is the ratio of overlay length to the total length of the periodic cell). However, in the actual design each overlay element is realized using a single piece of alumina (square or circular) rod; the fill factor will change as the periodicity varies. All simulations have also used square overlay opposed to circular which is one of the design implementations. The effects of fill factor and circular overlay elements on the EBG structure will be investigated.

4.4.1 Effects of Circular Overlay

To determine the effect of using circular overlay elements as opposed to square elements, the band-gap properties produced by each will be compared where all other conditions are identical. It is hypothesized that a circular overlay element may produce a band-gap with less rejection than a square overlay element of the same size (diameter). This is because the effective dielectric constant of the microstrip under the circular overlay is not constant. There is an air-gap between the circular overlay and the microstrip trace except for area where the overlay touches the microstrip. This air-gap reduces the effective dielectric constant.

Table 4. below shows the comparison of simulation results for various sized circular and square overlay elements. All simulations configurations have 50% fill factor and ten periods.

Table 4.2: Comparison of square and circular overlay element band-gaps.

	Overlay Size (Side/Diameter)	Band-gap Center Frequency (GHz)			Band-gap Rejection (dB)		
		Square	Circular	Delta	Square	Circular	Delta
Duroid® 5880LZ	1/8”	15.48	16.53	1.05	-18.217	-12.949	5.268
	¼”	7.53	8.28	0.75	-21.382	-13.424	7.958
	3/8”	4.98	5.58	0.60	-22.483	-12.792	9.691
Duroid® 3006	1/8”	9.98	10.68	0.70	-13.182	-6.937	6.245
	¼”	4.93	5.38	0.45	-14.364	-6.062	8.302
	3/8”	3.28	3.58	0.30	-14.78	-5.395	9.385

As hypothesized the band-gap rejection decreases for circular overlay elements. Large diameter circular overlay elements have a greater difference in band-gap rejection than smaller ones. Another finding is that circular overlay elements have an upward shifted band-gap center frequency. This behavior may be explained by the relationship found in Figure 4.11 where band-gap center frequency increases as the relative dielectric constant of the overlay decreases. As previously explained, the effective dielectric constant of the microstrip under the circular overlay is smaller than that of the square overlay because the air-gap between the trace and overlay decreases the relative dielectric constant of the overlay.

4.4.2 Effect of Fill Factor

To discover the effects of fill factor on an EBG microstrip structure, simulations shall be executed where fill factor is swept and all other factors remain constant. Identical tests will be completed for both base substrates. The constant test conditions are: Periodicity of 500mils, 10 Periods, alumina overlay ($\varepsilon_r = 9.8$). Simulation results are shown on the following two pages.

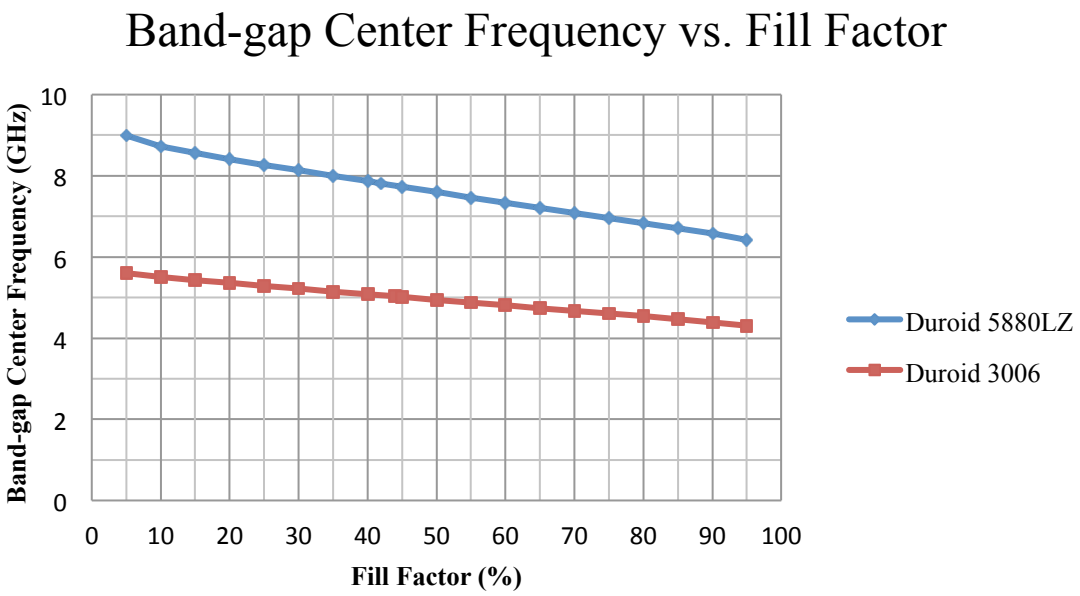

Figure 4.14: Effect of fill factor on band-gap center frequency.

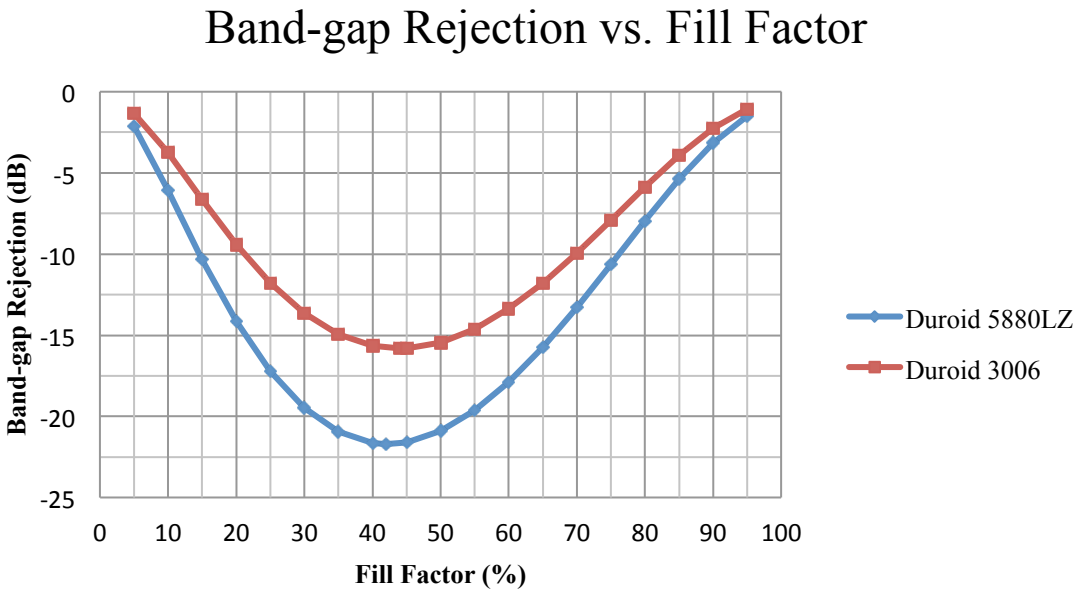

Figure 4.15: Effect of fill factor on band-gap rejection.

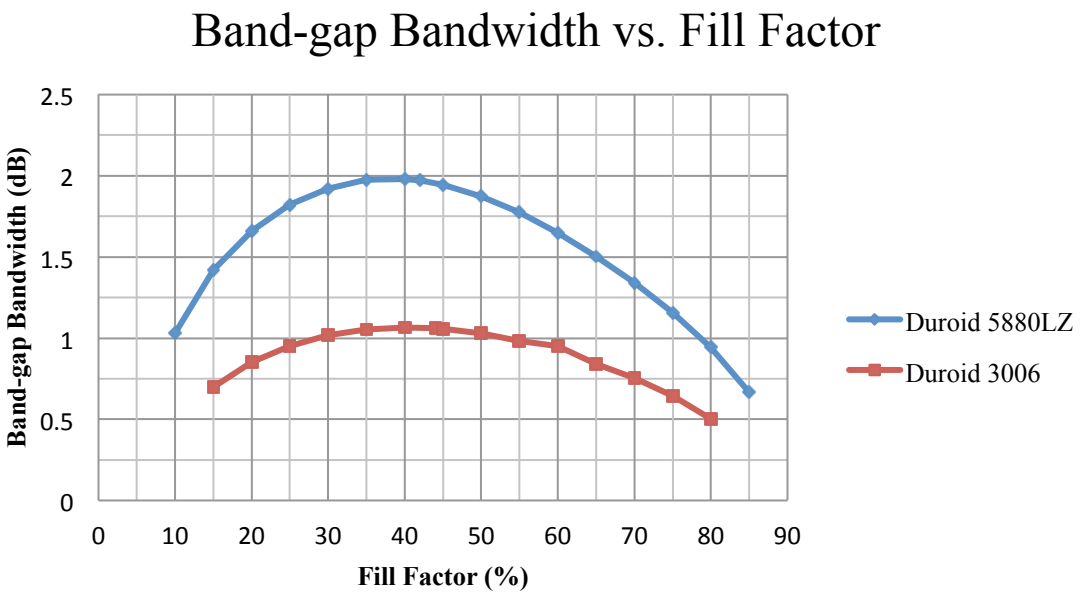

Figure 4.16: Effect of fill factor on band-gap bandwidth.

Simulation results reveal that band-gap center frequency decreases as fill factor increases (Figure 4.14). This behavior is due to the previously discussed inverse relationship between frequency and ε_{eff}. Increasing the fill factor increases the amount of microstrip with overlay (higher overall ε_{eff} along the microstrip), causing a downward shift in band-gap frequency.

Figure 4.15 shows that band-gap rejection is greatest at 42% fill factor for Duroid® 5880LZ and 44% fill factor for Duroid® 3006. Therefore, the fill factor at which band-gap rejection is maximized, decreases as the dielectric contrast of the periodically repeating dielectrics increases. Of the two substrates, Duroid® 5880LZ has larger dielectric contrast; hence maximum band-gap rejection occurs at a lower fill factor. Band-gap bandwidth is also maximized at the fill factor where rejection is maximized.

4.5 Higher Order Band-Gaps

All simulation results in the previous sections pertain to the fundamental band-gap. However, one of the unique qualities of EBG structures is its repeating band-gaps.

These higher order band-gaps experience the same effects that the fundamental band-gap experiences for all band-gap frequency and bandwidth relationships. The key difference is that the band-gap frequency is relative to the order of the band-gap (2^{nd} order band-gap frequency is double the fundamental band-gap frequency).

However, it was discovered in simulation that band-gap rejection is dependent on fill factor. Previously shown simulations reveal that for the fundamental band-gap, rejection maximizes near 50% fill factor, and minimizes at the fill factor extremes. This trend changes for higher order band. An overall trend is discovered that correlates the band-gap order to the fill factor when determining band-gap rejection.

The band-gap rejection of a second order band-gap maximizes at two fill factor values, opposed to one for the fundamental band-gap. A third order band-gap has three peaks, a fourth order has four, and so on. This relationship for higher order band-gaps has a repeating nature with a periodicity that may be evaluated in terms of fill factor. The periodicity of the relationship in terms of fill factor is equal to the reciprocal of the order n of the band-gap,

$$P_n = {}^{1}/_{n}\ (ff).$$

Therefore, the fundamental band-gap has a period of 1, second order is 0.5, third order is 0.333 etc. Shown below (Figure 4.17) are the ADS simulated results of the band-gap rejection vs. fill factor relationship for the first four orders of an EBG microstrip structure. Other relevant simulation parameters are: periodicity of 500 mils, 10 periods, alumina overlay, and Duroid® 5880LZ substrate.

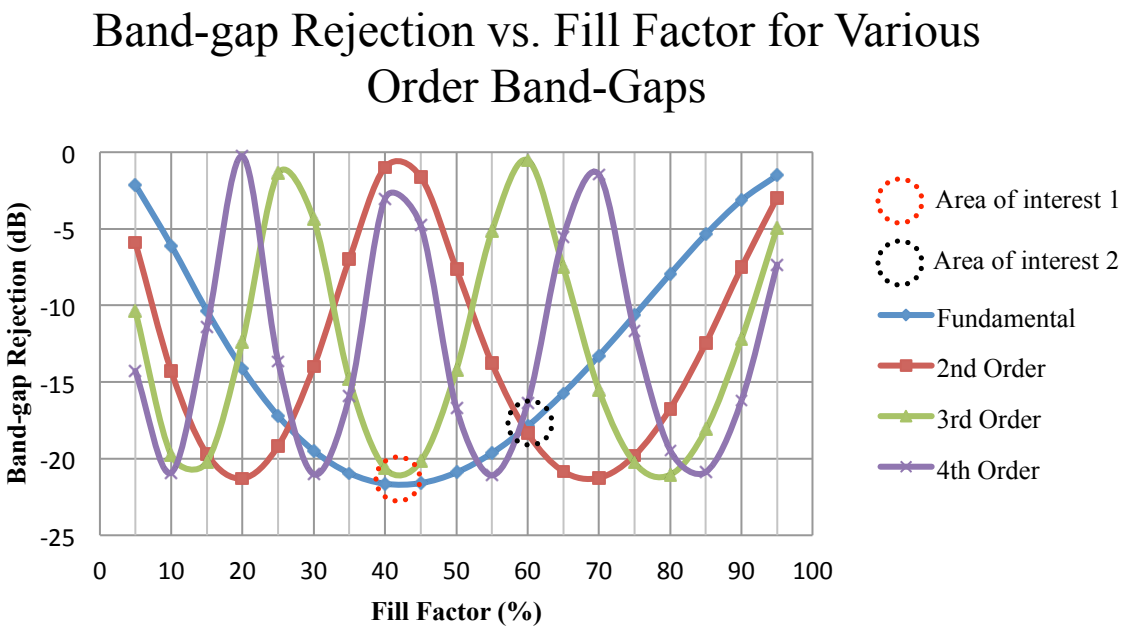

Figure 4.17: Effect of fill factor on band-gap rejection for four orders of band-gaps.

This trend holds for any periodicity. It was shown in Figure 4.6 that periodicity has very little effect on band-gap rejection. This applies to higher order band-gaps as well.

A noteworthy aspect of this relationship is that odd mode band-gaps share a common peak rejection fill factor value. This is denoted by 'Area of interest 1.' All even mode band-gaps are eliminated at this fill factor value as well. As a result, only odd mode band-gaps are present. This fill factor value is dependent on the substrate and overlay materials. For the simulation shown in Figure 4.17, this common peak rejection value occurs at 42% fill factor. A wide frequency S_{21} simulation when even mode band-gaps are eliminated is shown in Figure 4.18 where fill factor is 42%, and all other parameters are the same as those used to obtain results in Figure 4.17. Dielectric losses are omitting in this simulation.

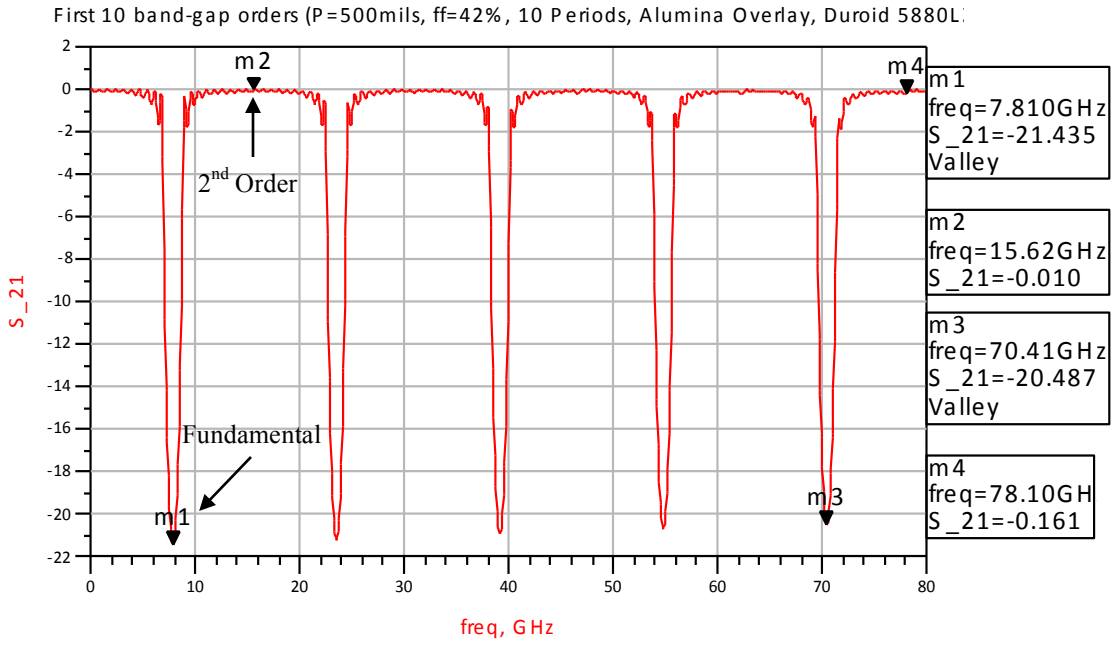

Figure 4.18: S_{21} even mode band-gap elimination for ff=42%.

Another filtering possibility achieved by controlling the fill factor is to eliminate every third order multiple band-gap (3^{rd}, 6^{th}, 9^{th}…). This is achieved for two fill factor values. One of these values, denoted by 'Area of interest 2', occurs when fill factor is 59.25%. Peak rejection is not achieved at this point like it is in area of interest 1, but all band-gaps have the same amount of rejection. The response at this fill factor is shown in Figure 4.19.

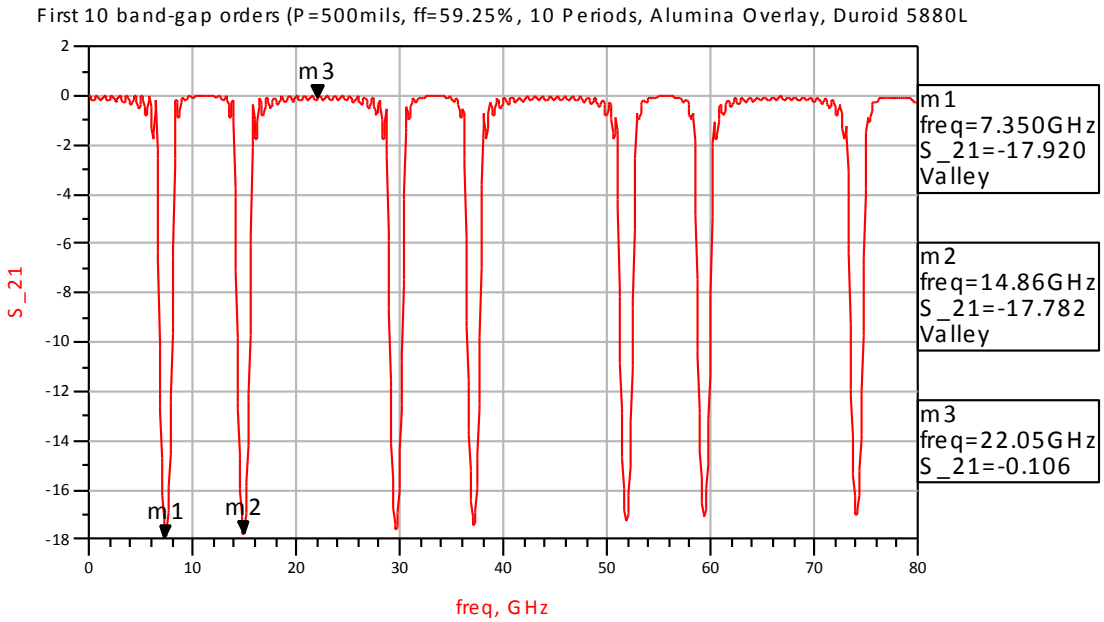

Figure 4.19: S_{21} 3rd order multiple band-gaps eliminated using ff=59.25%.

These developments of fill factor modulation introduce new filtering applications, not possible in a traditional filter topology. Implementing an EBG filter with the correct fill factor may allow suppression of only odd mode harmonics or suppression of non-third order multiple harmonics. It is, however, not possible to suppress all harmonics with the same level of attenuation.

4.6 Effect of Discontinuities

Ideally an EBG structure has perfect periodicity where every periodic cell in the structure is equal in length. Unfortunately in real world implementation this is not possible. To determine the effects of discontinuous periodic EBG microstrip structures, simulations shall be performed for discontinuities of varying severity. Discontinuities will be simulated by adding space between overlay elements. Figure 4.20 illustrates a discontinuity in overlay placement.

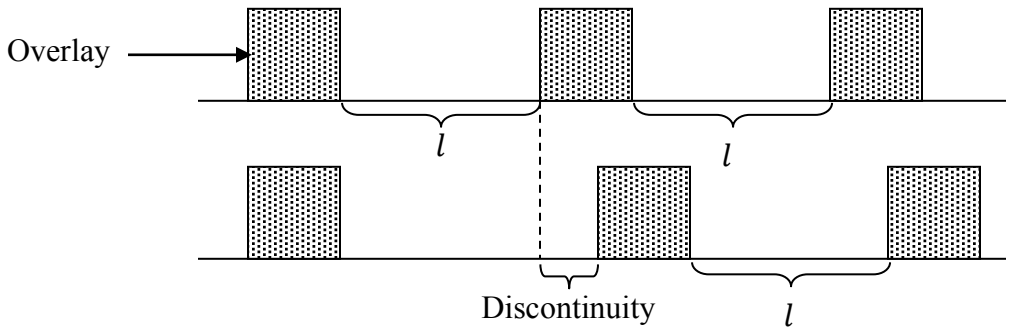

Figure 4.20: EBG structure with a discontinuity.

The following simulations were executed using a nominal period spacing of 1000 mils, 10 periods of ¼" square alumina overlay, and a Duroid® 5880LZ substrate.

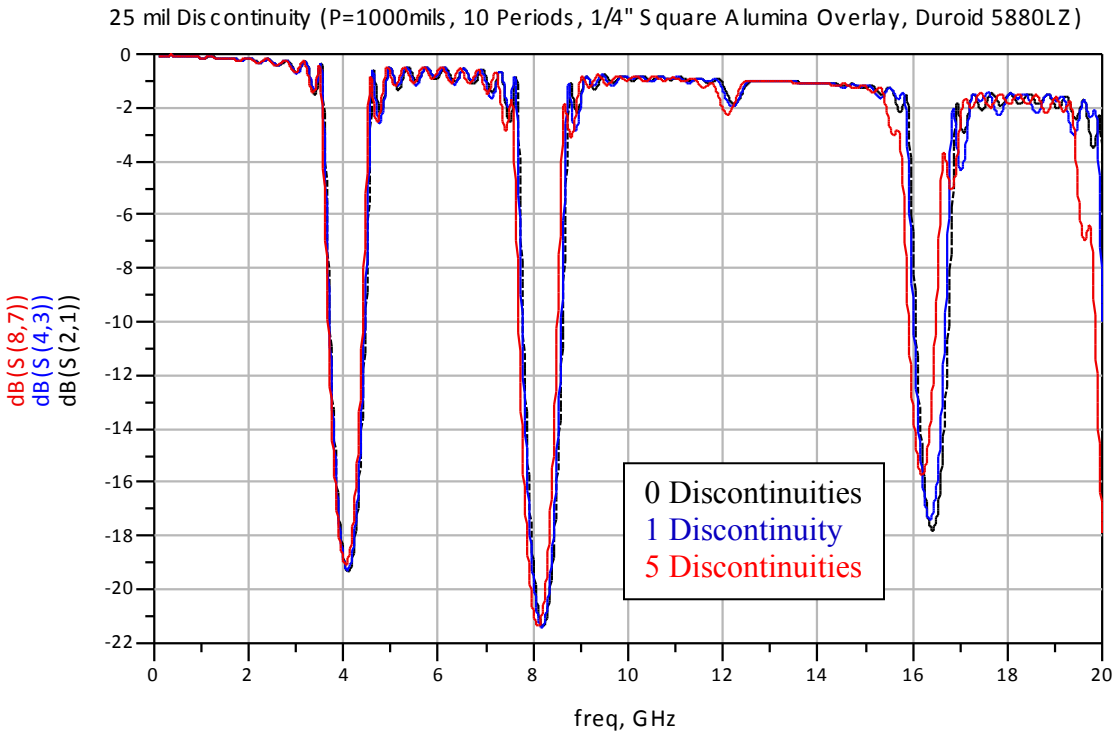

Figure 4.21: Effect of 25 mil discontinuities.

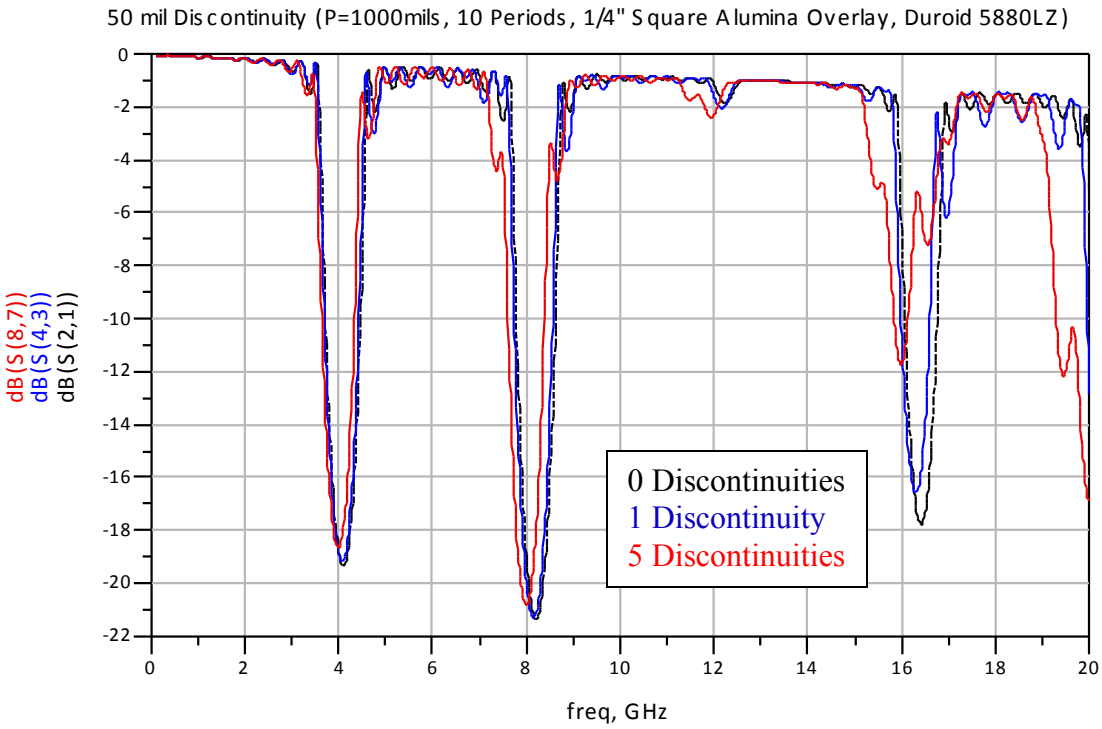

Figure 4.22: Effect of 50 mil discontinuities.

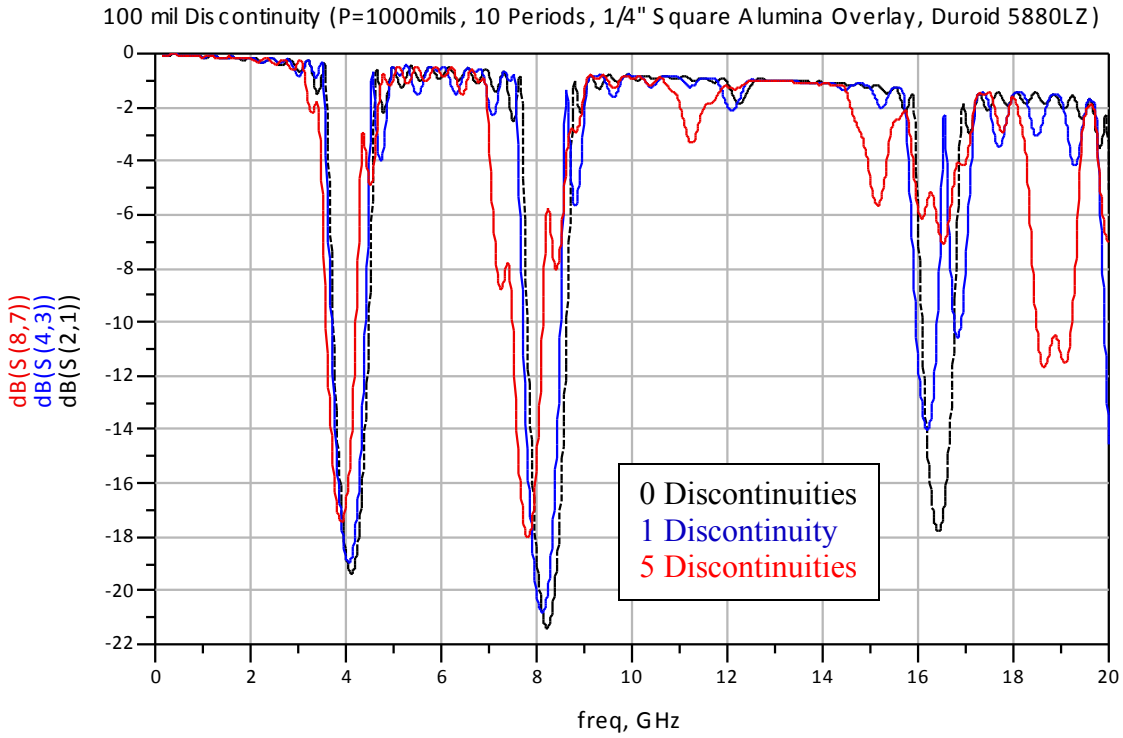

Figure 4.23: Effect of 100 mil discontinuities.

As seen in the figures above, discontinuities may have detrimental effects on band-gap response. When overlay is displaced it increases the period spacing of its periodic cell. This causes an additional, lower frequency, band-gap to form. The result is multiple band-gaps interfering to create a distorted response. More displaced overlay elements cause a deeper secondary band-gap to form which adds more distortion to the response. This is proven by the simulations above; a configuration with five displaced elements has a more distorted response than configurations with only one or no displaced elements. The amount of displacement required to cause distortion depends on the nominal period spacing of the EBG structure. For the simulations above (1000 mil period) distortion first becomes evident at 25mil displacement. The distortion would be more severe for a configuration with 500 mil period because 25 mils is larger relative to 500 mils than it is relative to 1000 mils. Higher order band-gaps are distorted more than lower frequency band-gaps because the separation between two interfering band-gaps is increased by the order of the band-gaps.

4.7 Summary of Results

ADS simulations have yielded much insight into the operation of an overlay controlled EBG microstrip filter. Key findings are highlighted below:

Effect of Periodicity: Periodicity has no effect on band-gap rejection, while an increased periodicity causes a decrease on both band-gap center frequency and bandwidth.

Effect of Number of Periods: The number of periods in an EBG structure has very little effect on band-gap center frequency. Increasing the number of periods linearly increases the band-gap rejection and narrows the band-gap bandwidth.

Effect of Overlay Dielectric Constant: A large dielectric constant overlay reduces the band-gap center frequency, increases band-gap rejection (higher dielectric contrast), and increases band-gap bandwidth.

Effect of Circular Overlay: Circular overlay, opposed to square overlay, causes a reduction in relative dielectric constant of the overlay because of the air-gap between the microstrip trace and the overlay itself. This causes the same effects as decreasing overlay dielectric constant.

Effect of Fill Factor: Fill factor is the ratio of the length of microstrip with overlay to the total length of a periodic cell. For the fundamental band-gap, the center frequency linearly decreases as fill factor increases. Band-gap rejection and bandwidth are maximized at a certain fill factor value specific to the dielectric contrast of the repeating dielectrics, and minimized at the fill factor extremes.

Higher Order Band-gaps: The rejection of the higher order band-gaps depends on the fill factor. This dependence is illustrated by Figure 4.17. If the correct fill factor is implemented, unique band-gap characteristics may be accomplished such as eliminating even mode band-gaps and eliminating third order multiple band-gaps.

Effect of Discontinuities: Perfect periodicity is not possible to implement in real-world application. Displaced overlay elements cause the formation of an additional band-gap with a different center frequency. These two band-gaps interfere with one another resulting in a distorted response. The amount of displacement necessary to cause distortion depends on the nominal periodicity of the EBG structure.

Chapter 5
FABRICATION

This chapter focuses on the construction of the devices and mechanisms described in the design section.

5.1 Microstrip Fabrication

Microstrip board fabrication consisted of milling the double sided copper clad substrate boards and soldering SMA connectors to the milled board. An LPFK Protomat S62 milling machine, shown in Figure 5.1 was used to mill the microstrip boards. The milling process was completed on October 9th, 2012 in the antenna laboratory (room 04-113) at Cal Poly, San Luis Obispo.

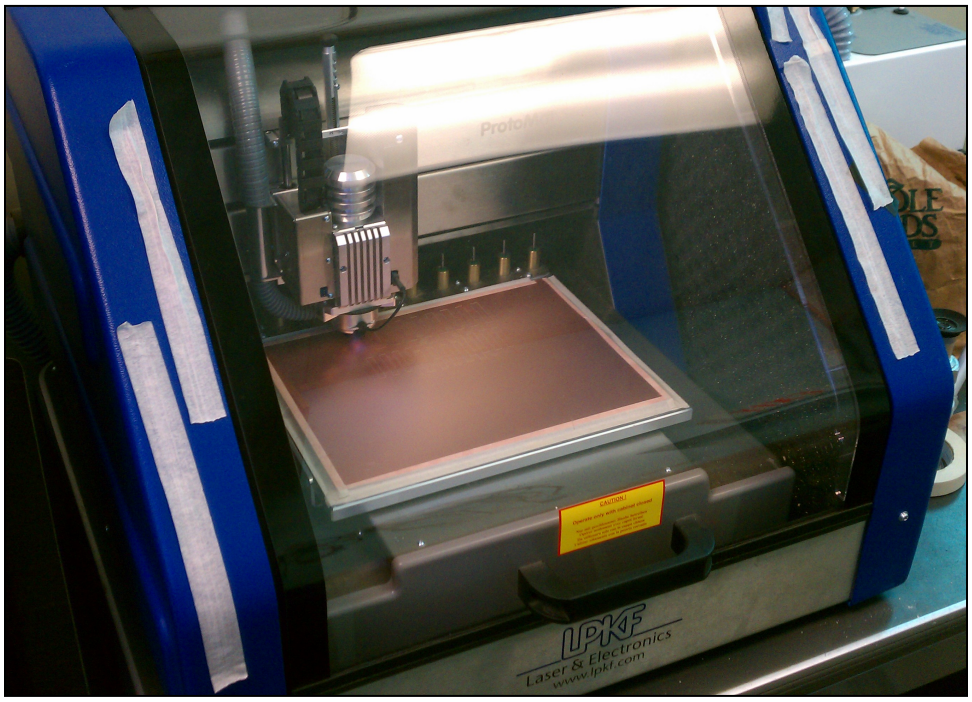

Figure 5.1: LPFK Protomat S62 milling machine used to mill microstrip boards.

Using the 12”x9” substrate samples, 11” long by 1.8” wide boards were constructed for each substrate board. This dimension yields ample length for a high tuning range and enough width to support the overlay rods. Gerber files containing board and trace dimensions were created using ADS. The Gerber files were converted into LMD files using ‘CircuitCAM’ by LPFK. The milling machine reads LMD files to determine cutting/milling areas and drill bit sizes.

Next, panel mount SMA connectors where soldered onto the milled boards. The completed microstrip boards are shown below in Figure 5.2.

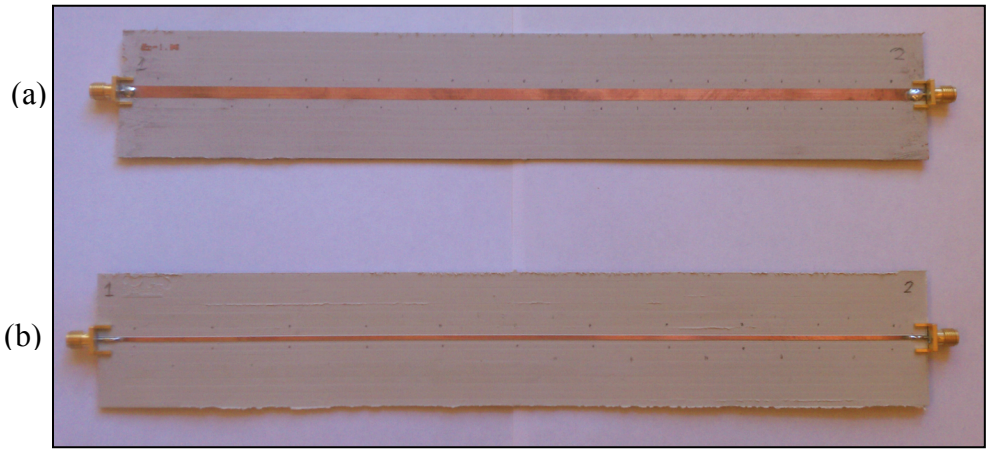

Figure 5.2: (a) Duroid® 5880LZ and (b) Duroid® 3006 microstrip boards.

5.2 Overlay Rods

To realize the several overlay elements, the 12” long alumina rods were cut into 1” sections. Alumina ceramic is almost as hard as diamond, making it very difficult to cut. A wet saw was used to cut the five rods into 1” length sections. Pictured below in Figure 5.3 and Figure 5.4 are the cut circular and square rods.

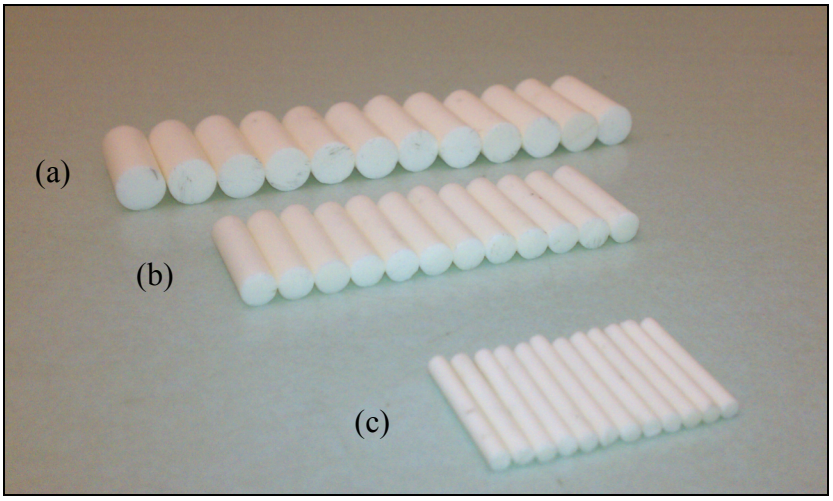

Figure 5.3: 1" long circular alumina rods. (a) 3/8" diameter, (b) 1/4" diameter, and (c) 1/8" diameter.

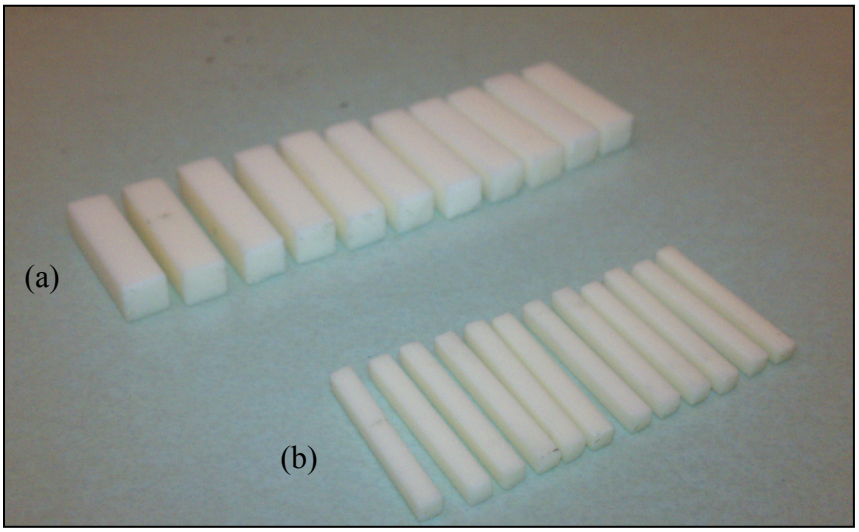

Figure 5.4: 1" long square alumina rods. (a) 1/4" sides and (b) 1/8" sides.

5.3 Acoustic Standing Wave Tuning Mechanism

The following parts where used to assemble the acoustic standing wave tuning mechanism:

(1) Clear Acrylic Tube

(a) Encloses the acoustic waves to form a standing wave

(b) 2” inner diameter with 1/8” thick walls

(c) Cut to a 15” length to allow spacing for connectors on the end of the 11” long microstrip board

(d) Manufactured by Tap Plastics

(2) Cardboard Mailing Tube

(a) Used to adjust the effective length of the acoustic tube

(b) 2” outer diameter to fit inside the acrylic tube

(3) End Cap

(a) Used to close the end of the tube

(b) 2” diameter to fit inside the tube

(4) Computer Speaker

(a) Altec Lansing ACS90

(b) 4.5W max output power

The test setup for using this mechanism will be discussed in more detail in a later chapter.

5.4 Mechanical Tuning Mechanism

The following parts were used to assemble the mechanical arm tuning mechanism:

(1) Wooden Sticks

(a) Used as the criss-crossing supports

(b) ¼” wide and 3/32” thick and cut into 2” long sections

(c) 20 sections (to support 10 overlay rods)

(2) Nails

(a) Used as a pivot point shaft

(b) Nail head used as an area to adhere overlay rods

To construct the mechanical arm, 1/16” diameter holes were drilled into each support piece where a nail may be inserted. Drilling holes in the exact same locations on each support is very important as any slight offset will affect the periodicity of the structure. Excess nail length was clipped. Since the periodicity in the structure exists in the middle joints, the alumina rods were glued to these points. Therefore each alumina rods should maintain equal separation as the device is extended/contracted. The finished device may be placed on top of the microstrip line with the overlay situated on the trace.

Chapter 6

CONTROLLED OVERLAY TESTING

Before testing either tuning mechanism, controlled overlay tests shall be performed to evaluate operation of the EBG microstrip structure. Placement of the overlay elements will be adjusted manually instead of using a tuning mechanism.

6.1 Test Setup

To evaluate relevant EBG filter parameters such as band-gap center frequency, band-gap rejection, and band-gap bandwidth, s-parameters must be measured. This requires a high frequency network analyzer. The HP 8720B is such a device, and was used for all s-parameter measurements throughout testing. The HP 8720B has a measureable frequency range of 130MHz-20GHz. S-parameter data was extracted using a LabView program on a computer connected to the HP 8720B via HPIB. Figure 6.1 is a picture of the test setup which includes the HP 8720B and SMA cables connected to the microstrip board.

Since a tuning mechanism is not used in this testing, the overlay is manually placed. EBG structures are very sensitive to small errors in period spacing so calipers were used to make the period spacing as accurate as possible.

Figure 6.1: HP 8720B network analyzer and microstrip board test setup.

6.2 Measurement vs. Simulation Comparison

S-parameters were measured for all combinations of the following parameters:

- Period Spacing: 500 mils, 1000 mils, and 1500 mils.
- Number of Periods: 10, 6, 4, and 2.
- 1/8" and ¼" square rods. 1/8", ¼", and 3/8" circular rods.
- Duroid® 5880LZ and Duroid® 3006.

In Figure 6.2 a picture is shown for an overlay configuration with ten ¼" square rods with 500 mil spacing on Duroid® 3006.

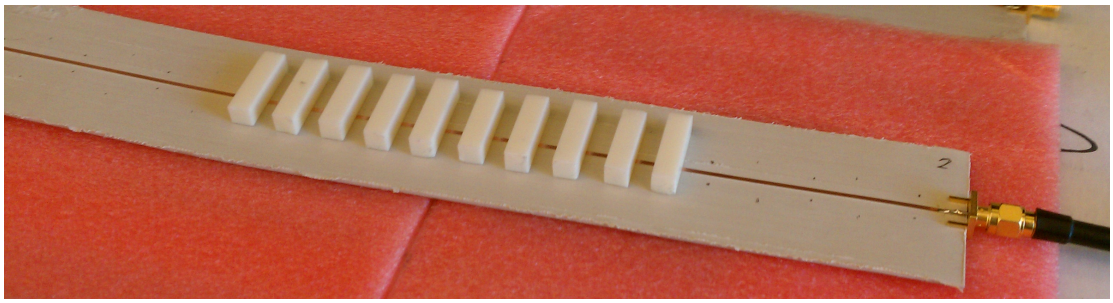

Figure 6.2: Picture of Duroid® 3006 microstrip board with ten ¼" square overlay elements spaced by 500 mils.

First the insertion loss and return loss of the microstrip board without overlay must be evaluated. Shown below in Figure 6.3 and Figure 6.4 are S_{11} and S_{21} responses of the Duroid® 5880LZ and Duroid® 3006 substrate microstrip boards without overlay.

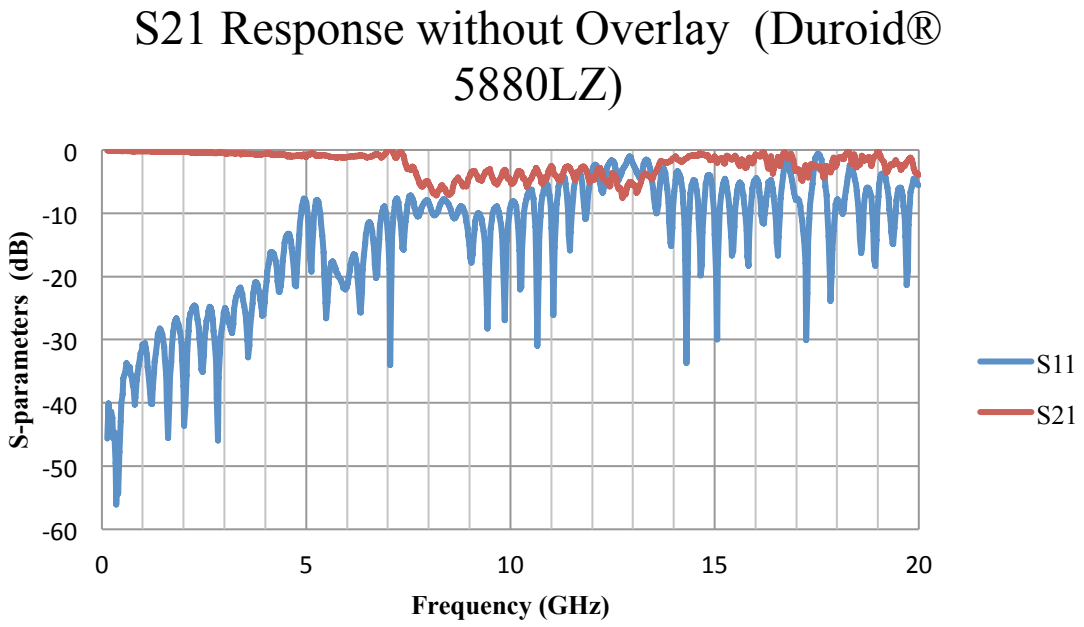

Figure 6.3: Insertion loss and return loss for Duroid® 5880LZ microstrip board without overlay.

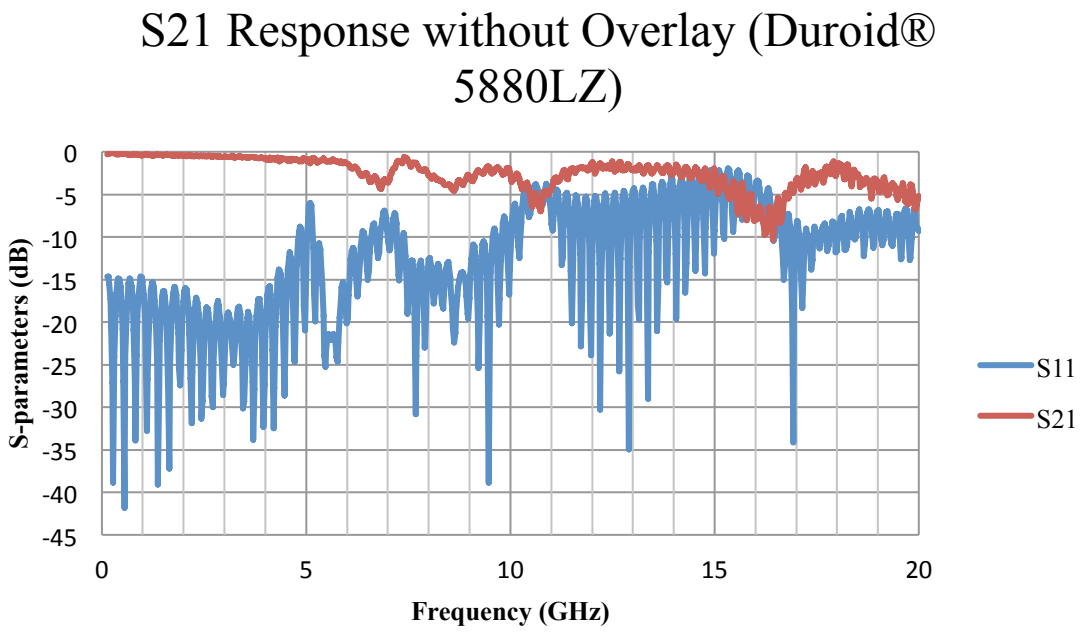

Figure 6.4: Insertion loss and return loss for Duroid® 3006 microstrip board without overlay.

Both substrate microstrip boards exhibit no more than 10dB insertion loss. The insertion loss of the boards without overlay <1dB below 5GHz but varies greatly above 5GHz. This preexisting insertion loss in the boards will limit the passband level of the EBG microstrip structure.

Shown in Figure 6.5 is an example of the measured S_{11} and S_{21} responses from the EBG microstrip structure. The first two band-gaps are clearly present. A reflection at the center of the third band-gap is present due to the fill factor of the configuration. Higher frequency band-gaps are more difficult to realize because small spacing inaccuracies have greater effects for smaller wavelengths. Also loss increases with frequency, making high frequency band-gaps not viable with the EBG microstrip structure.

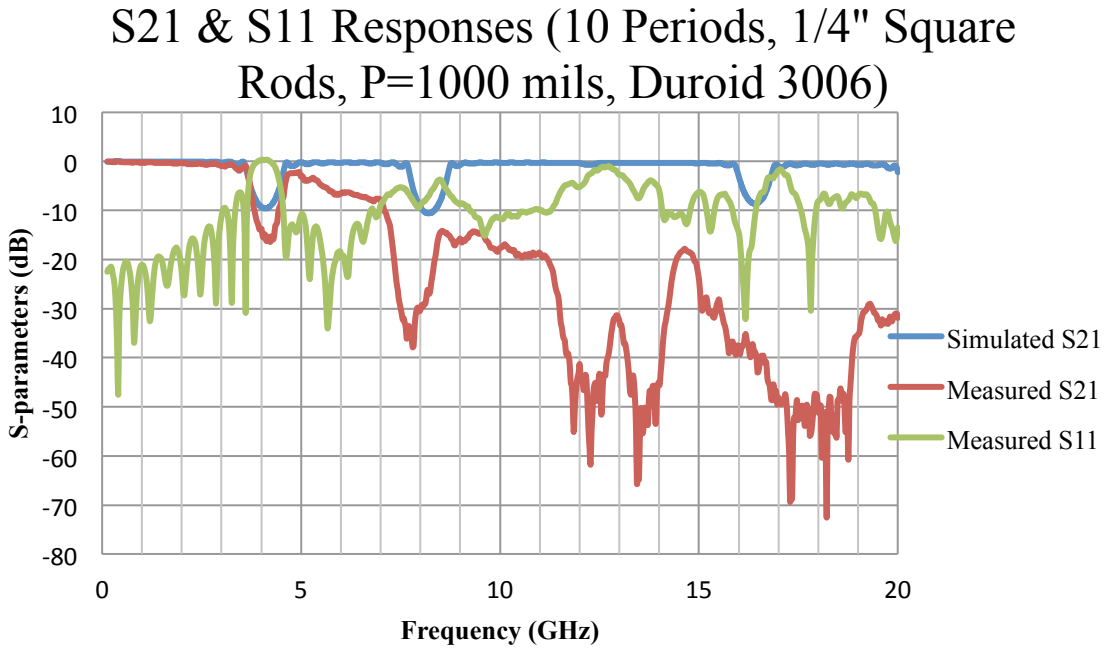

Figure 6.5: Comparison of simulated and measured S_{21} responses for Duroid® 5880LZ with ten ¼" square rods and 1000 mil spacing.

It is immediately apparent from Figure 6.5 that the measured S_{21} passband has much greater loss as compared to the simulated response. This has been discovered to be a disadvantage of the EBG microstrip topology. Passband attenuation increases as the number of periods increases. This trend is shown below in Figure 6.6 where the passband level decreases as number of periods increases. Also apparent is the increase in distortion for higher order band-gaps. This behavior, explained through simulation, occurs when there are discontinuities in overlay placement.

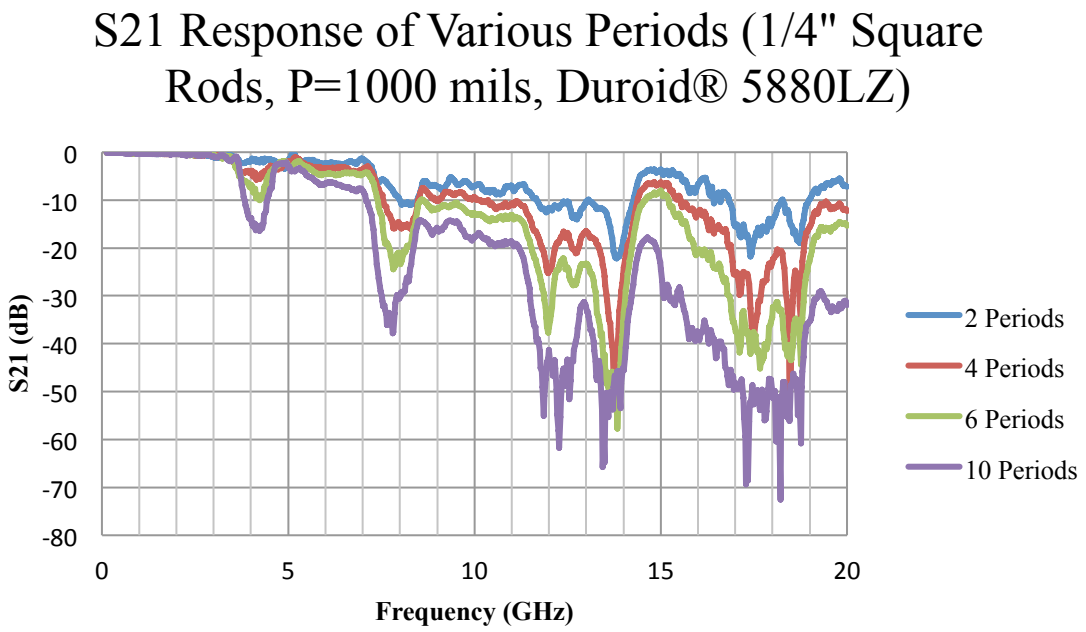

Figure 6.6: Effect of number of periods on passband loss.

The band-gap center frequency, rejection, and bandwidth of measured and simulated responses are compared in the following sections.

6.2.1 Band-gap Center Frequency Comparison

For band-gap center frequency comparisons, 10 periods were used for 500 mil and 1000 mil configurations, and 6 periods for 1500 mil configurations. The maximum number of periods is limited by the 11" length of the microstrip board. As shown in simulation, number of periods has little effect on band-gap center frequency. The following plots compare band-gap center frequencies of the measured and simulated responses.

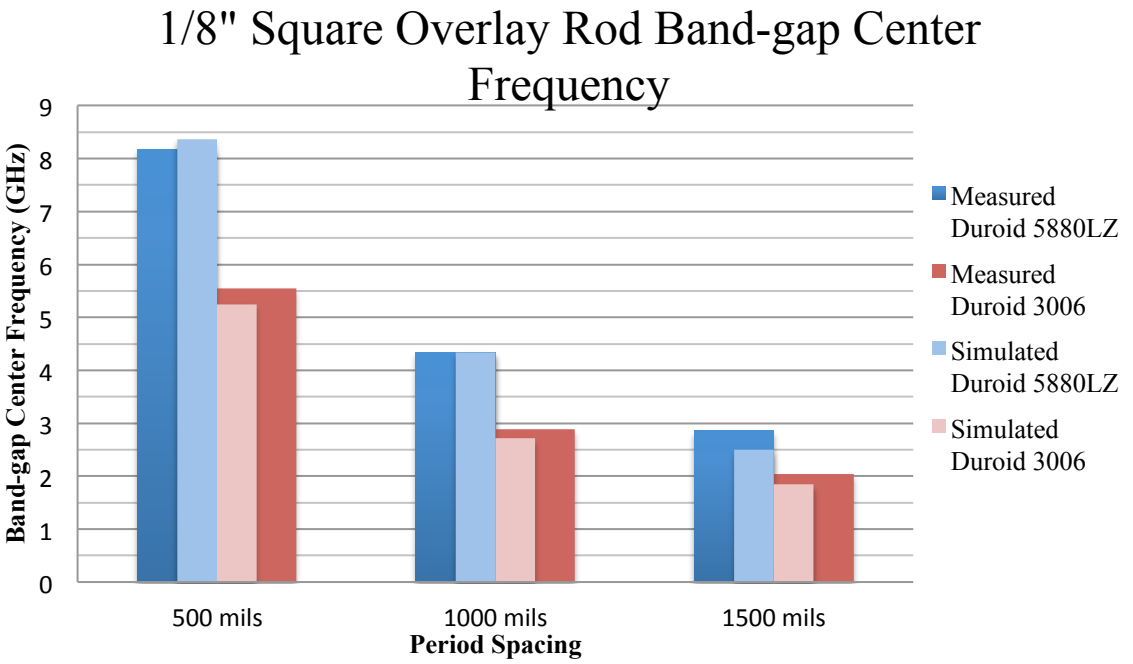

Figure 6.7: Comparison of measured and simulated S_{21} band-gap f_c for 1/8" square overlay.

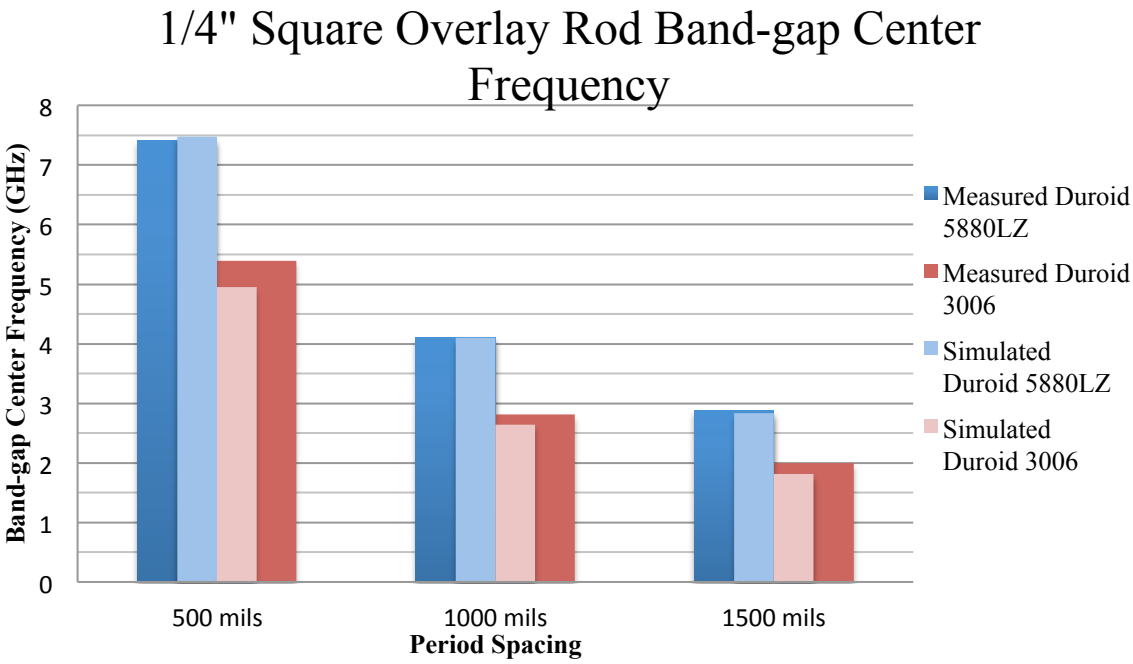

Figure 6.8: Comparison of measured and simulated S_{21} band-gap f_c for 1/4" square overlay.

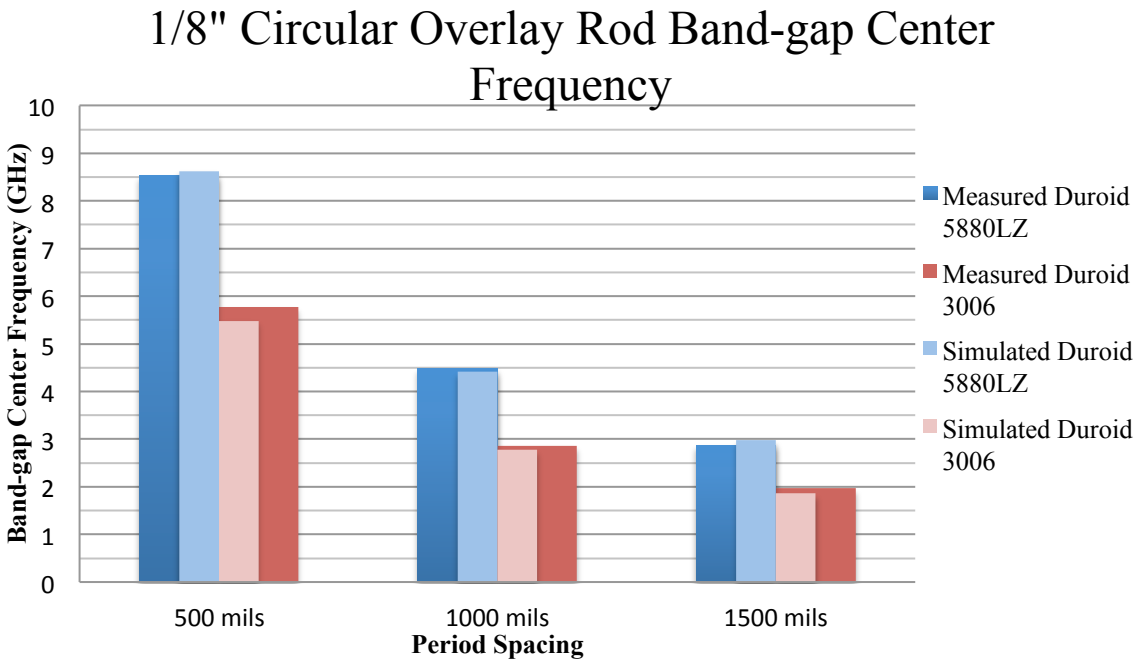

Figure 6.9: Comparison of measured and simulated S_{21} band-gap f_c for 1/8" circular overlay.

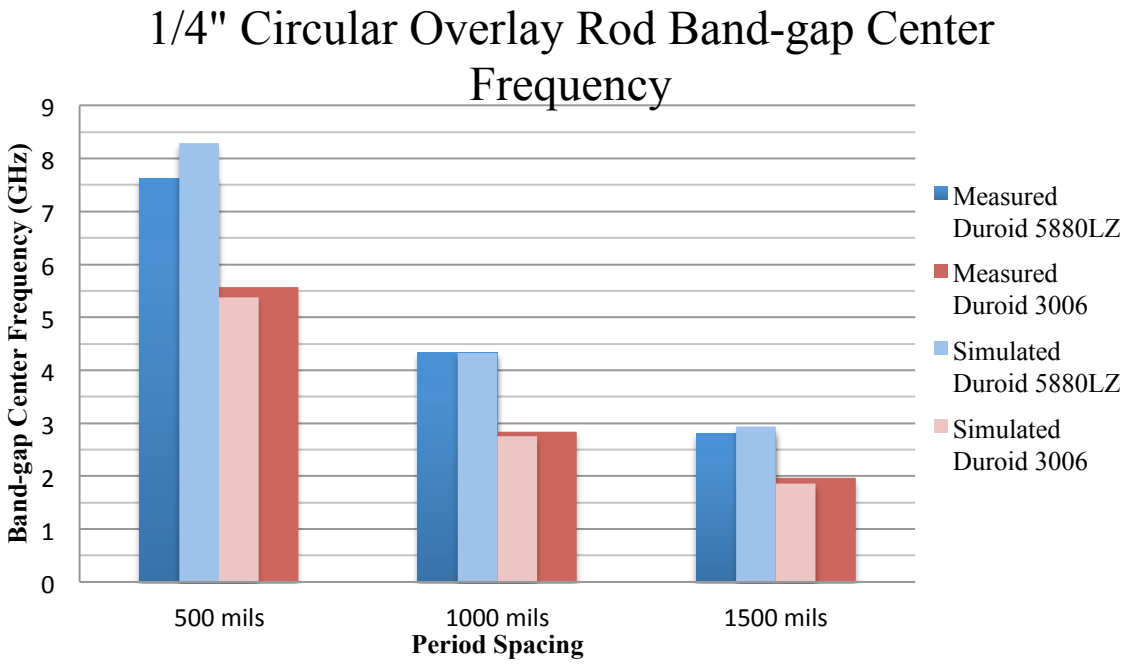

Figure 6.10: Comparison of measured and simulated S_{21} band-gap f_c for 1/4" circular overlay.

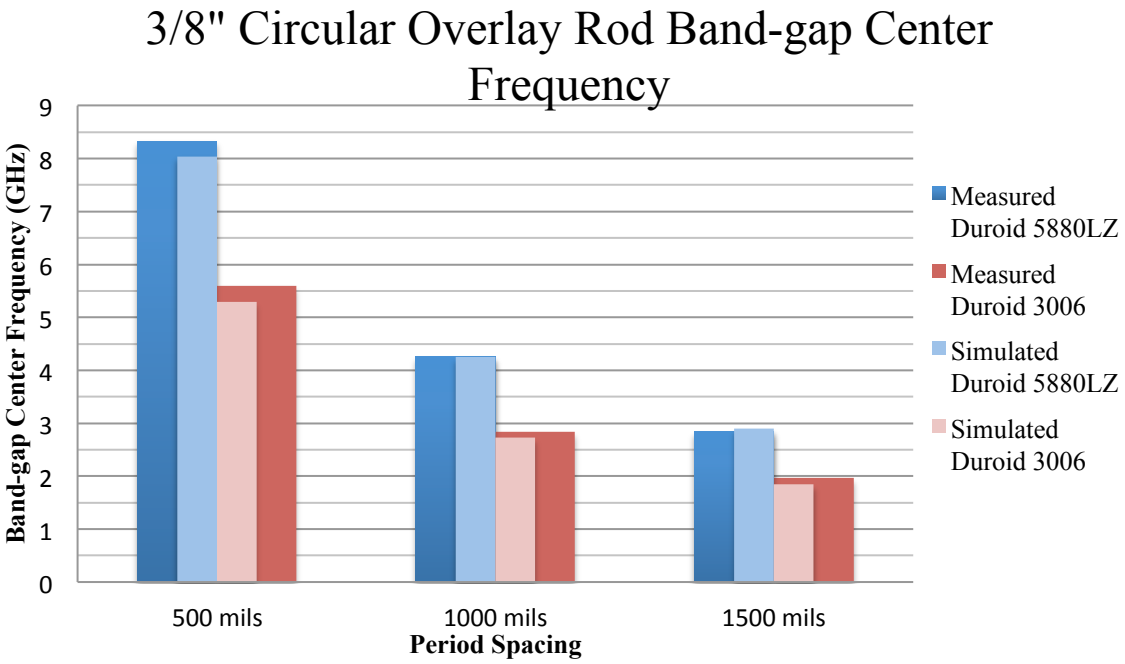

Figure 6.11: Comparison of measured and simulated S_{21} band-gap f_c for 3/8" circular overlay.

The band-gap center frequency error for the three period spacing values is tabulated below in Table 6.. Band-gap center frequency error is most likely due to inaccuracies in the placement of the overlay rods. This is unavoidable when manually placing overlay elements but is minimized by using a precise measurement device. Substrate and alumina overlay properties such as dielectric constant and loss tangent are assumed as nominal in simulation. Divergence from nominal dielectric constant will cause a change in band-gap center frequency. As shown in chapter 4, larger dielectric constant causes a downward shift in frequency. Largest band-gap frequency error occurs for 500 mil spacing configurations with an average error of 0.282 GHz. Average band-gap center frequency error throughout all test cases is 0.189 GHz or 4.44%.

Table 6.1: Band-gap center frequency error for 500, 1000, and 1500 mil period spacing values.

Period Spacing	Average Band-gap Center Frequency Error (GHz)	Average Band-gap Frequency Error (%)
500 mils	0.282	4.491
1000 mils	0.071	2.485
1500 mils	0.144	6.546

6.2.2 Band-gap Rejection Comparison

Simulation and measured band-gap rejection comparison plots for each size overlay and substrate are included in Appendix B. Table 6.2 shows the band-gap rejection error for each measured case. Error for the three period spacing values and two substrates are combined.

Table 6.2: Band-gap rejection error for each size overlay element.

Overlay	Number of Periods	Average Band-gap Rejection Error (dB)	Average Absolute Band-gap Rejection Error (dB)
1/8" Square	10	3.509	3.509
	6	1.400	1.400
	4	0.589	0.634
	2	0.138	0.359
1/4" Square	10	1.062	6.668
	6	0.966	2.321
	4	0.672	0.905
	2	0.092	0.763
1/8" Circular	10	-0.337	0.853
	6	-0.290	0.543
	4	-0.388	0.416
	2	-0.301	0.301
1/4" Circular	10	-0.625	2.352
	6	-0.773	1.212
	4	-1.088	1.350
	2	-0.681	0.848
3/8" Circular	10	1.356	2.271
	6	-0.883	1.534
	4	-0.779	1.111
	2	-0.711	0.834

As shown by the results, error tends to be largest for configurations with more periods. This is because, as previously proven, band-gap rejection increases for more periods; therefore the error due to a difference in band-gap rejection for a single periodic cell will accumulate as the number of periods increases. Maximum average error occurs for ¼" square rod overlay configurations. These configurations yield the greatest overall band-gap rejection with -34.17dB and -10.46dB attenuation for Duroid® 5880LZ and Duroid® 3006 respectively; it therefore comes with no surprise that this configuration has the largest average error. Average absolute band-gap rejection error for all test cases is 1.358 dB.

Perhaps the greatest source of error is the much larger than anticipated loss. Loss due to substrate and overlay dielectric was much less in simulation than in measurement. For example in Figure 6.5 at 10GHz the measured passband is ~18dB lower than simulated and ~30dB less at 20GHz.

As apparent from the plots in Appendix B, measured rejection for circular rods was greater than simulation predicted for Duroid® 5880LZ configurations and less than simulation predicted for Duroid® 3006 configurations. These discrepancies must be due to the difference in actual dielectric constant of the substrate from nominal used in simulation.

6.2.3 Band-gap Bandwidth Comparison

Not every band-gap produced has a measureable bandwidth; some band-gaps do not reach -3dB attenuation relative to the passband. Band-gaps with measureable bandwidths are tabulated below in Table 6.3 along with their respective simulation and error values. As expected (Figure 4.7) bandwidth decreases as periodicity increases. The direct relationship between the number of periods and bandwidth is also confirmed; bandwidth tends to decrease for fewer periods. The average absolute bandwidth error, as compared to simulation, for all measured cases is 0.325GHz. There are a few anomalous measurements where the bandwidth error is >1GHz.

Table 6.3: Band-gap bandwidth error.

Substrate	Overlay	Period Spacing (mils)	Number of Periods	Measured Bandwidth (GHz)	Simulated Bandwidth (GHz)	Bandwidth Error (GHz)
Duroid® 5880LZ	1/8" Square	500	10	1.622	1.62	0.002
			6	1.447	1.71	-0.263
		1000	10	0.65	0.51	0.14
	¼" Square	500	10	1.54	1.92	-0.38
			6	1.03	2.16	-1.13
		1000	10	0.91	0.95	-0.04
			6	0.86	1.05	-0.19
	1/8" Circular	500	10	0.89	1.11	-0.22
	¼" Circular	500	10	1.58	1.59	-0.01
			6	1.24	1.65	-0.41
		1000	10	0.57	0.54	0.03
	3/8" Circular	500	10	0.66	1.66	-1.00
			6	0.47	1.78	-1.31
		1000	10	0.64	0.68	-0.04
			6	0.67	0.59	0.08
Duroid® 3006	1/8" Square	500	10	0.69	0.97	-0.28
	¼" Square	500	10	0.80	0.96	-0.16
			6	0.80	-0.98	-0.18

6.2.4 Fill Factor Effect Comparison

As stated in section 4.6, band-gap rejection is highly dependent on the fill factor of the periodic cells. To prove the relationship previously established (shown in Figure 4.17) a test shall be executed where fill factor is swept. With only 12 elements of each overlay size available, a configuration with 4 periods separated by 1000 mils is used. The fill factor can be incremented by adding 1/8" and ¼" square rods. Each 1/8" section results in a 12.5% increment in fill factor. This test was executed on a Duroid® 5880LZ board and the results as compared to simulation are as follows in Figure 6.12.

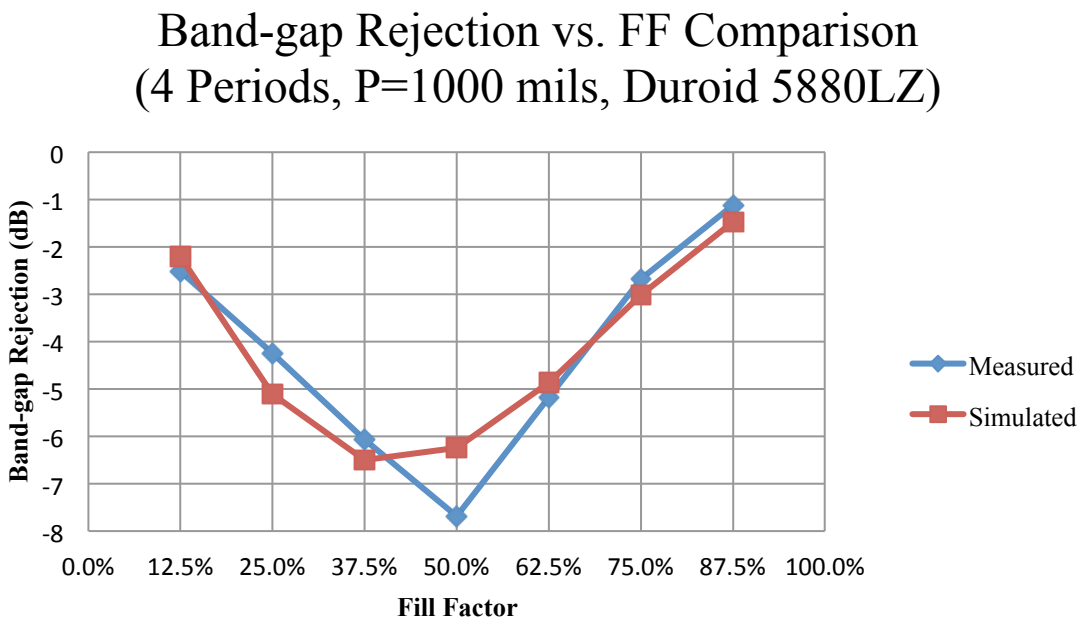

Figure 6.12: Comparison of the effect of fill factor on Band-gap rejection.

The effect of fill factor on band-gap rejection is verified through experimentation. Although maximum rejection occurs at 50% in measurement instead of 37.5% like in simulation, the expected trend is evident. Band-gap rejection is maximized around 50% fill factor and minimized at the fill factor extremes. The fill factor at which band-gap rejection is maximized at is dependent on the dielectric contrast of the periodically repeating EBG dielectrics.

6.3 Summary of Results

In this chapter, band-gap center frequency, rejection, and bandwidth of various configurations were measured and compared to simulation. Comparing these band-gap properties allows the relationships found in simulation to be confirmed.

Band-gap center frequency: Average band-gap center frequency error ranged from 0.071 GHz (1000 mil configurations) to 0.282 GHz (500 mil configurations). As

spacing decreases, band-gap center frequency increases; therefore, overlay displacements have a greater effect in frequency offset.

Band-gap rejection: Average band-gap rejection error increases for configurations with more periods. This is because each periodic cell contributes a certain amount of rejection, and if it is different from simulation, then the error accumulates as more periods are added. Maximum error occurred for configurations with ten ¼" square rods, with an average error of 6.668 dB. ¼" square overlay rod configurations also had the largest average rejection, while configurations with 1/8" circular overlay rods had the smallest average rejection.

Band-gap bandwidth: Average band-gap bandwidth error across all configurations with a measureable bandwidth was 0.325 GHz. While the error is large, the expected relationships regarding bandwidth were confirmed. Bandwidth increases as periodicity decreases (higher center frequency), and bandwidth increases for more periods.

Fill Factor: In simulation fill factor was found to directly control the rejection of every order band-gap. To confirm this behavior, the rejection of the fundamental band-gap was measured as fill factor was swept. Results matched simulation which suggested rejection is maximized at a certain fill factor near 50% and minimized at the fill factor extremes.

Post-test design considerations: Several design considerations not previously known can be taken away from these tests. It was established through EBG structure theory and simulation that band-gap rejection may be increased by increasing the number of periods with little side effects. However, this also increases loss which reduces the pass band level more as frequency increases. If using this design, one would need to

balance between passband level and band-gap rejection. Loss may be reduced by using a higher dielectric constant substrate (to reduce dielectric contrast). This however introduces another trade-off because lowering dielectric contrast reduces band-gap rejection. This is apparent throughout Duroid® 3006 substrate tests which have less loss but also less band-gap rejection. Like most designs in electrical engineering, trade-offs must be made to achieve optimum performance.

Chapter 7

TUNING MECHANISM TESTING

In this chapter the performance of the acoustic standing wave tube and mechanical arm tuning mechanisms are evaluated.

7.1 Acoustic Standing Wave Tuning Mechanism Testing

7.1.1 Test Setup

To ensure the formation of a standing wave in the tube, the pressure distribution throughout the length of the tube must be measured. This is accomplished by using a microphone. To measure the pressure levels at various locations inside of the tube, a microphone was connected to a long piece of rigid coax where the other end sticks out of the end cap to be slid in and out of the tube. An electret condenser microphone with a build in FET was used. The schematic in Figure 7.1 shows the bias and output circuitry along with the equipment used.

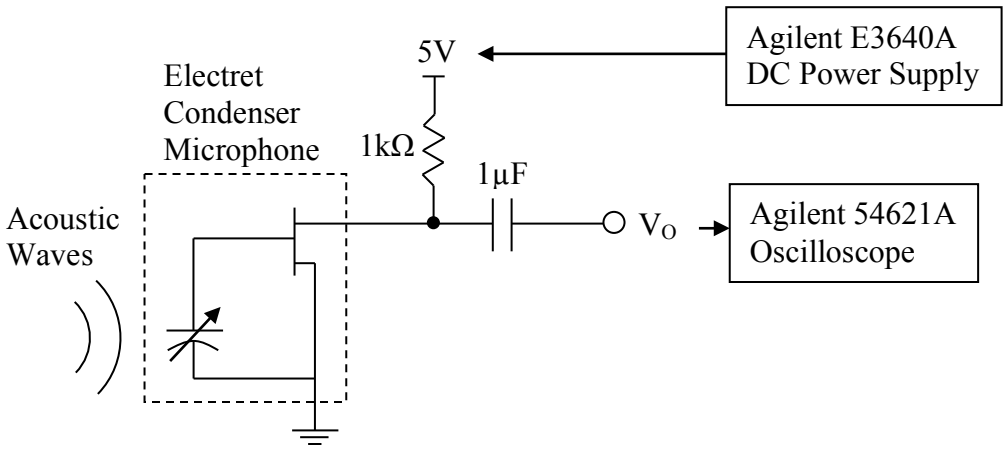

Figure 7.1: Schematic of microphone circuitry and test equipment.

The test setup includes the tube with an end sealed by an end cap, and the other end positioned up to the speaker. Pictures of the test setup with the microphone circuitry, tube, speaker, and test equipment are shown in Figure 7.2 and Figure 7.3.

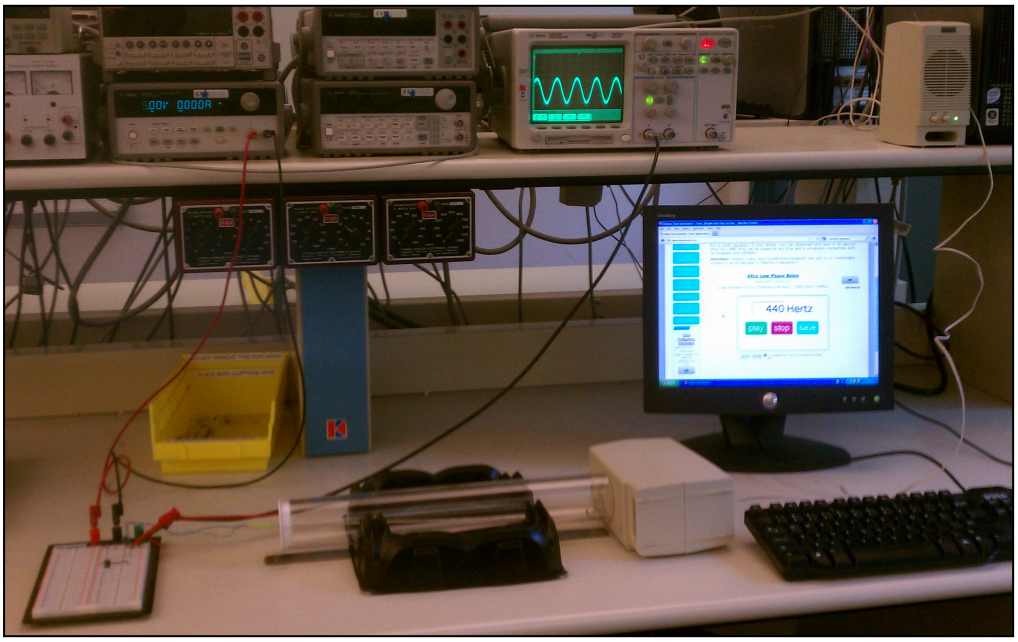

Figure 7.2: Acoustic standing wave tube mechanism test setup.

Figure 7.3: Closer view of tube, microphone, coax, end cap, and speaker.

7.1.2 Producing a Standing Wave

Since the speaker is placed at the open end of the tube, an open-closed standing wave (as shown in Figure 3.9) forms. The effective length $L_{effective}$ of an open-closed standing wave tube is actually slighter longer than the length of the tube L_{actual}. The reflection point on the open end of the tube is slightly beyond the open end. The effective length of an open-closed tube may be expressed by [20]:

$$L_{effective} = L_{real} + 0.3D,$$

where:

D = tube diameter.

The effective length of the open-closed standing wave tube used is calculated as:

$$L_{effective} = 38cm + 0.3(5.08cm) = 39.52cm.$$

Now the wavelengths and frequencies of the various ordered modes for this tube may be calculated using the equations stated in section *3.4.1*. To verify these calculated values, the microphone was used to measure the frequency at which maximum pressure distribution occurs for the anti-nodes; this is a standing wave condition. The third mode was measured since it is the lowest mode with an anti-node inside of the tube. A standing wave of the third mode formed at 606Hz. This yields a measured effective tube length of 42.1cm. This extra length is due the small distance in which the actual speaker device rests beyond the inside of the casing. Also, the calculations assume a speed of sound of 340m/s which may be slightly inaccurate depending on room temperature. The calculated and measured wavelengths and frequencies for various mode standing waves are shown in Table 7..

Table 7.1: Calculated and measured wavelengths and frequencies for various modes of the standing wave tube.

Mode	λ_{calc}	f_{calc}	λ_{meas}	f_{meas}
1	1.5808m	215.1Hz	1.683m	202Hz
3	0.5269m	645.2Hz	0.5611m	606Hz
5	0.3162m	1075Hz	0.3366m	1010Hz
7	0.2258m	1506Hz	0.2405m	1414Hz
9	0.1756m	1.936kHz	0.1870m	1818Hz
11	0.1437m	2.366kHz	0.1530m	2222Hz

The peak pressure levels over the length of the tube for modes 1-11 were measured. The speaker volume was set to 10% max output; pressure too large causes distortion in microphone output. The peak to peak voltage of the microphone output was recorded at incremented positions within the tube. This voltage may be converted to pressure, given the sensitivity of the microphone. The microphone sensitivity (V_{rms}/P_{rms}) for the setup used is $-65dB \pm 4dB$, where $0dB = 1V/0.1Pa$ [21]. This sensitivity may alternatively be expressed as $6.31mV_{rms}/P_{rms}$ (pressure is in Pascals). The pressure waveforms for modes 1-11 are included in Appendix A.

An important result which may be drawn from the pressure measurements is that pressure level decreases for higher mode standing waves (higher acoustic frequency). This result is important because to control many overlay rods, a high order standing wave is required. For example, controlling 10 overlay rods (10 nodes) requires a 21st order standing wave. Following the trend plotted from the data recorded in Appendix A (Figure 7.4), a 21st order standing wave will have extremely small pressure levels. The pressure levels required to move the overlay rods must be determined.

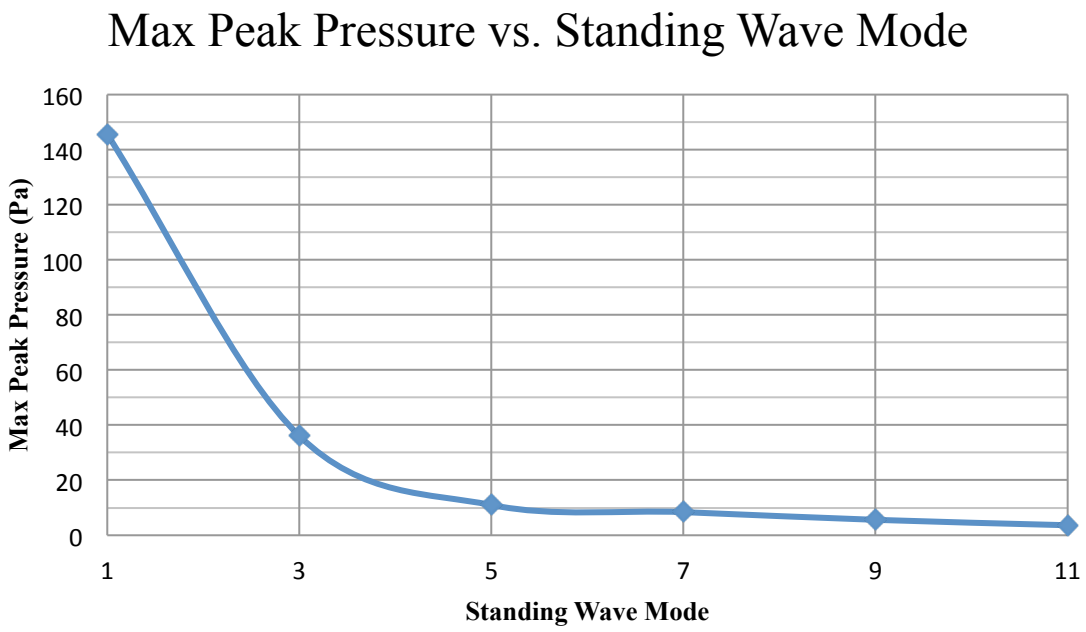

Figure 7.4: Maximum pressure at anti-nodes decrease as higher order standing waves are formed.

7.1.3 Overlay Adjustment Using an Acoustic Standing Wave

Before attempting to move alumina rods along the microstrip board with a pressure standing wave, moving a lighter material will be attempted first. A common material used to demonstrate a pressure standing wave is small pieces of Styrofoam. Small pieces of Styrofoam were acquired used to lightly fill the base of the tube. By adjusting the acoustic pressure and observing the pieces of Styrofoam, the pressure required to move the Styrofoam may be determined. The table below (Table 7.2) represents the peak pressure levels required in the standing wave tube to visibly move the Styrofoam pieces. A 'standing wave formation' means Styrofoam pieces have moved away from the anti-nodes and gathered at the nodes. Distortion to the microphone output occurred when measuring pressures beyond ~ 70 Pa; these pressure levels are obtained by linearly extrapolating from the pressures recorded at 10% speaker volume.

Table 7.2: Standing wave pressure (and speaker volume) required to move Styrofoam pieces.

Mode	Visible Movement	Moved into Standing Wave Formation
Mode 1 (202 Hz)	46.2 Pa (7.3% Vol.)	253.3 Pa (40% Vol.)
Mode 3 (606 Hz)	70.4 Pa (20% Vol.)	334.3 Pa (95% Vol.)
Mode 5 (1010 Hz)	101.4 Pa (100% Vol.)	--

Substantial movement of the Styrofoam can be accomplished for only modes 1 and 3. The Styrofoam cannot be moved beyond mode 5. This is because, as shown in Figure 7.4, peak pressure decreases for higher mode standing waves. The pressures required to cause movement at higher modes cannot be reached with the speaker used.

Although the Styrofoam is much lighter than the alumina rods, the circular rods may roll along the surface of the microstrip board. Acoustically moving the alumina overlay rods was tested by inserting a microstrip board with alumina rods placed on top into the acrylic tube. Placing various alumina rods along the microstrip board allows the determination of where the rods move the most with respect to the acoustic nodes and antinodes. 1/8", ¼", and 3/8" diameter rods were placed along a microstrip board in 1" increments. Figure 7.5 is a picture of the test setup with 1/8" diameter rods.

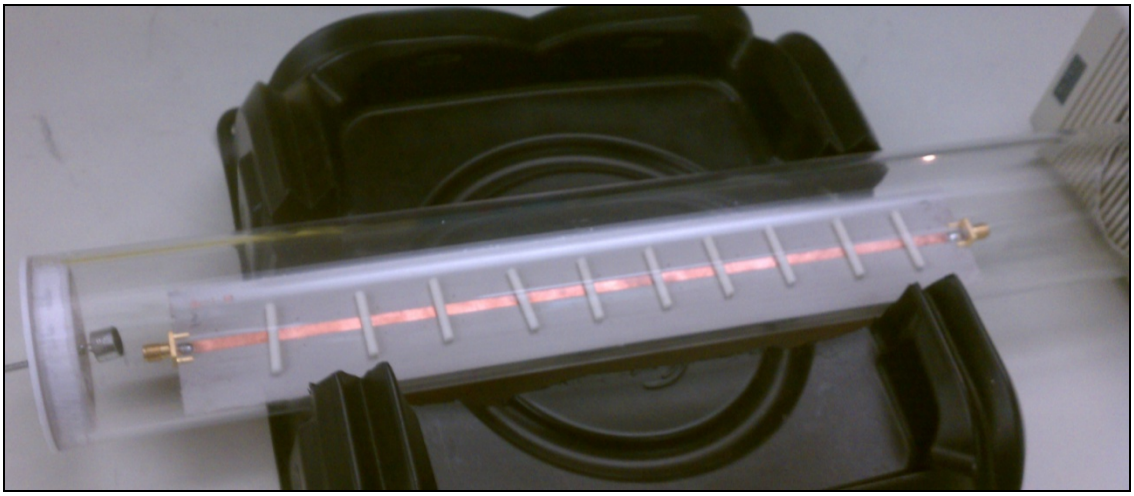

Figure 7.5: Test setup of 1/8" diameter rods on a microstrip board in standing wave tube.

Since the first order standing wave mode has the highest peak pressure, it is the first mode tested for moving overlay. For a first order standing wave in an open-closed tube, the anti-node is at the closed end and the node is at the open end. This means if moveable, the rods should move towards the speaker (node). The Styrofoam pieces were moveable at 40% max speaker volume for the first mode; it is expected that the volume must be greater to achieve this result for the overlay rods. First the 1/8” diameter rods were tested. With the speaker at 100% volume, only a few rods displayed movement. The rods which moved were not the rods closest to either end; the movement was likely due to vibrations of the tube and microstrip board. Also, the movement was not linear rolling as intended, but rather rotation and shifting in the direction perpendicular to the trace. The third standing wave mode did not produce any effect on the rods, presumably because of the decrease in peak pressure. Identical behavior was observed for ¼” and 3/8” diameter rods. Any movement only occurred only at the first order mode and didn’t produce the desired rolling movement.

To maintain control of each overlay rod, a node must exist in the standing wave for each overlay rod. A configuration with ten periods requires a 21st order standing wave. Creating a 21st order standing wave with enough peak pressure to control overlay rods using the 4.5W speaker is far beyond reason; even a first order standing wave didn't have enough peak pressure to move the overlay rods. Peak standing wave pressure may be increased by using a higher power speaker, but considering the results gained using a 4.5W speaker, the caliber of speaker required to control many overlay elements would render the system impractical.

Since the tuning mechanism didn't operate as intended with the minimum tube length (15"), testing the system with the adjustable extension tube was not necessary. Making connections from the microstrip board (inside of the tube) to test equipment (outside of the tube) was also not necessary. This would be accomplished by drilling holes in the acrylic tube where SMA connectors would be mounted to interface the microstrip board to test equipment. This would introduce the challenge of making the connectors hermetically sealed so pressure from the tube does not escape.

7.2 Mechanical Tuning Mechanism Testing

The mechanical arm tuning mechanism is a much simpler tuning approach than the acoustic tuning mechanism. Here, the concern is not whether the overlay rods may be moved, but how accurate the periodicity of the structure is. To evaluate the performance of the mechanical tuning mechanism, its periodicity will be evaluated by comparing the S_{21} responses which it produces with those produced in controlled overlay testing.

Ten ¼" square rods are attached to the ten middle pivot points of the mechanical arm; therefore its responses will be compared to controlled overlay tests using ten ¼"

square rods. The device is constructed so that other sized overlay rods may be swapped in or out. The nominal period spacing of the mechanical arm will be defined as the measured period spacing of the first periodic cell. If the periodicity of the mechanical arm is sound, then each periodic cell will be equal in length and the S_{21} responses should match those obtained in simulation and controlled overlay testing. If the periodicity is not sound, then the response will have distorted band-gaps. Figure 7.6 below is a picture of the mechanical arm mechanism with a period spacing of 1000 mils.

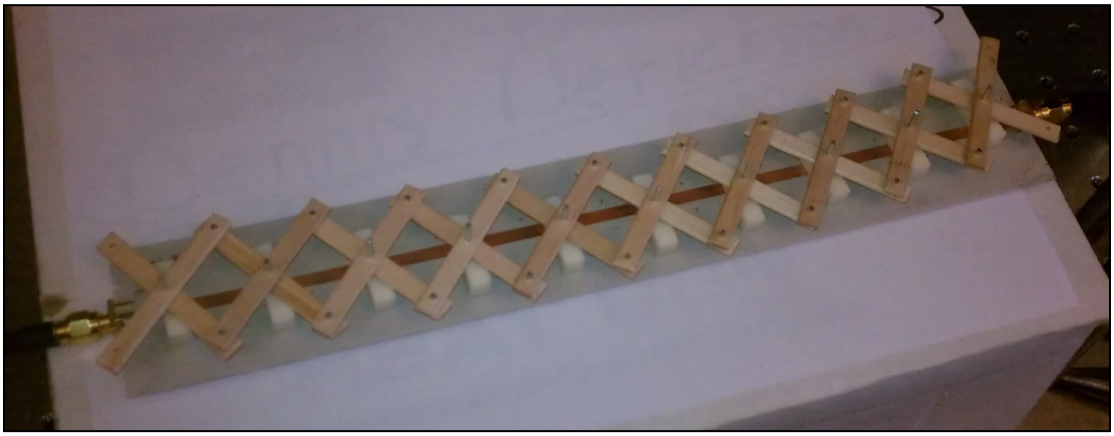

Figure 7.6: Mechanical arm tuning mechanism with ten 1/4" square alumina rods and period spacing of 1000 mils.

Test results using the mechanical arm tuning mechanism are tabulated on the following pages for comparison with controlled overlay testing and simulation:

Table 7.3: Mechanical arm tuning mechanism performance comparison of band-gap center frequency.

Substrate				Band-gap Center Frequency (GHz)			Error (GHz)	
	Overlay	Period	# of Periods	Simulation	Controlled Overlay	Mechanical Arm	Controlled Overlay	Mechanical Arm
Duroid® 5880LZ	¼" Square	500	10	7.48	7.407	7.556	-0.073	0.076
		1000	10	4.10	4.104	4.302	0.004	0.202
		1500	6	2.83	2.887	2.837	0.057	0.007
Duroid® 3006	¼" Square	500	10	4.95	5.396	4.924	0.446	-0.026
		1000	10	2.64	2.812	2.837	0.172	0.197
		1500	6	1.81	1.993	1.893	0.183	0.083

Table 7.4: Mechanical arm tuning mechanism performance comparison of band-gap rejection.

Substrate				Band-gap Rejection (dB)			Error (dB)	
	Overlay	Period	# of Periods	Simulation	Controlled Overlay	Mechanical Arm	Controlled Overlay	Mechanical Arm
Duroid® 5880LZ	¼" Square	500	10	-22.958	-34.17	-15.20	-11.21	7.761
		1000	10	-14.891	-14.45	-7.329	0.441	7.562
		1500	6	-5.973	-4.211	-2.812	1.762	3.161
Duroid® 3006	¼" Square	500	10	-15.545	-10.46	-5.541	5.085	10.00
		1000	10	-11.733	-6.101	-2.720	5.632	9.013
		1500	6	-3.073	-1.209	-1.511	1.864	1.562

Table 7.5: Mechanical arm tuning mechanism performance comparison of band-gap bandwidth.

Substrate				Band-gap Bandwidth (GHz)			Error (GHz)	
	Overlay	Period	# of Periods	Simulation	Controlled Overlay	Mechanical Arm	Controlled Overlay	Mechanical Arm
Duroid® 5880LZ	¼" Square	500	10	1.92	1.54	1.938	-0.38	0.018
		1000	10	0.95	0.91	0.560	-0.04	-0.39
		1500	6	--	--	--	--	--
Duroid® 3006	¼" Square	500	10	0.96	0.8	0.561	-0.16	-0.399
		1000	10	--	--	--	--	--
		1500	6	--	--	--	--	--

Results suggest that the mechanical arm tuning mechanism yields fundamental band-gap responses comparable to controlled overlay testing. For some tested configurations, the tuning mechanism's results are more accurate to the simulation. For each tested case the mechanical arm yielded smaller band-gap rejection than controlled overlay testing did. This is partly caused by a slight bend in the arm which arises when it is extended. This bend causes some overlay rods to become slightly lifted above the microstrip trace; this introduces an air-gap between the overlay and trace.

As proven in simulation, discontinuities in the periodicity of an EBG structure degrade a band-gap's rejection. This is another source of the consistently poorer band-gap rejection. In this device, discontinuities are a result of small offsets in drilled hole locations between each of the mechanical arm supports. If each of the 20 supports were identical, the mechanical arm could have perfect periodicity but any mechanical structure build by hand will not be perfect. Also, the initial adhering of the overlay elements onto the middle joints of the mechanical arm cannot be assumed to be perfect; this is another source of small.

The maximum and minimum achievable period spacing values on the mechanical arm are 1500 mils and 250 mils respectively. The upper limit is due to the length of the criss-crossing supports, and the lower limit is due to the ¼" width of the rods. When extended to the maximum spacing, only six overlay rods can fit on the 11" microstrip board. The resulting tunable frequency ranges for band-gap center frequency are 2.837-9.519 GHz for Duroid® 5880LZ and 1.893-7.209 GHz for Duroid® 3006. These are large tunable frequency ranges as the initial goals specified.

Chapter 8

CONCLUSION

In this thesis a new solution for a tunable electromagnetic band-gap structure was successfully designed, simulated, fabricated, and tested. This tunable EBG structure uses moveable dielectric overlay elements on top of a microstrip board to adjust the periodicity of the structure. In chapter 2, the band-gap center frequency of an EBG structure was derived, and it was proven that band-gap rejection increases with the number of periods. In chapter 3 the design was reached by evaluating various multilayer substrate microstrip configurations. Simulations in chapter 4 using Agilent's ADS provided much insight into how each EBG parameter (periodicity, number of periods, overlay dielectric constant, etc…) affects band-gap properties. Also, a new method for controlling the rejection of higher order band-gaps was discovered through varying the fill factor of periodic cells. This introduced new filtering possibilities such odd harmonic filtering and third order multiple harmonic filtering. While controlled overlay testing results didn't perfectly match simulation, it verified all of the relationships previously established. Passband loss was much greater than expected, making this solution not ideal for high frequency filtering applications. However, the robustness in tunable frequency range and fine tuning precision which other current solutions lack was met.

To make this system usable in filtering applications, two tuning mechanisms which adjust the overlay position were developed. The acoustic standing wave tuning mechanism aimed to control the position of circular overlay rods by using the periodicity of an acoustic standing wave. The pressure required to move these rods was found to be

much too great for practical implementation. Although the desired results were not met, valuable information was gained regarding the feasibility of using such a device as an overlay tuning mechanism. A simpler tuning device, a mechanical arm pantograph, gave better results. While the mechanical arm made adjusting the period quick and easy, it lacked accuracy in periodicity which caused band-gap distortion. Although initial implementations of these devices didn't produce desired results, they provided useful findings which may be used in future work.

8.1 Future Work

Tuning mechanism: A great challenge in using this system as a tunable EBG filter is the precision in overlay placement required to minimize distortion of higher order band-gaps. Even in controlled overlay testing distortion was present for high order band-gaps. To improve upon the work already completed a more accurate tuning device may be developed. The developed EBG microstrip structure has been proven to work as a model for a tunable EBG structure, but a more accurate tuning mechanism must be developed for it to be considered a practical filter solution. The mechanical arm was made by hand. A new mechanical arm could be fabricated from a machine; then its periodicity would be much more accurate. Other adjustable periodic structures could be investigated.

Materials and substrates: A big downside found in using the microstrip/overlay topology is the large loss at high frequencies. Since only two substrates and one overlay material were used, further investigation into loss prevention couldn't be made. Testing more substrate and overlay material combinations could provide more insight into how loss can be minimized while maintaining adequate band-gap rejection.

WORKS CITED

[1] J. H. Apfel, "Phase retardance of periodic multilayer mirrors," *Applied Optics, Vol. 21, Issue 4,* pp. 733-738, 1982.

[2] C. Klein and C. S. Hurlbut, Manual of Mineralogy, 20th ed., 1985.

[3] V. Radisic, Y. Qian, R. Coccioli and T. Itoh, "Novel 2-D photonic bandgap," *IEEE Microwave and Guided Wave Letters,* vol. 8, pp. 69-71, 1998.

[4] D. Thalakotuna, L. Matekovits, K. Esselle and M. Heimlich, "Dynamic tuning of electromagnetic bandgap," *Antennas and Propagation (EUCAP), Proceedings of the 5th European Conference on,* pp. pp.1065-1067, 11-15 April 2011.

[5] D.-I. Yeom, P. Steinvurzel, B. J. Eggleton, S. D. Lim and B. Y. Kim, "Tunable acoustic gratings in solid-core photonic bandgap fiber," *Optics Express,* vol. 15, no. 6, pp. 3513-3518, 2007.

[6] P. S. J. Russell, "Photonic Crystal Fibers," *Journal of Lightwave Technology,* vol. 24, no. 12, pp. 4729-4749, 2006.

[7] M. Shimizu, "Optical Access Network Technology (Optical Media Technology) Toward Expansion of FTTH," *NTT Technical Review,* vol. 6, no. 5, pp. 1-8, 2008.

[8] D. M. Pozar, Microwave and RF Design of Wireless Systems, Wiley, 2001.

[9] J. Zhao, X. Li, L. Zhong and G. Chen, "Calculation of photonic band-gap of one dimensional photonic crystal," *Journal of Physics: Conference Series,* vol. 183, no. 1, 2009.

[10] J. Svacina, "Analysis of mulitlayer microstrip lines by a conformal mapping method," *IEEE Transactions on Microwave Theory and Techniques,* vol. 40, no. 4, pp. 769-772, April 1992.

[11] Rogers Corporation, "RT/duroid® 5880LZ High Frequency Laminates," 2012. [Online]. Available: http://www.rogerscorp.com/documents/1100/acm/RT-duroid-5880LZ-High-Frequency-Laminates.pdf. [Accessed 18 September 2012].

[12] Rogers Corporation, "RO3000® Series Circuit Materials," 2011. [Online]. Available: http://www.rogerscorp.com/documents/722/acm/RO3000-Laminate-Data-Sheet-RO3003-RO3006-RO3010.pdf. [Accessed 18 September 2012].

[13] Y. Liu and P. H. Daum, "Relationship of refractive index to mass density and self-consistency of mixing rules for multicomponent mixtures like ambient aerosols," *Journal of Aerosol Science,* vol. 39, no. 11, pp. 974-986, 2008.

[14] Insaco, "Alumina 99.5% (Al2O3) Data, Properties, Grades and Tolerances - Supplier Data By Insaco," 2 Mar 2006. [Online]. Available: http://www.azom.com/article.aspx?ArticleID=3269. [Accessed 29 Sept 2012].

[15] A. Kundt, "Acoustic Experiments," *The London, Edinburgh and Dublin Philosophical Magazine and Journal of Science,* vol. 35, no. 4, pp. 41-48, 1868.

[16] UM Physics Demonstrations, "3D30.60 - Kundt's Tube," University of Michigan, 2007. [Online]. Available: http://webapps.lsa.umich.edu/physics/demolab/content/demo.aspx?id=848. [Accessed 10 April 2012].

[17] Dell, "Specifications: Altec Lansing Computer Speaker System ACS90," [Online]. Available: http://support.dell.com/support/edocs/acc/61408/Specs.htm. [Accessed 13 December 2012].

[18] E. Sengpiel, "Table of Sound Pressure Levels," [Online]. Available: http://www.siue.edu/~gengel/ece476WebStuff/SPL.pdf. [Accessed 26 March 2012].

[19] S. Ohms, "Guide to Speaker Specifications," PSB Speakers, 2 June 2006. [Online]. Available: http://www.psbspeakers.com/articles/Guide-to-Speaker-Specifications. [Accessed 26 March 2012].

[20] D. Harrison, "Standing Waves & Acoustic Resonance," October 1999. [Online]. Available: http://faraday.physics.utoronto.ca/IYearLab/stwaves.pdf. [Accessed 7 November 2012].

[21] RadioShack, "Electret Microphone Element," 5 April 1996. [Online]. Available: http://support.radioshack.com/support_supplies/doc9/9796.htm. [Accessed 25 November 2012].

Appendix A
Acoustic Standing Wave Tube Pressure Measurements

The following graphs represent the data measured as described in sections *7.1.1* and *7.1.2*. The 'measured' trace represents data measured using the microphone and the 'projected' trace represents the complete expected waveform based on the peak pressures measured at the anti-nodes and the frequency of the sound wave. For mode 1 only four data points were recorded because the max pressure limit of the microphone was reached.

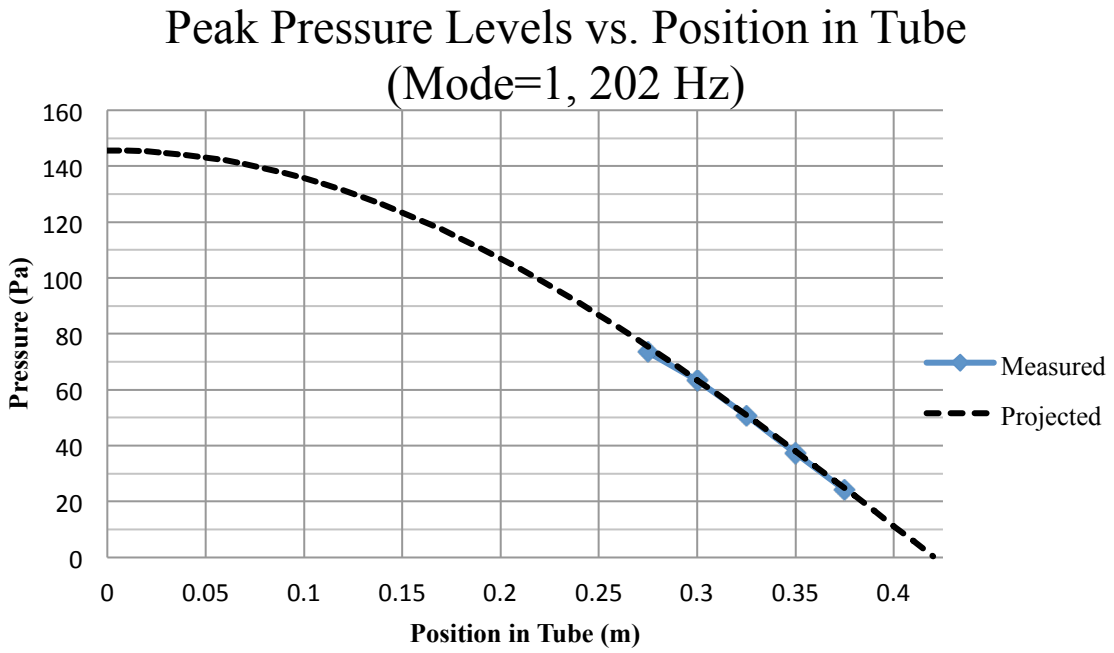

Figure A.1: Peak Pressure Levels in Standing Wave Tube of mode 1.

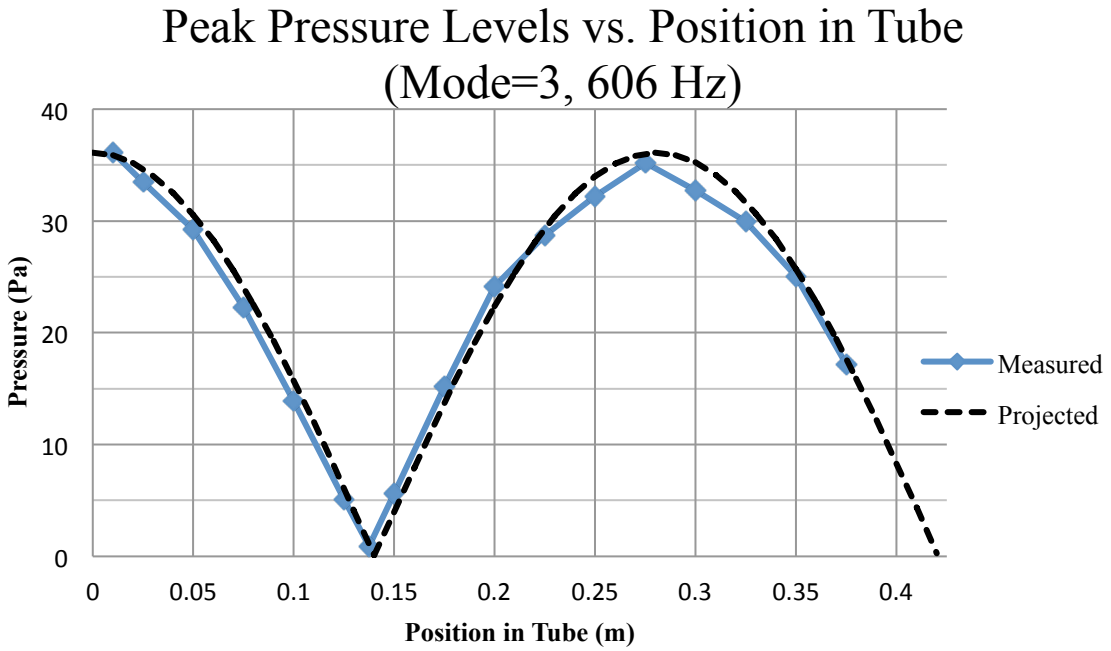

Figure A.2: Peak pressure levels in standing wave tube of mode 3.

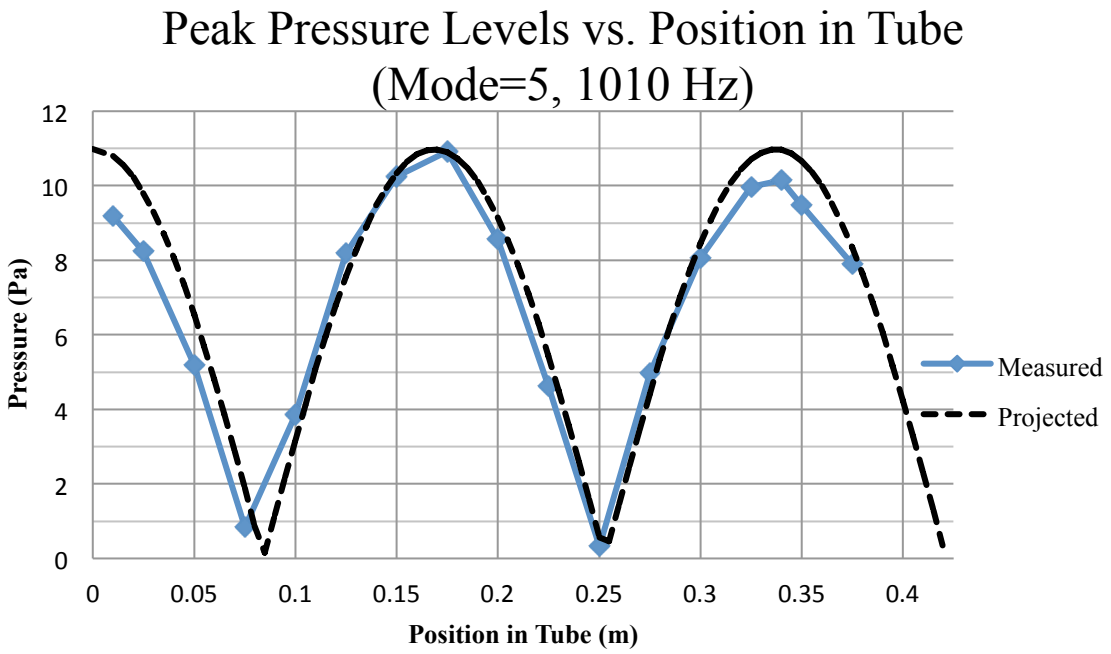

Figure A.3: Peak pressure levels in standing wave tube of mode 5.

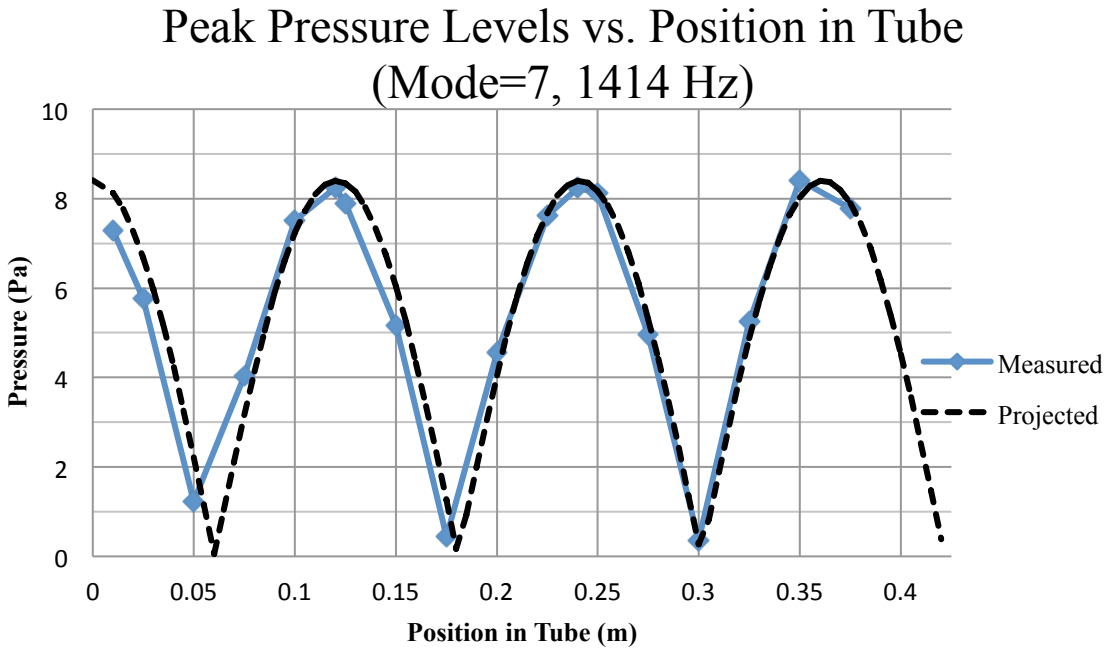

Figure A.4: Peak pressure levels in standing wave tube of mode 7.

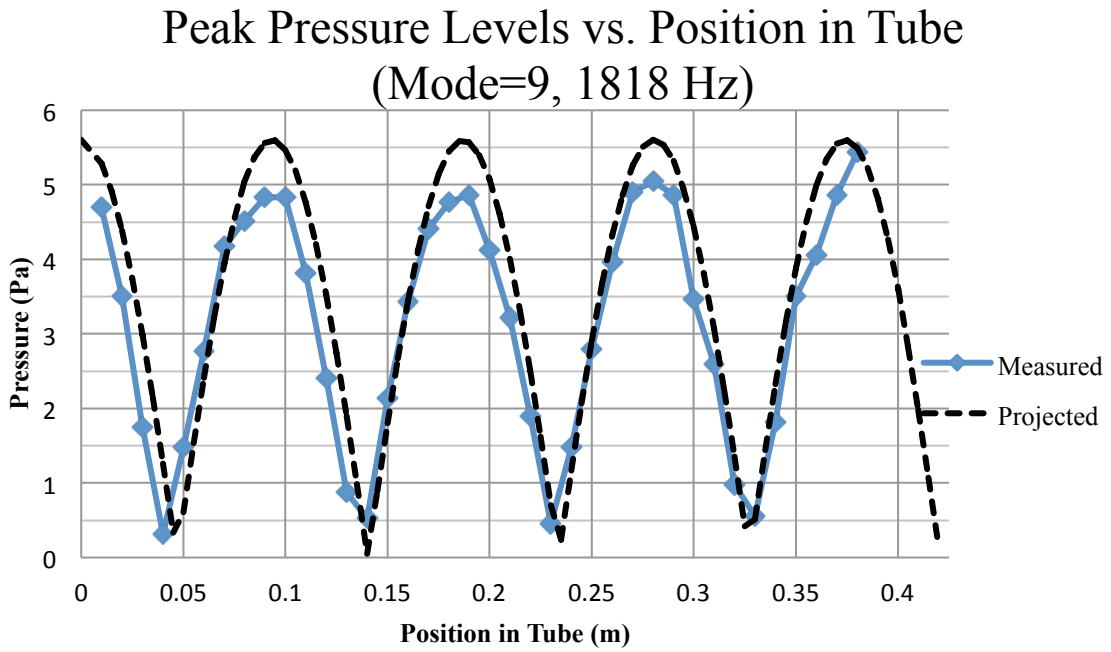

Figure A.5: Peak pressure levels in standing wave tube of mode 9.

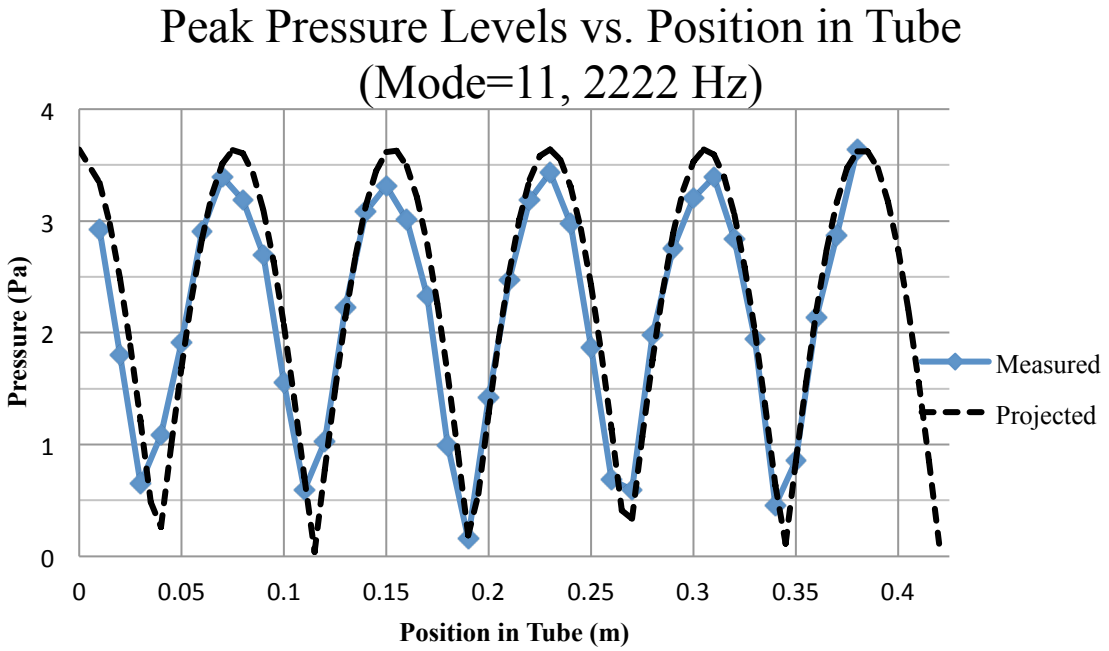

Figure A.6: Peak pressure levels for a standing wave tube of mode 11.

Appendix B
Band-gap Rejection Comparison Graphs

The following graphs show the band-gap rejection vs. number of periods for the three period spacing values, each size overlay element, and each dielectric substrate.

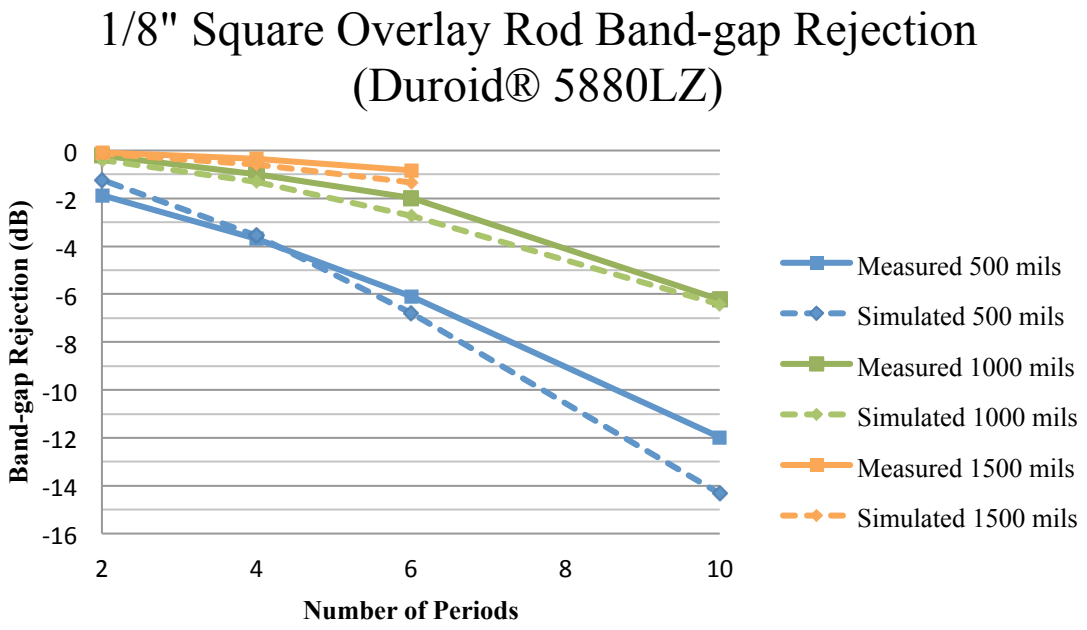

Figure B.1: Comparison of measured and simulated S_{21} band-gap rejection for 1/8" square overlay on Duroid® 5880LZ.

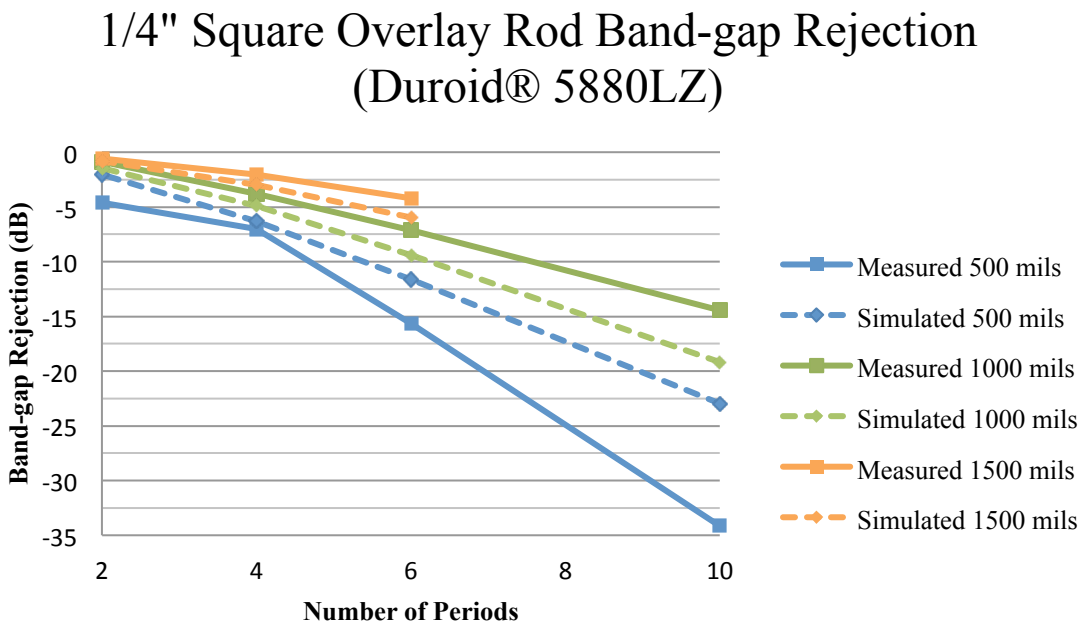

Figure B.2: Comparison of measured and simulated S_{21} band-gap rejection for 1/4" square overlay on Duroid® 5880LZ.

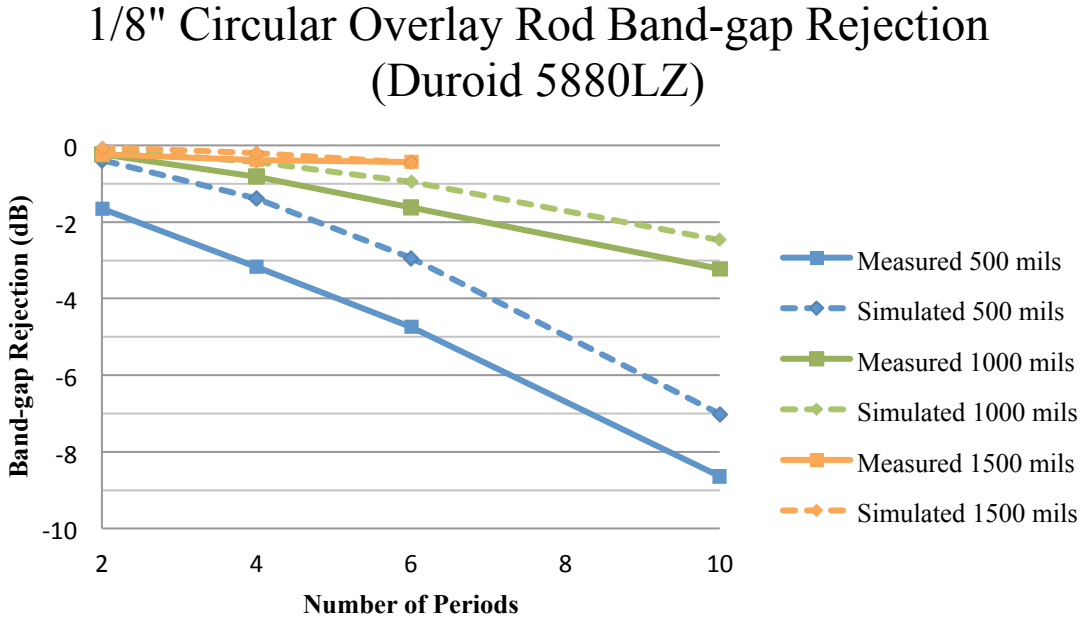

Figure B.3: Comparison of measured and simulated S_{21} band-gap rejection for 1/8" circular overlay on Duroid® 5880LZ.

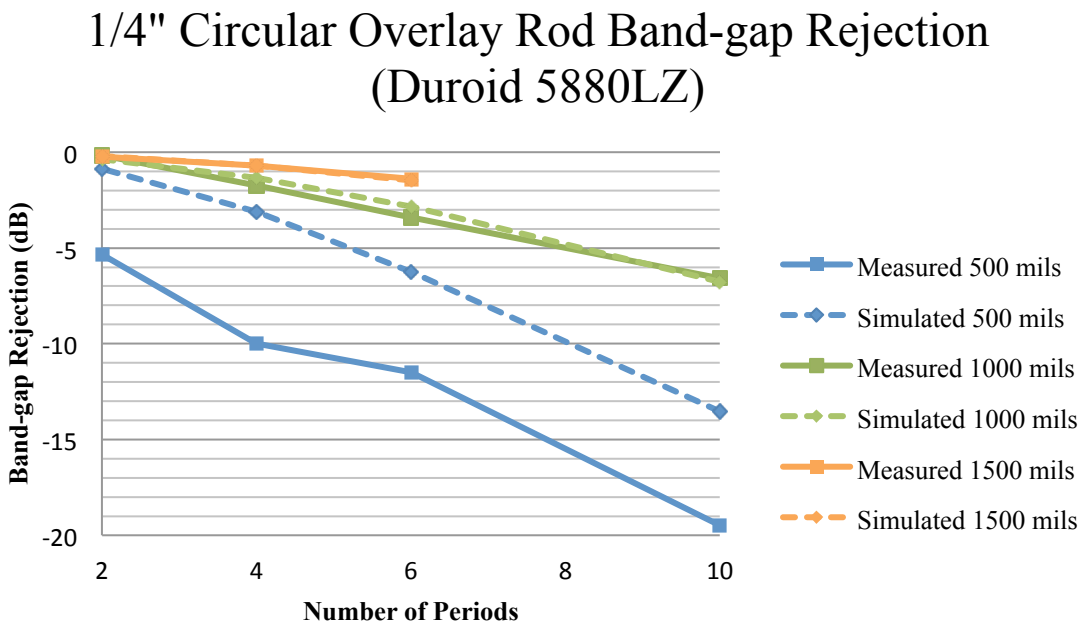

Figure B.4: Comparison of measured and simulated S_{21} band-gap rejection for 1/4" circular overlay on Duroid® 5880LZ.

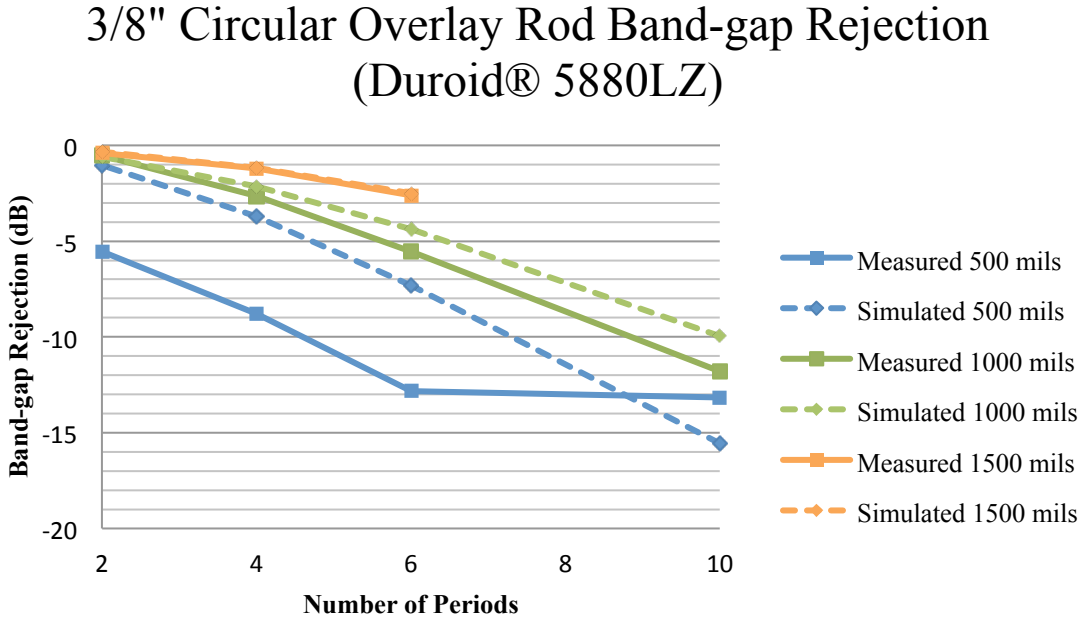

Figure B.5: Comparison of measured and simulated S_{21} band-gap rejection for 3/8" circular overlay on Duroid® 5880LZ.

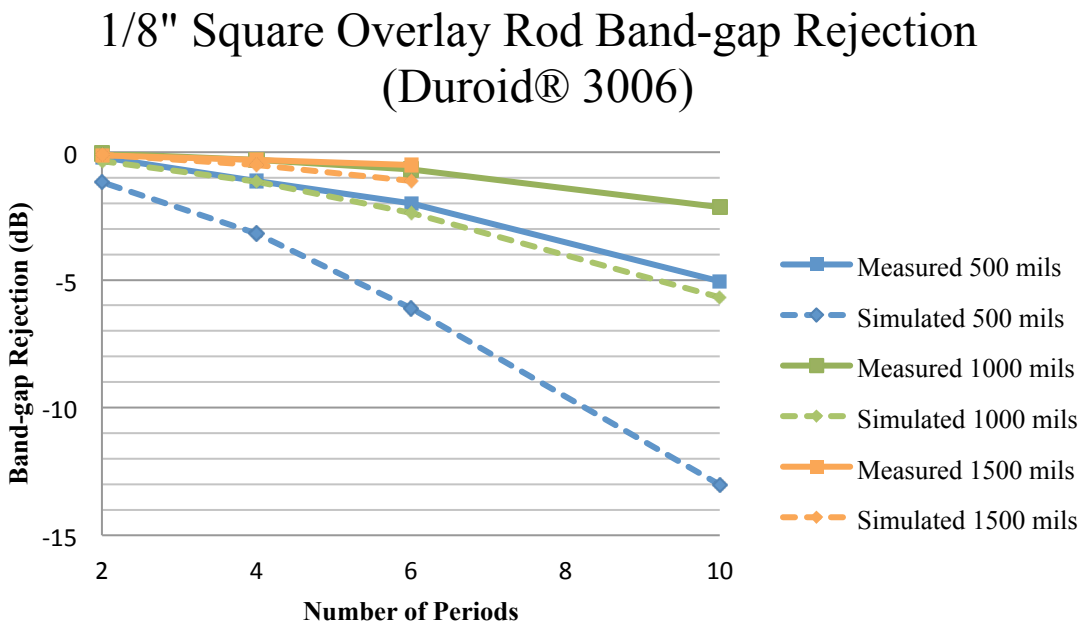

Figure B.6: Comparison of measured and simulated S_{21} band-gap rejection for 1/8" square overlay on Duroid® 3006.

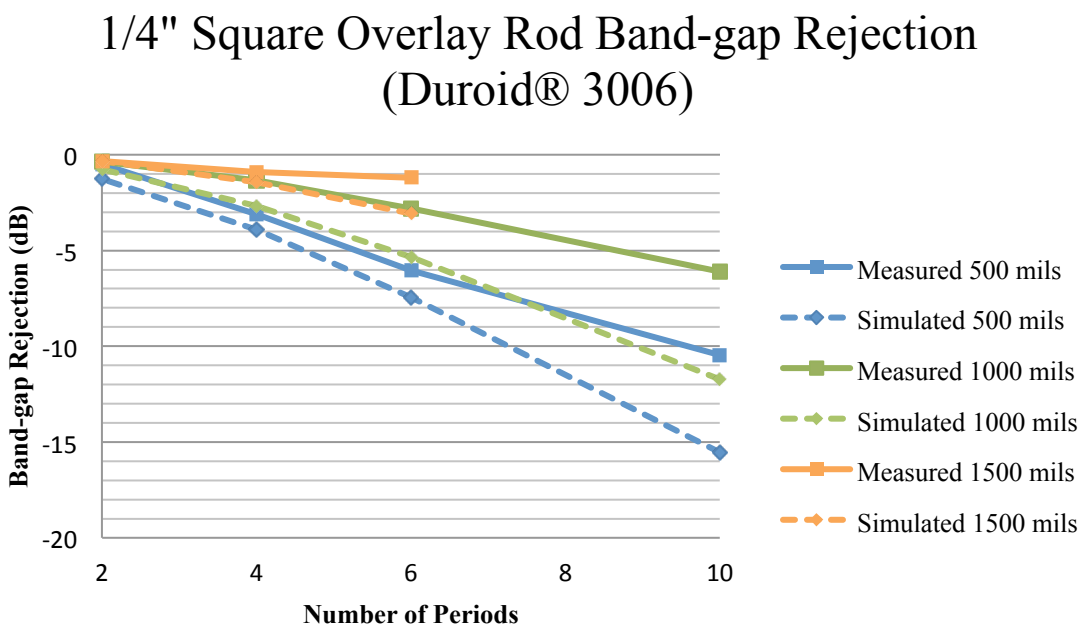

Figure B.7: Comparison of measured and simulated S_{21} band-gap rejection for 1/4" square overlay on Duroid® 3006.

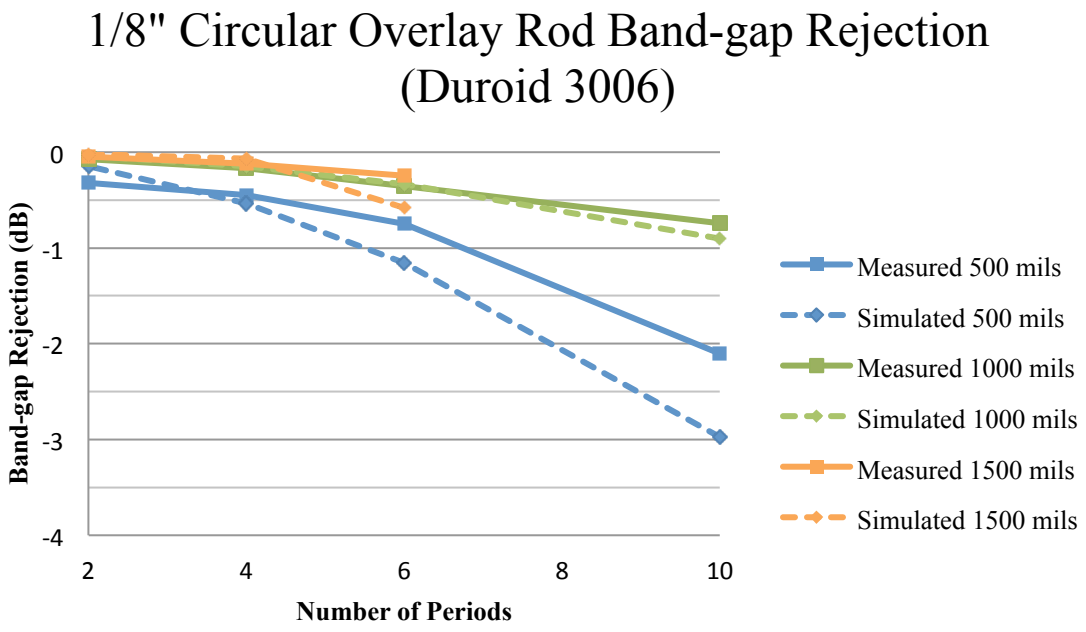

Figure B.8: Comparison of measured and simulated S_{21} band-gap rejection for 1/8" circular overlay on Duroid® 3006.

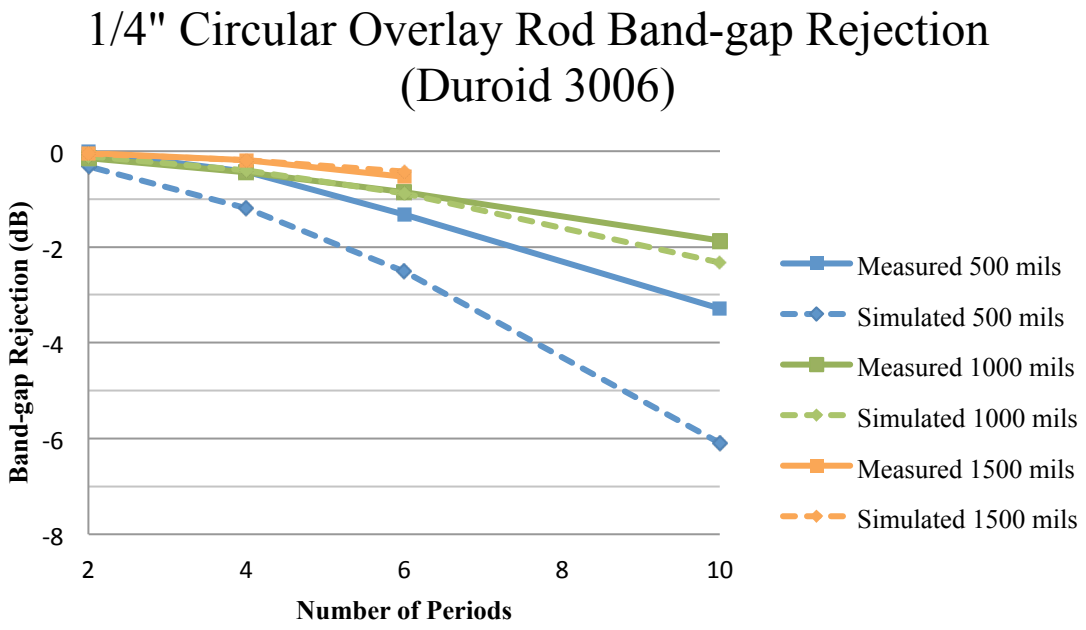

Figure B.9: Comparison of measured and simulated S_{21} band-gap rejection for 1/4" circular overlay on Duroid® 3006.

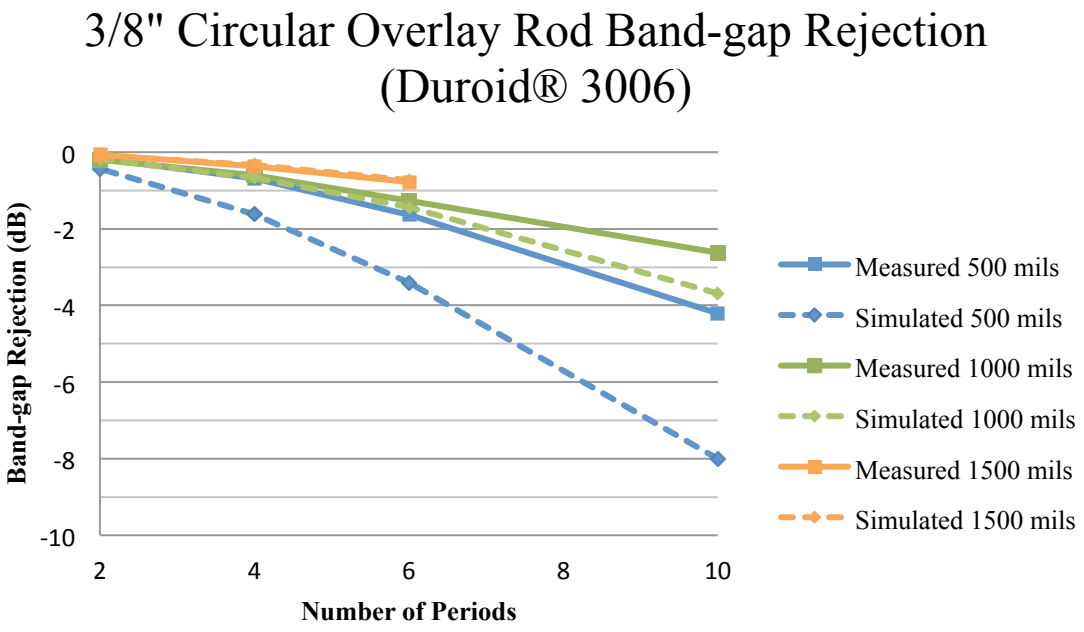

Figure B.10: Comparison of measured and simulated S_{21} band-gap rejection for 3/8" circular overlay on Duroid® 3006.

Appendix C
ANALYSIS OF SENIOR PROJECT DESIGN

C.1 Summary of Functional Requirements

The tunable EBG microstrip filter must improve upon previous solutions by accommodating both a wide tunable frequency range and fine tunable precision. More specifically, the tunable range requirement is 1-6 GHz. A fine tunable range requires a non-discrete tuning implementation. In an ideal band-stop (band-gap filter), passband ripple is minimized while stopband rejection is maximized. Filter requirements are <1dB passband ripple and >10dB band-gap rejection. To interface with standard test equipment ports use standard SMA connectors with 50Ω input impedance.

C.2 Primary Constraints

The design is limited by the inherent nature of EBG structures. Tuning an EBG structure requires physically altering its periodicity. This provides a great challenge. This thesis seeks a novel solution to this problem. Fabrication limitations include acquiring substrates, connectors, and a milling machine. Testing is limited by the need for a high frequency network analyzer (up to 20 GHz). As an initial proof of concept, the project has no size or cost limitations.

C.3 Economic

The EBG filter itself only consists of the microstrip board, connectors, and overlay rods. The microstrip boards were acquired as free samples through Rogers Corporation. These substrates are common microwave materials used in many applications. The overlay rods were acquired through Ortech Ceramics and, as a specialty

material, were the most expensive accessory in the project. Tuning mechanism cost was low as they required only a few parts. The bill of materials is included below.

Table C.1: Bill of Materials

Item	Cost/Unit	Quantity	Cost
Duroid® 5880LZ/ Duroid® 3006	Free Sample	1	--
SMA Panel Mount Connector	$3.49	4	$13.96
3/8" x 12" Long Alumina 99.8% Circular Rod	$42.54	1	$42.54
1/4" x 12" Long Alumina 99.8% Circular Rod	$36.06	1	$36.06
1/8" x 12" Long Alumina 99.8% Circular Rod	$26.31	1	$26.31
1/4" x 12" Long Alumina 99.8% Square Rod	$49.29	1	$49.29
1/8" x 12" Long Alumina 99.8% Square Rod	$31.62	1	$31.62
2 ¼" x 6' Clear Acrylic Tube (1/8" wall)	$26.75	1	$26.75
2'x2" Mailing Tube	$2.99	1	$2.99
End Cap, 2"	$0.25	2	$0.50
Wood Sticks, 75pc. 5 ¾"x1/4"x3/32"	$1.99	1	$1.99
#17x1" Wire Nails	$1.30	1	$1.30
Total	--	--	**$233.31**

This device is relatively low cost considering the generally high cost of most high frequency components. If investigated further, lower cost overlay dielectric materials could be used and would further reduce the cost.

C.4 Commercial Manufacturing

The device is not yet in production form. To make it more feasible for real applications, further investigation and design improvements must be made. The device would not likely be used in commercial applications, but rather by private companies for high frequency communications.

C.5 Environmental

Neither this project nor the device poses harm or impact on the environment.

C.6 Manufacturability

There are no special challenges relating to the manufacturability of the device. Microstrip fabrication is a very common procedure in microwave design. To make the acoustic tuning mechanism usable, connections to the microstrip board inside the tube must be made to the outside of the tube. This requires making holes in the tube where connectors could interface the inside of the tube with the outside. A more accurate mechanical arm tuning mechanism requires an automated manufacturing process. This may be accomplished using a milling machine or a machine which can drill holes with high precision.

C.7 Sustainability

The EBG filter itself is a passive device; no external power is needed for the filter to operate. The tuning mechanisms, however, require an external force to move the overlay elements. The speaker tested is rated for 4W, but the pressure levels it created at maximum output volume was still not great enough to move the overlay rods. The acoustic pressure level, and speaker power required to produce the intended tuning results would render the device to be an unsustainable design. The mechanical arm tuning mechanism requires very little force to adjust the periodicity of the structure; it is a much more efficient design.

The configurations tested had very high loss at higher order band-gaps, making it inefficient harmonic filtering. To reduce the passband loss and make the filter more efficient, more substrates and more precise tuning methods must be investigated.

C.8 Ethical

There is no ethical relevance to designing a tunable EBG filter.

C.9 Health and Safety

The project and device have no potential health or safety concerns.

C.10 Social and Political

There is no social or political relevance to designing a tunable EBG filter.

C.11 Development

New tools and techniques learned during the project:

1. Modeling circular overlay elements using ADS
2. Microstrip fabrication using a milling machine
3. Pressure level measurements using an electret condenser microphone